# IDŐJÁRÁS

QUARTERLY JOURNAL
OF THE HUNGARIAN METEOROLOGICAL SERVICE

## CONTENTS



VOL. 119 * NO. 3 * JULY – SEPTEMBER 2015

# IDŐJÁRÁS

*Quarterly Journal of the Hungarian Meteorological Service*



*Editorial Office: Kitaibel P.u. 1, H-1024 Budapest, Hungary*
*P.O. Box 38, H-1525 Budapest, Hungary*
*E-mail: journal.idojaras@met.hu*
*Fax: (36-1) 346-4669*

**Indexed and abstracted in Science Citation Index Expanded™ and Journal Citation Reports/Science Edition**
**Covered in the abstract and citation database SCOPUS®**

*Subscription by mail:*
*IDŐJÁRÁS, P.O. Box 38, H-1525 Budapest, Hungary*
*E-mail: journal.idojaras@met.hu*

# IDŐJÁRÁS

*Quarterly Journal of the Hungarian Meteorological Service*
*Vol. 119, No. 3, July – September, 2015, pp. 307–335*


# Measuring and modeling of hazardous weather phenomena to aviation using the Hungarian Unmanned Meteorological Aircraft System (HUMAS)


**Zsolt Bottyán**[1*], **András Zénó Gyöngyösi**[2], **Ferenc Wantuch**[3], **Zoltán Tuba**[1], **Rita Kurunczi**[4], **Péter Kardos**[5], **Zoltán Istenes**[6], **Tamás Weidinger**[2], **Katalin Hadobács**[7], **Zoltán Szabó**[2], **Márton Balczó**[8], **Árpád Varga**[8], **Andrea Bíróné Kircsi**[9], and **Gyula Horváth**[10]

[1]*Department of Military Aviation, National University of Public Service, P. O. Box. 1,H-5008 Szolnok, Hungary*

[2]*Department of Meteorology, Eötvös Loránd University, Pázmány Péter sétány 1/A., H-1117 Budapest, Hungary*

[3]*Aviation Authority, National Transport Authority, Lincoln u. 1., H-2220 Vecsés, Hungary*

[4]*Időkep Ltd., Bartók B. út 65/b., H-1224 Budapest, Hungary*

[5]*HungaroControl, Hungarian Air Navigation Plc, Iglo u. 33–35, H-1185 Budapest, Hungary*

[6]*Department of Software Technology and Methodology, Eötvös Loránd University, Pázmány Péter sétány 1/C., H-1117 Budapest, Hungary*

[7]*Geoinformation Service, Hungarian Defence Forces, H-1524 Budapest, Hungary*

[8]*Department of Fluid Mechanics, Budapest University of Technology and Economics, Budafoki út 8, H-1111 Budapest, Hungary*

[9]*Department of Meteorology, University of Debrecen, H-4032 Debrecen, Egyetem tér 1., Hungary*

[10]*Hungarian Meteorological Service, Gilice tér 39, 1181 Budapest, Hungary*

**Corresponding author E-mail: bottyan.zsolt@uni-nke.hu*



*(Manuscript received in final form November18, 2014)*



**Abstract**—At present, Unmanned Aircraft Systems (UAS) are playing more and more significant role in military and civil operations in Hungary. A well-used meteorological support system is essential during the planning and executing phases of different UAS

missions. In the present work, the structure of an applied analog statistical and a WRF-based numerical forecast system is to be introduced with special regards to aviation meteorological factors, such as visibility, ceiling, turbulence, icing, etc. Within such a system, it is very important to generate an accurate short-time visibility prediction. In order to develop such forecasts, we combined an analogy based statistical approach to a high-resolution numerical model for visibility prediction, which are currently available as a hybrid visibility prediction for the regions of four main airports in Hungary. On the other hand, we also present the first Hungarian Unmanned Meteorological Aircraft System (HUMAS). In our case study, the HUMAS measurements are compared to dynamical weather prediction data during the international planetary boundary layer (PBL) campaign in Szeged, Hungary.

*Key-words*: aviation meteorology, Unmanned Aircraft Systems, integrated forecast system, fuzzy logic, WRF model, visibility, cloud ceiling

## *1. Introduction*

Application of Unmanned Aircraft Systems (UAS) for both civilian and military purposes spreads very rapidly worldwide because of its low operational costs that are expected to even more decrease significantly in the near future (*Gertler*, 2012; *Watts*, 2012). Unmanned systems are playing more and more significant role in military and civil operations also in Hungary (*Fekete* and *Palik*, 2012; *Somlyai et al.*, 2012; *Restás*, 2013). Aerial support for natural or industrial disaster management, monitoring (earthquakes, floods and forest fire etc.), government and private survey (cartography, agriculture, wild life monitoring, border control, security and maintenance control for industrial companies, electricity cords or oil and gas pipeline networks, etc.) and the defense of critical infrastructures may benefit from the onboard instruments that might be the payload of such UASs (*Adams* and *Friedland*, 2011; *Gyöngyösi et al.*, 2013; *Restás* and *Dudás*, 2013). Unmanned aviation, on the other hand, is even more sensitive to the actual weather situation than manned flights. Due to their smaller dimensions compared to manned vehicles, the areodynamic processes during flight that highly depend on the present state of the atmosphere are affecting the reliability of flight in a manner more sensitive than for larger sized aircrafts. In addition, the weather itself is able to modify not only the (aero)dynamic aspects of aviation processes but the navigation and execution of a given mission (reconnaissance, observation, etc.), too. The mentioned atmospheric influence on the aviation is more important in the case of unmanned flights which are controlled by autonomous onboard robotic systems or remote pilots (*Williams*, 2004; *Drury et al.*, 2006). These airplanes usually have relatively large wings with a slim airfoil and significant surface area, thus, they are especially sensitive to gusts, turbulence, and airframe icing as well. Beyond that – similarly to manned ones –, they are also sensitive to heavy precipitation, low cloud, and poor visibility condition during their flights (*Østbø et al.*, 2004; *Hadobács et al.*, 2013).

In spite of the relative ease of controlling of most UAS, weather hazards may be extremely dangerous to their flights. Numerous UAS crashes and accidents were reported that were principally caused by hazardous weather factors. Despite of the mentioned sensitivity of UASs to weather – at present –, the number of systems that are specially developed for the meteorological support of UAS operators is relatively low (*Garcia et al.*, 2013; *Sun et al.*, 2014).

In order to decrease the weather-related risks during UAS flights, we had developed a complex meteorological support system for UAS users, mission specialists, and decision makers. This system is based on an integrated weather prediction software, the Integrated Forecasting System (IFS). Calibration and verification have been carried out using a special meteorological UAS, called the Hungarian Unmanned Meteorological Aircraft System (HUMAS). Finally, it is important to point out that this meteorological support system can easily be adopted for any location at all over the world, because the applied meteorological data and numerical model system are mainly open-access.

## *2. The Integrated Forecast System (IFS)*

Prediction of key aviation meteorological parameters such as visibility and ceiling is one of the greatest challenges for an operational forecaster. These variables are usually the Achilles' heel of numerical weather prediction (NWP) models, too (*Jacobs* and *Maat, 2005*; *Souders* and *Showalter,* 2008; *Hirardelli* and *Glahn*, 2010). Unfortunately, most of the phenomena which are affecting flight operations are not predicted directly even by high resolution NWP models. Visibility and ceiling are playing clearly a key role in the success of UAS missions, (*Bankert* and *Hadjimichael,* 2007). Usually, the operational minima of UAS flights are below the limits of special mission execution. For example, for reconnaissance or surveillance tasks, poor visibility and low ceiling can eliminate the mission but yield no restrictions to the UAS flight itself.

Accordingly, high resolution NWP model output data should be processed parallel to a statistical analysis of archive database for a given weather situation to produce the best combination forecast in a certain occasion. To solve the challenge of visibility and ceiling prediction, we developed the Integrated Forecast System (IFS) which consists of i) a suitable, specially tuned NWP model, ii) a statistical climatological prediction component, which all together are capable to generate iii) a reliable and appropriate hybrid (combined statistical and numerical) aviation meteorological forecasts for UAS operations.

The construction of the experimental complex meteorological IFS is based on the following parts:

- statistical modeling subsystem (SMS),
- numerical modeling subsystem (NMS),
- hybrid modeling subsystem (HMS),
- post processing subsystem (PPS),
- UAS measurements (UM).

The main components of the UAS meteorological support system and the relations of its different components are shown in *Fig. 1.* The Integrated Forecast System is a modeling and post-processing unit using both statistical and numerical outputs of its subsystems to produce hybrid visibility and ceiling forecasts. IFS uses climatological data of mentioned parameters from the statistical modeling subsystem and actual weather forecast data (basic meteorological variables) from the numerical modeling subsystem. Based on these parts, IFS is able to produce the hybrid (combined) short-time predictions with respect to both visibility and ceiling. On the other hand, IFS has a coupled UAS measurement (UM) component to verify and test the IFS predictions during the development time. The applied Hungarian Unmanned Meteorological Aircraft System (HUMAS) was equipped by meteorological sensors to measure the atmosphere with special regard to the state of the planetary boundary layer (PBL).

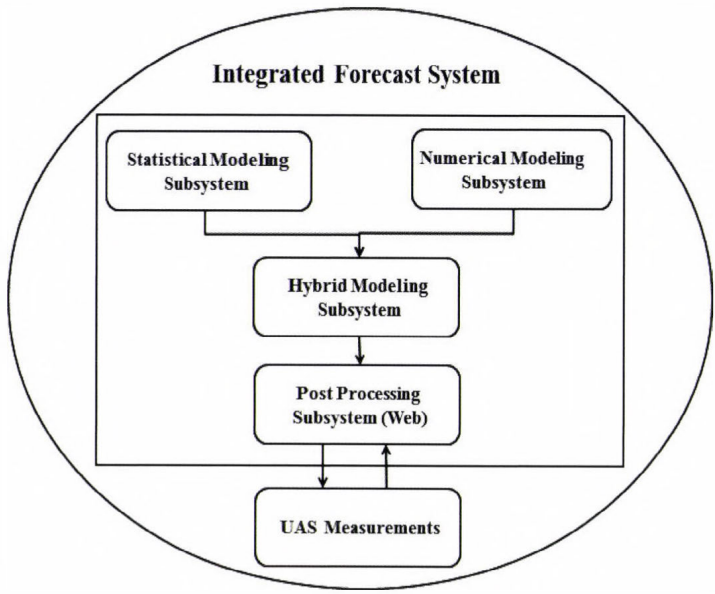


*Fig. 1.* The structure of the Integrated Forecast System (IFS) for UAS missions.

### *3. Statistical approach in the IFS*

Fuzzy logic based analog forecasting is a quiet new and effective tool of ultra-short term weather forecasting (*Hansen,* 2007).

The basic principle of analog forecasting is well known (from *Toth*, 1989) as to find similar weather situations in the past to the current and recent conditions and rank them according to the degree of their similarity in the interest of giving relevant information for weather forecasts. The term *weather situation* hereafter is meant as a couple-of-hour continuous observation. Therefore, analog forecasting does not work without a relevant climatic database which contains the meteorological parameters planned to forecast in the future. We had set up an appropriate database for Hungarian military airbases (LHKE, LHPA, and LHSN) and for the largest Hungarian international airport (LHBP), based on routine aviation weather reports (METARs) (*Bottyán et al.*, 2012; *Wantuch et al.*, 2013). *Fig. 2* presents the location of airports. The applied database contains the meteorological variables for every half hour from 2006. More than 30 variables have been introduced, including the parameters both in raw and derived formats (e.g., year, month, day, hour, minute vs. day of the year). The records are more than 99% complete, and the whole database is reproducible from raw METAR reports in short time with our script (*Bottyán et al., 2012*).

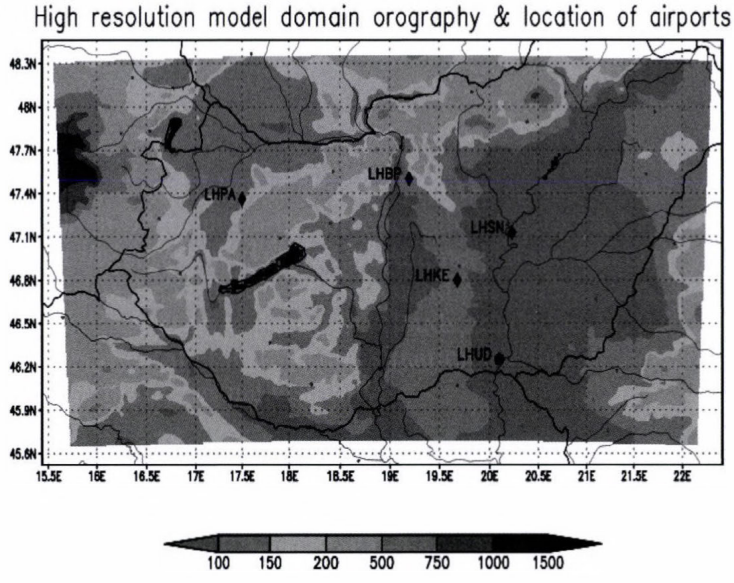


*Fig. 2.* Locations of four Hungarian airports inside the highest resolution, innermost (d03) model domain that were examined in the present study (black diamonds). LHKE: Kecskemét; LHSN: Szolnok; LHBP: Budapest; LHPA: Pápa. LHUD is the Szeged aerodrome (black dot), the location of field experiments.

The applied fuzzy logic based algorithm is measuring the similarity between the most recent conditions and the appropriate elements of the database. During the examination of every single weather situation, the model uses the current and the eleven previous METARs' content. The algorithm compares the meteorological variables of every examined time step using fuzzy sets *(Tuba et al.*, 2013b; *Wantuch et al.*, 2013).

The fuzzy sets – composed to describe the degree of similarity – were determined by experts (in this case by operational meteorologists), which is a common method in the development of fuzzy systems (*Meyer et al.*, 2002). These functions are applied for all compared parameters, to output the measure of similarity ranging from 0 to 1. The individual parameters at a given weather situation are examined one by one, and the overall measure of similarity for that situation is constructed from the weighted average of the individual measures of similarity of the parameters (*Tuba et al.*, 2013b).

Obviously, the initial values (or situation) of a given meteorological parameter from the most similar cases have determinative role in the forecast process. The higher the difference between initial values, the higher the risk of an inaccurate forecast of the selected element.

This led to our assumption: we could improve the accuracy of the forecast of individual elements by using appropriate weights highlighting the importance of them during the fuzzy logic based forecasting process (*Tuba et al.*, 2013b). As we have shown in our mentioned study: there are two different ways to highlight meteorological parameters which help to give more similar initial values for the parameters selected as more important. The first method is the suitable designation of fuzzy sets. Unfortunately, this approach is very difficult, because the expert judgments are hardly applicable on indirect way. In this case, they have to define the potential modification of the chosen fuzzy set in order to give a better prediction of the selected element. In another approach, we assign weights to the meteorological variables. The higher the importance of the parameter, the larger the applied weight. Because of the large number of variables, the direct determination of weights was excluded.

We applied the Analytic Hierarchy Process (AHP) introduced by *Saaty* (1977), which is a widely used technique in different fields of life except meteorology. This method is mainly used in multi-criteria decision making, especially in solving complex problems from most different fields (*Bardossy et al., 1993*; *Al-Harbi*, 2001; *Tuba et al.*, 2013a). Its main idea is to model the problem as a hierarchy. It is needed to define decision makers' goal, the applied criteria in decision making, which evaluates the possible alternatives and the alternatives to be chosen. In our case, the goal is to find the most similar situations in the database. Actually, it means the decision making. The conclusion of the lines above is that the alternatives are the single weather situations which are evaluated by the criteria: the different meteorological and time parameters. The meteorological problem to be solved has seven-seven

different criteria and sub-criteria, and more than 100,000 different alternatives. The large number of alternatives makes impossible to apply the whole analytic hierarchy process for finding the most similar situations, but for this we have the fuzzy logic based algorithm described above.

AHP was used only for determining the applicable weights for the different parameters as criteria. It was implemented by the first steps of AHP technique. Firstly, it is necessary to apply pairwise comparison on criteria which is based on general definition. In our case, these experts' judgments were assigned by operational forecasters' joint opinion. The ratios of pairwise comparisons can give the elements of a matrix. The best choice for the weight vector is the eigenvector belonging to the maximal eigenvalue of this matrix (see *Saaty*, 1977). To determine the eigenvector, we used the standard power iteration method. The received weights will be shown at the verification results. Obviously, the matrix might be inconsistent due to the subjective comparisons. We found an inconsistency of 2.5% which is less than the tolerable 10%, so the results are significantly reliable (*Saaty*, 1991).

Knowing the calculated weights we can determine the similarity of the individual time steps under investigation by weighted averaging of the single parameters' similarity. Finally, we calculate the overall similarity ($S_{overall}$) of the examined case from weighted averaging of the similarity of time steps. The current observation ($t-0$th time step) gets the largest weight, and this weight decreases rapidly as we go through time steps. It provides that the most similar cases probably contain the dynamic changes and guarantee the convergence in similarity during the examined time period. General description of the weighted averaging is the following:

$$S_{overall} = \frac{\sum_{n=1}^{k} \left(2^{n-1} \cdot S_{t-(n-1)}\right)}{2^{k}-1}, \qquad (1)$$

where $k$ is the number of the time steps applied in comparisons and $S_{t-(n-1)}$ is the similarity value of the $(t-(n-1))$th time step.

After finding the most similar weather situations, we can compose a deterministic prediction from the consecutive observations of the chosen cases with an appropriate method. The model collects the 30 most similar situations which are used for producing deterministic forecast. In the semi-operational phase, we used the 30th percentile value of the chosen parameter as prediction following *Hansen* (2007). We found that the percentile value is not independent from the examined parameter and the category limit of dichotomous forecast. We plan to investigate, if the verification results could be improved by dynamically changing percentile value in the function of category limits.

## *4. Numerical modeling in the IFS*

The Weather Research and Forecasting (WRF) model from the UCAR (*Skamarock et al.*, 2008) with the Advanced Research WRF (ARW) core, version 3.5 (release April 18, 2013) has been applied to generate numerical input for our NWP system.

WRF is a well-established, tested, and documented, non-hydrostatic, meso-scale meteorological model, applicable for both atmospheric research and weather forecasting purposes ranging from micro to global scales. Its modularity and flexibility together with its detailed documentation suited well for the needs of our purposes (*Passner et al.*, 2009). The modular structure of our development provides the possibility to swap one limited area model with another – e.g., ALADIN/AROME (*Hágel*, 2009; *Balogh et al.*, 2011; *Horányi et al.*, 2011, *Seity, et al.*, 2011) –to be used as a dynamical driver for the numerical unit of the system.

Input geographical dataset have been generated from two different sources. Landcover/land-use information were taken from the Corine 2000 (Coordinate information on the environment) database (*Büttner et al.*, 2002) adapted and modified for the applications in WRF by *Drüszler et al.* (2011). The main advantage of this database with respect to the USGS (United States Geological Survey) dataset (originally used by WRF) is the much more realistic and detailed representation of land characteristic features (e.g., much better and more specified representation of various types of forests and scrubland; in addition to more than 3 times larger area specified as urban land). These characteristics are essential in surface-atmosphere interactions and boundary layer processes, the most valuable input for aviation meteorology parameters.

Similarly, the original FAO (Food and Agriculture Organization) soil texture dataset has also been replaced by the DKSIS (Digital Kreybig Soil Information System), produced by the Center for Agricultural Research, Hungarian Academy of Sciences (see *Pásztor et al.*, 2010 for more details). The false over-representation of clay and loam type soils within the FAO data has been removed from the input data, and sand (absent from the original database) and sandy clay have been introduced in an additional extent covering more than 12% of the area of the country. The spatial distribution of the difference between the two different input data with respect to landuse (USGS vs. Corine 2000) and soil texture (FAO vs. DKSIS) geographical data fields are depicted in *Fig 3.* The most significant differences are the representation of urban area, water bodies and the under representation of evergreen forests in mountainous area, while with respect to soil texture. Contrarily to the Corine 2000 database, which covers whole Europe and can be applied to all model domains, DKSIS covers only the area of Hungary, inside the political boundaries of the country and is usable only for the best resolution (d03) domain (*Fig. 4*).

In addition, soil hydraulic parameters used by the WRF model were modified according to Hungarian soil sample data (MARTHA and HUNSODA), giving more realistic values for the soil structure in Central Europe (*Ács et al.*, 2010). Sensitivity tests showed that even during a sunny summer day, model results featured significant differences in terms of planetary boundary layer heights with respect to the soil hydraulic parameters that have been applied (*Breuer et al.*, 2012; *Ács, et al.*, 2014).

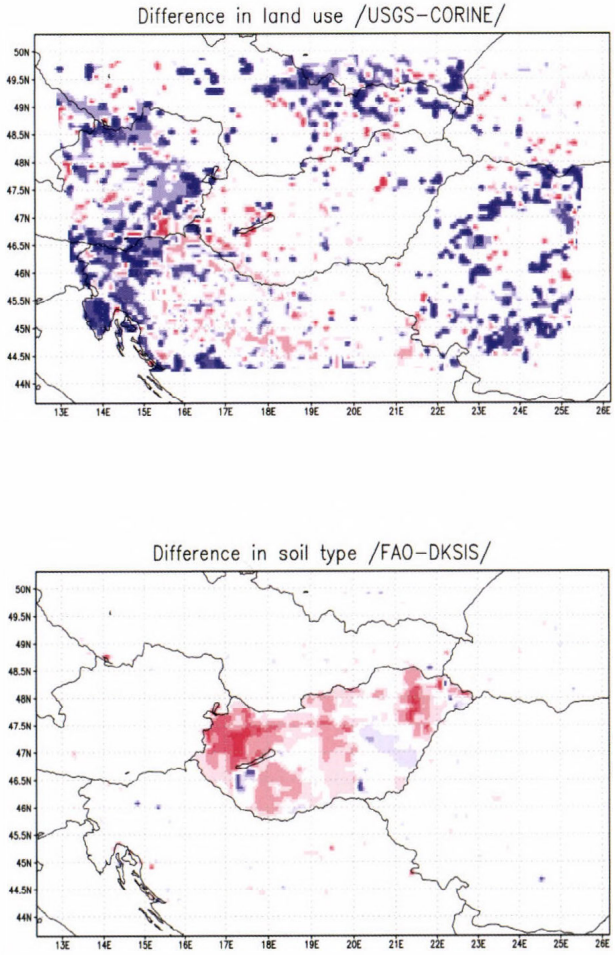


*Fig. 3.* Differences between the original and replaced geographical data with respect to land use (top) and soil texture (down) databases, applied for the integration of the WRF numerical weather model. Red (blue) shades indicate areas where the land use index has been increased (decreased), and white areas were not changed. It can be seen, that for soil texture, only the area inside the political boundaries of Hungary was modified.

The model setup in the newly developed IFS is the following. The number of vertical levels is 44, from which 24 levels are below 2 km. The vertical layers depth is ranging from 25–250m in the lower portion of the domain through 500 m layer in the middle levels up to 780 m in the upper portion of the model domain (see *Fig. 4*, left panel). Three level telescopic nesting is applied ranging from 22.5 km in the coarsest (d01) domain through 7.5 km in the intermediate (d02) domain to 2.5 km horizontal resolution in the high resolution lowest (d03) nested domain that is located in the Carpathian Basin (centered N47.43; E019.18) and covers Hungary with 202 × 121 grid cells (*Fig. 3.*, see also *Gyöngyösi et al.*, 2013 and *Fig. 4*, right panel).

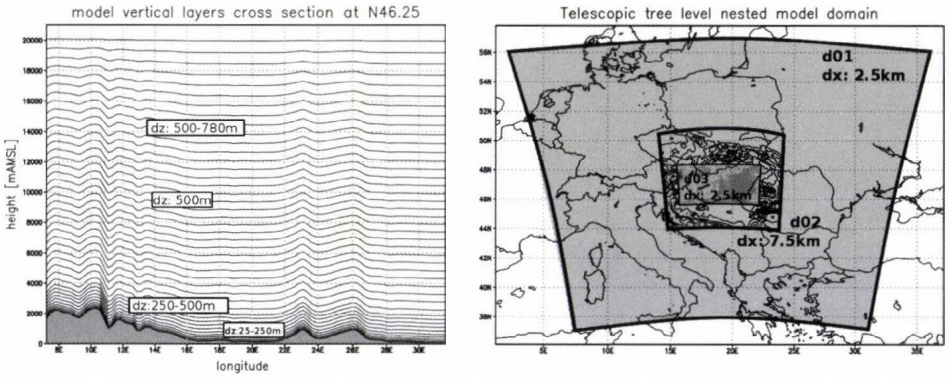


*Fig. 4.* Vertical levels with higher resolution in the lower levels and deeper layers in the upper portion (right panel) and the three level telescopic nested domain setup for high resolution modeling of the Carpathian Basin in the IFS system (left panel). Horizontal resolution is 22.5 km, 7.5 km and 2.5 km, grid size is 97 × 97, 97 × 97, and 202 × 121, respectively.

In order to apply a setup tuned for the special requirements of the designated purpose, extensive tests were performed: 30 different combination of parameterization setups (*Gyöngyösi et al.*, 2013) – including 8 types of micro-physics (types 3–9 and 13), 6 types of land surface models (types 1, 2, 4, 5, 7 and 10), and 8 types of PBL (1, 2, 4, 5, 7–10) schemes (see WRF-ARW Version 3 user's manual, *Wang et al.*, 2009) – have been tested. Tests have been performed for 9 selected weather situations, all having aviation weather relevancies (*Table 1*). Similar investigation has been made by *Hu et al.* (2010) for the optimization of the modeling of PBL processes with the comparison of three different parameterization schemes. An extensive test with a physical ensemble, using different parameterization setup (e.g., *Evans et al.*, 2012) requires enormous computational capacity, while in the current project we were focusing only to the study of a limited number of typical weather situations.

The test case studies investigated in the current test were chosen according to their aviation meteorology relevance, all of them are typical in the Carpathian Basin, including heavy icing, deep convection, abrupt wind direction change, etc. The list of the cases is detailed in *Table 1.*

*Table 1.* Test cases (date and short description) of weather situations for the evaluation of the numerical weather prediction unit

| No. | Date | Description |
|---|---|---|
| 1. | 10.27.2012. | Widespread precipitation from a Mediterranean low pressure system |
| 2. | 09.20.2012. | High horizontal pressure gradient situation with strong winds, with a special wind pattern |
| 3. | 01.19.2012. | Significant low-level inversion during winter period |
| 4. | 09.08.2012. | High pressure ridge transition resulting in significant and rapid change in wind direction |
| 5. | 07.29.2012. | Deep convection resulting in local and heavy showers that were not well resolved by most operational models |
| 6. | 05.12.2012. | Significant change in wind direction following a cold front |
| 7. | 01.22.2012. | Well documented severe icing case weather situation |
| 8. | 02.16.2012. | Convective precipitation from a high level cold vortex, temperature in the mid-troposphere is less than –25 °C |
| 9. | 12.06.2012. | UAS test flight case for direct verification purpose |

Model output have been compared to synoptic surface observations at 31 ground stations in Hungary located in the high resolution (d03) domain, and operational radiosonde data of 4 stations located in the medium resolution (d02) domain. Temperature, dew point, and wind data have been compared using RMS error and a wind score derived with respect to wind speed and wind direction differences. Results showed that in the surface data there is a wide variation in humidity and temperature, while in the upper level only wind speed and direction are significantly affected by the choice of the parameterization schemes.
From the analysis of the results the Bretherton and Park (2009) moist turbulence PBL scheme, the WRF Single Moment Scheme with 3 micro-physics class

(*Hong et al.*, 2004) and the Noah scheme (joint development of the National Centers for Environmental Prediction, Oregon State University, Air Force and Hydrologic Research Lab) for land-surface processes (*Chen* and *Dudhia*, 2001) performed the best. For parameterization the RRTM (Rapid Radiative Transfer Model) for longwave radiation (*Mlawer et al.*, 1997), the *Dudhia*'s (1989) scheme for shortwave radiation and a modified version of the Kain-Fritsch scheme (*Kain*, 2004) for cumulus convection parameterization have been applied.

GFS data with $0.5^{\circ} \times 0.5^{\circ}$ resolution was applied as initial and boundary conditions for the limited area integration of the outermost domain in every 3 hours, with no additional data assimilation. Soil temperature and humidity data were taken from GFS model as initial data only and were handled separately from meteorological data as boundary conditions, i.e., it is not updated from the large scale model during the integration. Appropriate adjustment of the lower boundary conditions to the physics of the model was achieved during the spin-up period in the beginning of the model integration. Input data was prepared with WPS, the vendor preprocessor of the WRF system.

This model setup has been considered as the best choice for the current purpose and it has been kept for operational integrations that are being run for 96 hours lead time, performed two times a day, initialized from 00 and 12:00 UTC, and 04:00 and 16:00 UTC, respectively. Data download of 1.5 GB input data from NOAA server takes 40 minutes, model preprocessing and integration on 24 cores for about half an hour, and post-processing for another 40 minutes. Model products are delivered to the users through the web interface of the integration server itself 6 hours after initialization time.

For the need of UAS forecasts, two different post-processors (ARWpost and the Universal Post-processor, UPP) are used. Output data is interpolated to both pressure levels (with UPP) and height levels (with ARWpost). Times series of predicted values at selected locations for (QNH) pressure; wind speed, direction (barbs), and wind gust; temperature, dew point, trigger temperatures for 1000 m and 1500 m deep thermal convection; grid scale and convective precipitation (both accumulated and intensity); and different level cloud amount, low-level cloud base (ceiling), and visibility forecasts are also published operatively (*Fig. 5a*).

In order to support UAS operation in the lower troposphere (from surface up to 3000 mAMSL) and above (up to 7000 mAMSL), evolution of vertical profiles (time-altitude cross-sections) of wind, temperature, lapse rate, and humidity are also plotted using shading and contouring at certain height levels (instead of pressure levels), that are easily interpretable by the user (*Fig. 5b*). Model prediction is presented in the usual form for the days of the intensive PBL observation period at Szeged, from in November 27–30, 2013 (*Cuxart et al.*, 2014; *Weidinger et al.*, 2014).

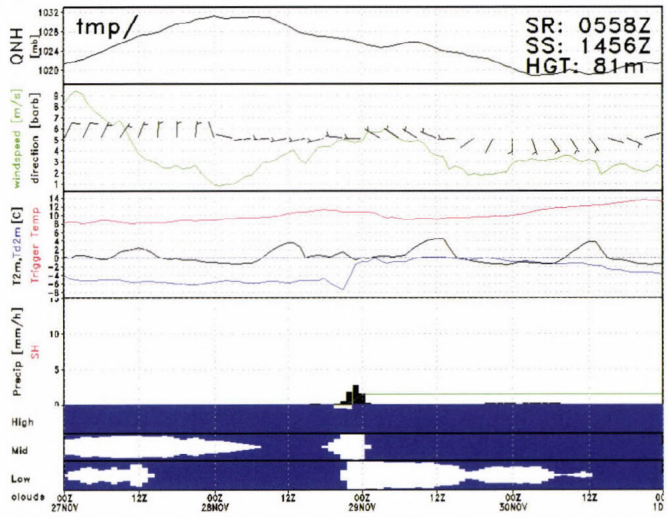


*Fig. 5a.* Meteogram graphical output of the predicted time variation of surface meteorological variables. Description of variables depicted on each panel, from top to bottom: sea level pressure (QNH), wind speed (green line, m $s^{-1}$) and direction (barbs), 2 m temperature (black line), dew point (blue line), and the calculated trigger temperature for a 1500 m mixed convective layer (red line), precipitation intensity (black bars), accumulated precipitation (green line), and low-, medium-, and high level cloud amount (white shaded area in the respective blue strips) with respect to time (UTC, horizontal axis), in the form as delivered to the users through the web based interface. Calculated sunrise and sunset times (UTC) are printed on the top right corner together with surface elevation.

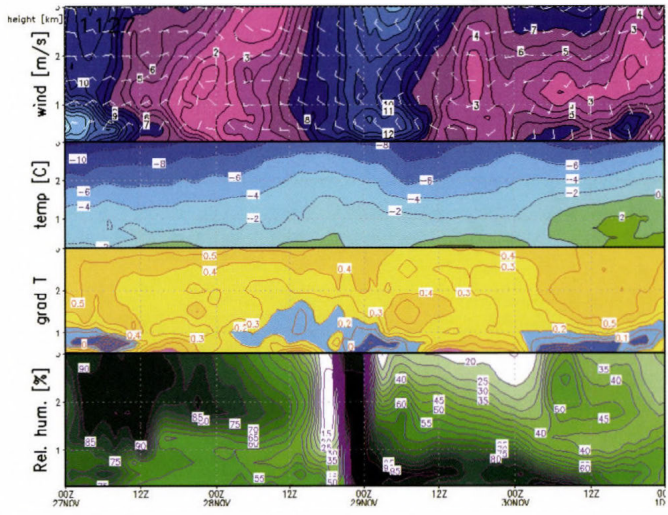


*Fig. 5b.* Same as *Fig 5a.* but for vertical profiles of atmospheric variables: wind speed and direction (barb), temperature, vertical temperature gradient (lapse rate, blue shades for absolute stable, yellow shades for conditionally unstable, and red shades for unstable stratification), and relative humidity.

In addition to basic model forecasts, time series of derived aeronautical weather parameters are also given (*Gyöngyösi et al.*, 2013). For example, predicted thermal characteristics (temperature advection, condensation level convective layer height, thermal index profile, and expected convective vertical velocity) can also be seen on a separate page for all locations. Visibility is computed using both the built-in scheme of UPP and the decision-tree based algorithm developed by *Wantuch* (2001), including FogSSI as a function of predicted temperature at the surface and 850 hPa level dew points ($T_d$) and the wind speed at 850 hPa.

Derived icing and turbulence forecasts are plotted on time-vertical cross-sections using different methods for the estimation of the intensity of processes (*Mireles et al.*, 2003; *Sousounis*, 2005; *Fövényi*, 2010).

### *5. Hybrid visibility forecasting in the IFS*

Applicability of statistical (i.e., analogy based) and numerical forecasting of visibility is limited. Analog forecasting is based on a special database and on the measured information of the actual ($t + 0$) weather and a short period before. Its efficiency (accuracy or reliability) decreases over time. On the other hand, the performance of NWP model is basically constant over the examined short forecasting period (nine hours time interval). The correlation coefficients between category differences – which are based on the difference of numerically predicted and observed visibilities (*Bottyan et al.*, 2013; *Wantuch et al.*, 2013) – at the initial ($t + 0$) and latter time steps show also gradual and significant decrease over time (*Fig. 6*). Five visibility categories are used within the 0 – 800 m, 800 – 1500 m, 1500 – 3000 m, 3000 – 5000 m, and above 5000 m intervals initially, the possible absolute category differences are 0, ±1, ±2, ±3, and ±4, respectively.

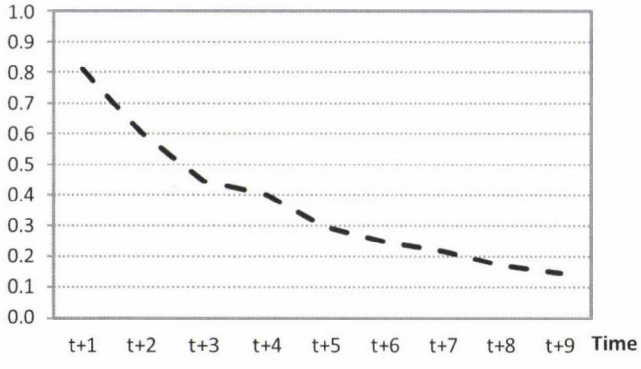


*Fig. 6.* Correlation coefficients of category differences between numerically predicted and observed visibility at the initial ($t + 0$) and latter time steps.

Preliminary results showed that the error of the initial time step is in close correlation with the latter inaccuracy of forecast from the same model run, but only for an ultra-short time period. This gave us the idea to combine the different methods during this period keeping their advantages and eliminating their disadvantages at the same time. This kind of models run only every 6 to 24 hours, thus the incorrect forecasts can be amended after the next model run which means the same loss of time. In contrast, the refresh rate of statistical forecasts fits the observation frequency which is not more than 1 hour. In consideration of the above, we created this hybrid model, which is from the simple linear combination of the statistical and numerical model outputs (*Tuba, 2014*):

$$Visibility_{HYBRID} = a \cdot Visibility_{STAT} + b \cdot Visibility_{NUM} , \quad (2)$$

where $a + b = 1$ and $a, b \in [0; 1]$. We specified that the statistical prediction weights should decrease

- with increasing category difference, because it corrects the potential initial inaccuracy of numerical model, and
- monotonically over time to provide the gradual transition between the statistical and numerical methods (*Bottyan et al.*, 2013).

On the basis of the above mentioned things, we can compose a weight matrix, with rows for the absolute category differences and columns for the time steps. *Table 2* gives an example for this kind of matrix with statistical model weights. Weights are optimized by verification parameters as absolute and root mean square error.

*Table 2.* The potential weights of statistical model are based on an experimental experts' first guess was examined on the LHSN data in the August 2013 and February 2014 period

| | | t+1 | t+2 | t+3 | t+4 | t+5 | t+6 | t+7 | t+8 | t+9 |
|---|---|---|---|---|---|---|---|---|---|---|
| **Absolute category difference** | **4** | 1.00 | 1.00 | 1.00 | 0.90 | 0.80 | 0.65 | 0.50 | 0.35 | 0.20 |
| | **3** | 1.00 | 1.00 | 0.90 | 0.80 | 0.70 | 0.55 | 0.45 | 0.30 | 0.20 |
| | **2** | 1.00 | 0.90 | 0.85 | 0.75 | 0.65 | 0.50 | 0.40 | 0.25 | 0.15 |
| | **1** | 0.90 | 0.85 | 0.80 | 0.70 | 0.60 | 0.45 | 0.35 | 0.20 | 0.10 |
| | **0** | 0.90 | 0.80 | 0.70 | 0.60 | 0.50 | 0.40 | 0.30 | 0.20 | 0.10 |

### *6. The Hungarian Unmanned Meteorological Aircraft System (HUMAS)*

In the Hungarian Unmanned Meteorological Aircraft System (*Mikó et al.*, 2009; *Szabó et al.*, 2013) for meteorological UAS measurements the BHE Bonn UAS has been mounted with the meteorological system as described below. The main features of the aircraft are the following: 16 kg total weight with 3 kg maximum payload, electrical propulsion that provides around 60–90 km/h IAS cruising speed, approximately 60–90 minutes duration, and more than 3000 mAGL flight altitude. The aircraft is equipped with a two-way microwave data communication system with a range of 15–20 km. The meteorological system is autonomous, independent of the UAS flight system, with its own power, GPS, IMU, and other sensors. It can be easily mounted on any other platform such as multi-copters or balloons.

The meteorological system is composed of a central unit and sensor units. The central unit (CU) is responsible for collection of the sensor unit (SU) data, pre-processing, and logging as well. The CU contains the power supply for the system, the onboard computer, and an UAS key for the data storage as shown below (*Table 3*).

*Table 3*. The structure of the central unit (CU)

| Device | Application |
|---|---|
| BeagleBone A6 single-board-computer | Pre-processing and logging. Features: 700MHz ARM Cortes-A8, Linux OS on micro SD card, 256MB DDR2 |
| Replaceable USB-key storage | Collecting of SU data |
| Power supply | Power supply for the independent meteorological measurement system. 7.4V, 3300mAh Li-Po with 2 cells providing > 6 hours duration depending on SU setup |

The SU contains all those instruments that necessary for collecting data usually provided by radiosondes. Because of the fast climbing and sinking rate during airborne measurements, it is necessary to sampling in a high frequency, particularly in temperature and relative humidity measurements (*Martin et al.*, 2011). According to this expectation, two sensors were placed on the HUMAS: a Vaisala HMP 45 (slow sampling) and a Texas Instruments TMP102 with a high frequency sampling rate (*Table 4.*). The sensors were mounted on the top part of the HUMAS's nose in a well perfused box (*Fig. 7*). The Vaisala probe was shielded with a white PVC tube with holes. The high sampling rate gave us an opportunity to measure not only vertical profile but temperature and relative humidity anomalies in up- and downdrafts during horizontal flight path (*Reuder et al.*, 2009).

*Table 4.* The structure of the sensor Unit (SU)

| Device | Measured variables | Derived variables | Sampling frequency (Hz) | Accuracy | Resolution |
|---|---|---|---|---|---|
| TMP102 | Temperature | | 10 | 0.5°C | 0.0625°C |
| HIH-4030 | Relative humidity | | 10 | ±3.5% | 0.5% |
| BMP085 | Pressure | Barometric altitude | 10 | ±1.0hPa | ±0.2hPa |
| GPS uBlox 6 SPK-GPS-GS407A 50 Channel | φ, λ | Ground speed, Track | 4 | | Horiz. <2.5m |
| 3-Axis MEMS accelerometer, 9-Axis MotionFusion | Euler angles (Θ, φ, ψ) | | 100 | 16384 LSB/g | ±16384 LSB/g |
| HMC5883L 3-Axis digital compass with Atmega328 microcontroller | Magnetic direction (MagX, MagY, MagZ) | Heading | 100 | 1370LBS /gauss | 1° |
| Vaisala HMP50 | T | | 1 | ±4.0% | 1% |
| Vaisala HMP50 | RH | | 1 | ±0.6°C | 0.1°C |
| Prandtl-tube with HCLA 12X5EU and HCA-BARO pressure sensor | Pdin, Pstat | IAS, Barometric altitude | 100 | ±6Pa, ±5mbar (baro.) | |
| 5HP with HCLA 02X5EB and HCLA 12X5EU pressure sensor | Pdin, Pstat | IAS, Barometric altitude, Angles of attack: α, β | 100 | ±2.5Pa | |

The system included GPS, accelerometer, digital compass, and the Prandtl-tube or the 5HP five holes probe that allowed us to apply several wind estimation methods, however, new methods were developed for wind measurements which have a lower instrumentation demand (*Szabó et al. 2013*). With the five holes probe (5HP) developed by the Technical University of Budapest (*Varga* and *Balczó*, 2013), high frequency 3D flow data became available (*Fig. 7*). With the combination of the measured 3D flow field and the temperature and humidity data, sensible and latent heat flow, could be investigated (*Bonin et al., 2013*).

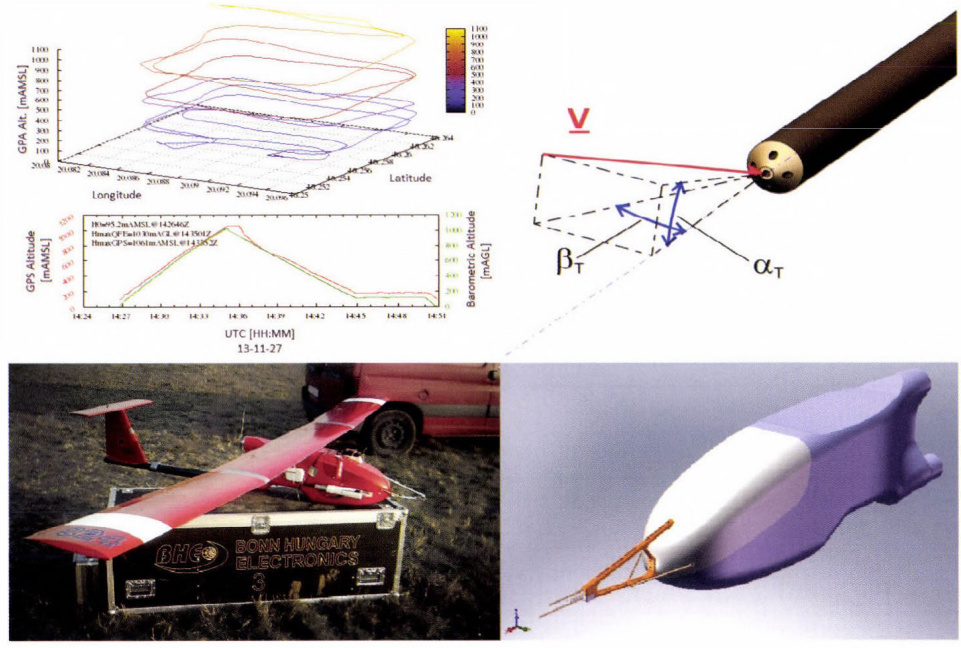


*Fig. 7.* Track of flight No. 4, Szeged, November 28, 2013 during the PABLS-2013 international measurement campaign (upper left), picture of the HUMAS (bottom left) and the 5HP pressure sensor (upper right) and its mounting on the nose of the HUMAS (bottom right).

## *7. Preliminary results and discussion*

After the description of the statistical, dynamical, and hybrid forecast system, followed by the presentation of the UAS based meteorological aircraft system, hereafter the applicability of the development will be demonstrated. In the following section the evaluation of the visibility forecast of a longer period of case is followed by the presentation of the preliminary results of an international atmospheric boundary layer observation campaign, where the system has been tested and performed suitable.

### *7.1. Visibility forecast*

In order to show the efficiencies of developed analog visibility forecasting model, the whole climatic database was divided into two different and

independent parts. The first one is for searching analog weather situations using fuzzy logic to the selected reports which are from the second dataset and they represent its every third hour. This control dataset contains the available and selected weather information of 2012. Nine-hour-long categorical forecast was examined (*Bottyán et al.*, 2013). The number and interval of categories are easily changeable in the verification template, so we can control the dependency of the results due to the different values.

*Doswell et al.* (1990) showed that there is no omnipotent verification method. For comprehensive verification of forecasts, it is advised to use several skill scores and verification parameters ($\alpha$, *BIAS*, *POD*, *POFD*, *FAR*, *HIT*, *CSI*, *TSS*, *HSS*, etc – see *Nurmi*, 2003). To the calculations we used a $2\times2$ contingency table of different categories of the parameter under verification (*Table 5*). As described in *Bankert* and *Hadjimichael* (2007): "Heidke skill score (*HSS*) is computed to measure the performance of each algorithm relative to random chance". Positive, zero, or negative *HSS* value indicates better, no better, or worse forecast performance than random chance, respectively. It is very important to note, that HSS values remain correct with verification of rare events, which is typical in case of low visibilities. According to the reasons, we present mainly the *HSS* values of visibility forecasts of the different prediction methods.

*Table 5.* Contingency table for categorical forecasts of binary events

| | | **Event observed** | |
|---|---|---|---|
| | | **YES** | **NO** |
| **Event forecasted** | **YES** | **a** (hit) | **b** (false alarm) |
| | **NO** | **c** (missed) | **d** (correct rejection) |

Some naive forecasts (e.g., persistence) can be a standard of reference *Murphy* (1992), or in other words, a competitive benchmark in the field of short term forecast verification. Thus, we show the verification results of persistence forecast on every figure for the comparability of outcomes. As it can be shown in *Fig. 8,* analog statistical forecast was generated for every third hour of the control period applying two different methods. Firstly, we did not use weights for highlighting the importance of the forecast element; secondly, we applied the calculated AHP weights. Each of them means almost 3000 model runs per examined airports (LHSN, LHPA, LHKE, and LHBP) in 2012.

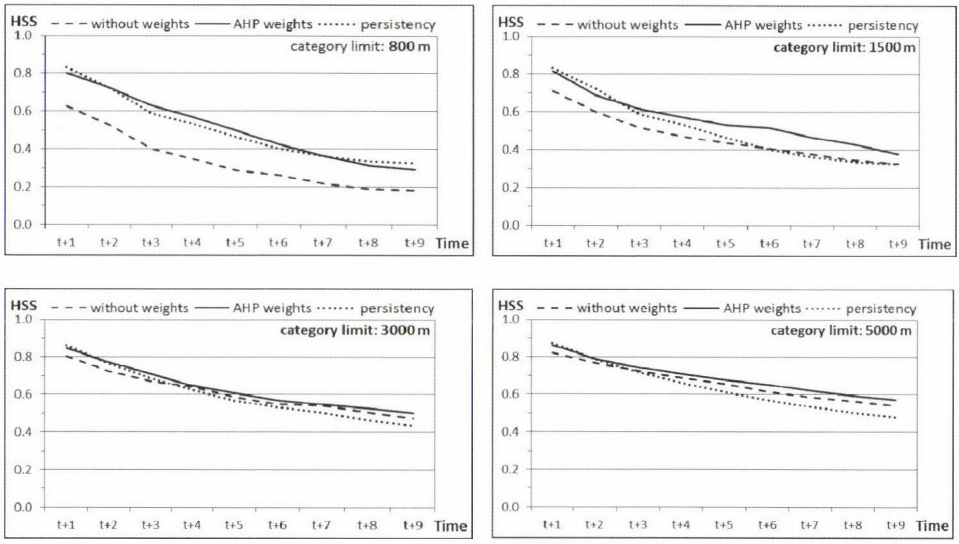


*Fig 8.* Average *HSS* of examined Hungarian airports (see *Fig. 2*) for predictions of different category limits and for the applied forecast methods for the year of 2012

Then we calculated the *HSS* values for both the methods and all of the examined category limits (800 m, 1500 m, 3000 m, and 5000 m), as well as the persistence forecast.

We found that application of AHP weights improved significantly the performance of analog forecasting during the whole nine-hour forecasting period. It is especially true in case of lower visibility ($\leq$ 1500 m). The applied AHP weights make analog forecasting highly competitive with persistence forecast in these categories.

In the following we show a case study, which represents how the hybrid model can correct the different visibility forecasts. On December 23, 2013, the synoptic situation over Central Europe was determined by anticyclonic effects. In Hungary, the weather was misty and foggy in several places day long. Only weak cold front touched the northern part of the country, and it caused some changes later. In Szolnok Airport (LHSN, 12860) there was broken or overcast ceiling at 4000 m during the previous night. Due to the clouds, the visibility decreased only to 3000 m. The clouds did not help the improvement of visibility during daytime. In the early evening hours the clouds became scattered, and due to the radiation, the visibility started to decrease rapidly, and finally dense fog formed by 21 UTC.

The most important part of this situation for us is the forecast period which starts at 15 UTC. The nine-hour time period covered the formation of fog. The

numerical forecasts were from the 12 UTC model run, and the statistical model used data from the 14:45 UTC and the previous observations. This case study intentionally uses the situation described aboave, when the numerical forecast is significantly different from the observation at the initial time step ($t + 0$). *Fig. 9* shows the observed and forecasted visibility values calculated by the different models.

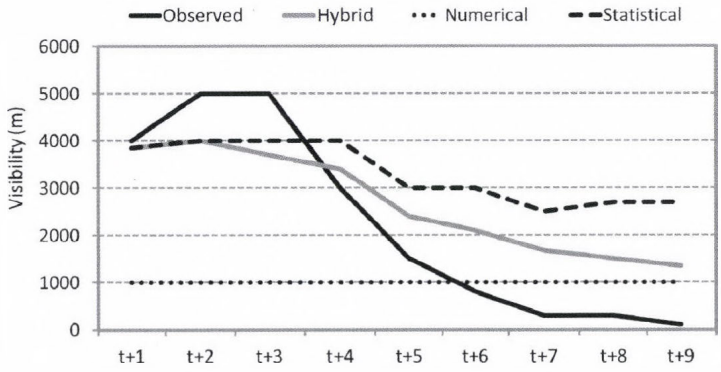


*Fig. 9.* The observed and different predicted visibility values for Szolnok Airport (LHSN, 12860) on December 23, 2013 ($t + 0 = 15$ UTC).

The lowest output value of the out-processing method of the numerical forecast is 1000 m. It means in the practice, that fog formed at the location. In the first part of the forecasting period, the numerical model significantly missed to correctly predict the visibility. In the second part, the statistical model missed to forecast the decreasing amount of clouds, and due to this, its visibility forecast was incorrect after that. In this situation, the hybrid model provides the best performance in forecasting visibility.

### *7.2. PBL profiles from HUMAS measurements and model forecasts*

In the following part of this section, the preliminary results of an international measurement campaign in late November, 2013 at Szeged, Hungary is discussed, on which the HUMAS has been deployed and performed suitable.

In the first iIntensive operation periods (IOP), on November 27 and 28, 2013, during the Pannonian Atmospheric Boundary Layer Experiment (PABLS-2013, in November 25–30, 2013), Szeged was located between a high pressure system over Central Europe and a low one over the Balkans. Airflow was from E-

NE to W-SW, and layer clouds between 800 m and 3000 m could be observed. Not far from the site, to the North of latitude N45.5°, the sky cleared up and remained clear during the whole night, but stayed overcast with occasional snow falls over Szeged. After 2300Z, precipitation stopped and cloud cover decreased from OVC to BKN, and finally to FEW clearing up until sunrise (0558Z). Altogether five different HUMAS measurement flights were performed before sunset and after sunrise. The main characteristics of the flights are summarized in *Table 6.* In this section, the WRF model results of the high resolution (d03) domain will be compared to UAS measurements, and also to other data from different sources with respect to temperature, humidity, and wind features.

*Table 6.* Main characteristics of the HUMAS flights during the PABLS-2013 measurement IOP1 on November 27–28, 2013. T/O time is the take-off time in UTC, Flt time is the flight time seconds, Hmax is the maximum height above ground level, achieved during the flight, T range, Rh range, and p range: temperature, relative humidity, and pressure maxima and minima, respectively

| No. | T/O time [day UTC] | Flt time [sec] | Hmax [m] | T range [°C] | Rh range [%] | p range [hPa] |
|---|---|---|---|---|---|---|
| 1 | 27. 10 29:19 | 847 | 530 | –3.4/2.5 | 66.8/88.1 | 955/1014 |
| 2 | 27. 12 49:37 | 674 | 483 | –2.4/2.9 | 66.4/81.9 | 961/1015 |
| 3 | 27. 14 26:46 | 1444 | 1030 | –5.9/5.9 | 62.4/93.9 | 901/1016 |
| 4 | 28. 06 04:28 | 2813 | 1979 | –6.3/-0.2 | 63.3/91.9 | 806/1020 |
| 5 | 28. 09 34:41 | 3166 | 2178 | –5.9/0.2 | 48.1/84.6 | 800/1021 |

Flight patterns have been selected to ensure maximum measurement accuracy with respect to meteorological variables, especially the calculation of wind components from GPS ground speed, (Prandtl-tube) IAS (indicated airspeed), and magnetic data. The flight path followed vertically staggered, quadratic path, keeping altitude for 3 legs and ascending/descending to the next level on the 4th leg, respectively (*Fig. 7*). Wind component speeds have been calculated from the ground speed differences on counter direction legs, and corrected with airspeed and magnetic data (*Cho et al.*, 2011; *Szabó*, 2014). In addition to onboard thermometers and humidity sensors, the UAS carried an additional Vaisala RS92-SGP radiosonde measuring unit for calibration purpose. During the IOP, the vertical flow structure of the site has been monitored with a SODAR equipment (METEK PCS.2000–24) in the lower 400 to 500 m layer.

From the comparisons, only for flight No. 4 will be presented here (*Figs. 10–11*). This flight has been carried out during the morning transition on the dawn after the night of 28 of November 2013.

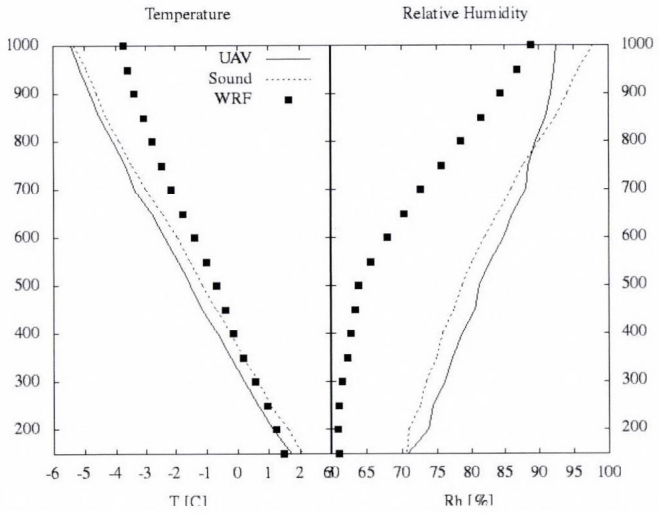


*Fig. 10.*Temperature and relative humidity data comparison. Measured data (HUMAS – solid line) is compared to measurements by operational Vaisala radiosonde device onboard of HUMAS (dotted line) and to the predicted data of the numerical weather model (high resolution, (d03) nested WRF domain – black squares). Flight No. 4, Szeged, November 28, 2013.

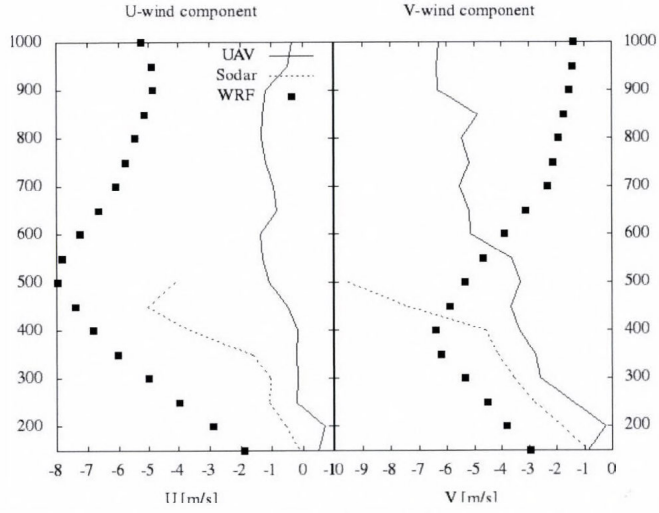


*Fig. 11.* Wind speed components *U* (zonal) and *V* (meridional) data comparison. Measured data (solid line) is compared to measurements by METEK PCS.2000-24 SODAR (dotted line) and to the predicted data of the numerical weather model (high resolution, (d03) WRF nested domain – black squares). Flight No. 4, Szeged, November 28, 2013.

In order to verify the measurements to standard meteorological sensors, temperature and relative humidity data were compared to a normal Vaisala RS92-SGP radiosonde unit that was carried onboard. From the qualitative comparison of *Fig. 10* it can be seen, that the temperature measurements were a little bit underestimated (negative bias), while humidity data provided by the HUMAS were a little higher than the reference, yielding an overestimation in the measurements. Comparing the measurements to modeled data shows that the model predicted more stability in the lower layer than the real temperature lapse rate, that might be a result of the under prediction of layer clouds and humidity (and of radiative cooling near surface) compared to realistic conditions in the lower layers. This sort of under-prediction in terms of humidity is clearly visible on the right panel as well, where the modeled relative humidity curve differs significantly from both measurements, especially in the lower 800 m layer. In *Fig. 11* data are presented in a manner same as in *Fig. 10* but for $U$ and $V$ wind components. Here the measured data has been compared to SODAR detection in the lower 500 m layer.

From the comparison of SODAR data to HUMAS measured wind data it can be seen, that there is a significant difference between the data over 300 m AGL. It should be noted however, that other wind measurements during this campaign yielded much better agreement to SODAR data than in this case, and the SODAR measurements over 300 m in certain meteorological conditions are slightly unreliable. Provided that the SODAR data are unreliable in this case over 300 m and if we consider the wind measurements of HUMAS as accurate, we can verify our model results to UAS measurement. It should be pointed out that the model predicted wind direction relatively precisely, but performed poorly in terms of wind speed, yielding in significant overestimation for wind speeds.

According to the preliminary results above, it should be pointed out that HUMAS proved to be a suitable platform for micro-meteorological in-situ measurement of the atmospheric boundary layer. Its operational costs and flexibility are much more suitable to the possibilities and needs of PBL measurements. As pointed out by *Passner et al.* (2009), *Marius et al.* (2012), *Stenmark et al.* (2014), for example, UAS measurements can yield valuable atmospheric data not only for experimental research but it may become an operational source of data for regional model calculations in the near future.

## *8. Conclusions*

Proper, detailed, and significant meteorological support is essential during the planning and executing phases of civilian and military UAS missions. For the smooth operation of such systems, it is very important to generate accurate, high-resolution, short-time predictions of ceiling, visibility, turbulence, icing, and other aviation meteorological factors.

The meteorological support system for UAS missions described in the current paper is based on the followings parts:

- an adequate data base of four Hungarian airports derived from freely accessible METAR data,
- application of statistical, dynamical, and special hybrid methods that can help the forecaster to give prognostic information for the UAS pilots and specialists,
- specially tuned and set-up numerical weather prediction model which can provide high resolution weather prediction over the Carpathian-basin,
- special post-processing system which is based on model products for the prediction of some hazardous weather phenomena such as low visibility and ceiling, turbulence, wind shear, icing etc.,
- a special web site to deliver adequate meteorological information in graphical, text and other formats via (mobile) web connection, and
- the first Hungarian meteorological UAS (HUMAS) specially equipped for the purpose of boundary layer measurements, which has been developed and successfully used during the mentioned project.

In the future, we can give the flight path optimization based on our predicted weather situation, and also we continue the development and testing of our UAS-based airborne meteorological measurement system.

***Acknowledgement:*** The authors thank *Károly Kazi* for using of Bonn Hungary Ltd's UAS system and *Péter Szalóky* for the AIRMET data set. Great thanks for providing the dataset during Pannonian Atmospheric Boundary Layer Experiment Szeged (PABLS-2013) to *Joan Cuxart Rodamilans*, *Gemma Simó Diego*, *Burkhard Wrenger*, *Dávid Tátrai*, *István Aszalos*, *Szabolcs Rózsa*, *Árpád Bordás*, *János Unger*, *János Józsa*, and *Melinda Kiss*. This research supported by the European Social Fund (TÁMOP-4.2.1.B-11/2/KMR-2011-0001 and TÁMOP-4.2.2.C-11/1/KONV-2012-0010 projects). Financial support by the Hungarian Scientific Research Foundation (OTKA, project no. K83909 and no. NN109679) is also gratefully acknowledged.

## *References*

*Ács, F., Horváth, Á., Breuer, H.,* and *Rubel, F.*, 2010: Effect of soil hydraulic parameters on the local convective precipitation. *Meteorol. Z. 19,* 143–153.

*Ács, F., Gyöngyösi, A.Z., Breuer, H., Horváth, Á., Mona, T.,* and *Rajkai, K.*, 2014: Sensitivity of WRF-simulated planetary boundary layer height to land cover and soil changes. *Meteorol. Z. 23*, 279–293

*Adams, S.M.* and *Friedland, C.J.*, 2011: A survey of unmanned aerial vehicle (UAS) usage for imagery collection in disaster research and management." 9th International Workshop on Remote Sensing for Disaster Response.

*Al-Harbi, K.M.*, 2001: Application of the AHP in project management. *Int. J. Proj. Manag. 19*, 19–27.

*Balogh, M., Horányi, A., Gyöngyösi, A.Z., André, K., Mile, M, Weidinger, T.,* and *Tasnádi P.* 2011: The ALADIN/CHAPEAU model as a new tool for education and inter-comparison purposes at the Eötvös Loránd University in Budapest. *HIRLAM Newsletter 58*, November 2011.

*Bankert, R. L.* and *Hadjimichael, M.*, 2007: Data Mining Numerical Model Output for Single-Station Cloud-Ceiling Forecast Algorithms. *Weather Forecast. 22,* 1123–1131.

*Bardossy A., Duckstein, L.* and *Bogardi, I.*, 1993: Combination of fuzzy numbers representing expert opinions. *Fuzzy Set. Syst. 57*, 173–181.

*Bonin, T., Chilson, P., Zielke, B.* and *Fedorovich, E.*, 2013: Observations of the Early Evening Boundary-Layer Transition Using a Small Unmanned Aerial System. *Bound.-Lay. Meteorol. 146*,119–132.

*Bottyán, Z., Wantuch, F., Tuba, Z., Hadobács, K.*, and *Jámbor, K.*, 2012: Repülésmeteorológiai klíma adatbázis kialakítása az UAV–k komplex meteorológiai támogató rendszeréhez. *Repüléstudományi Közlemények 24*, 11–18. (In Hungarian.)

*Bottyán, Z., Wantuch, F., Gyöngyösi, A.Z., Tuba, Z., Hadobács, K., Kardos, P.*, and *Kurunczi, R.*, 2013: Development of a Complex Meteorological Support System for UASs. *World Academy of Science, Engin. Technol. 7*, 648–653.

*Breuer, H., Ács, F., Laza, B., Horváth, Á., Matyasovszky, I.* and *Rajkai, K.*, 2005: Sensitivity of MM5-simulated planetary boundary layer height to soil dataset: comparison of soil and atmospheric effects. *Theor. Appl. Climatol. 109*, 577–590.

*Bretherton, C.S.* and *Park, S.*, 2009: A new moist turbulence parameterization in the Community Atmosphere Model. *J. Climate 22*, 3422–3448.

*Büttner, G., Feranec, J., Jaffrain, G., Steenmans, C., Gheorghe, A.*, and *Lima, V.*, 2002: Corine land cover update 2000. Technical guidelines. Copenhagen, Denmark: European Environment Agency.

*Chen, F.* and *Dudhia, J.*, 2001: Coupling an advanced land-surface/hydrology model with the Penn State-NCAR MM5 modeling system, part I, Model implementation and sensitivity. *Month. Weather Rev. 129*, 569–585.

*Cho, A., Kim, J., Lee, S.* and *Kee, C.*, 2011:, Wind Estimation and Airspeed Calibration using a UAS with a Single-Antenna GPS Receiver and Pitot Tube. *Aerospace Electronic sys. 47*, 109–117.

*Cuxart, J., Weidinger, T., Wrenger, B., Jimenez, M. A., Simo, G., Gomila, G., Warmers, H., Gyongyosi, A. Z., Istenes, Z., Bottyan, Z., Tatrai, D., Kiss, M.*, and *Jozsa, J.*, 2014: Joint Surface Budget Station, Tethered Balloon and RPAS Campaign SEABREEZE13 and PABLS13. ISARRA 2014 is held at Hans Christian Andersen Airport in Odense, Denmark, on May 26 to 28., http://www.isarra.org/isarra2014.html

*Doswell III, C. A., Davies-Jones, R.*, and *Keller, D. L.*, 1990: On summary measures of skill in rare event forecasting based on contingency tables. *Weather Forecast. 5*, 576–585.

*Drury, J.L., Riek, L.* and *Rackliffe, N.*, 2006: A decomposition of UAS-related situation awareness. In proceedings of the 1st ACM SIGCHI/SIGART conference on Human-robot interaction, New York, NY, USA, 88–94.

*Drüszler, Á; Vig, P.* and *Csirmaz, K.*, 2011: Impacts of Hungarian Land Cover Changes on the Regional Climate during the 20th Century. In: XXVth Conference of the Danubian Countries, Budapest, Hungary.

*Dudhia, J.*, 1989: Numerical study of convection observed during the Winter Monsoon Experiment using a mesoscale two-dimensional model. *J. Atmos. Sci. 46*, 3077–3107.

*Evans, J.P., Ekström, M.* and *Ji, F.*, 2012: Evaluating the performance of a WRF physics ensemble over South-East Australia. *Clim. Dynam. 39*, 1241–1258.

*Fekete, Cs.*, and *Palik, M.*, 2012: Introduction of the Hungarian unmanned aerial vehicle operator's training course. *Def. Res. Manage. 21st Cent. 1*, 55–68.

*Fövényi, A.*, 2010: Meteorológiai előrejelzések készítése sportrepülők részére numerikus modelladatok felhasználásával – régi és új módszerek adaptálása és automatizálása. *Repüléstudományi Közlemények 22* (Special Issue). (In Hungarian)

*Garcia, M., Viguria, A.*, and *Ollero, A.*, 2013: Dynamic Graph-Search Algorithm for Global Path Planning in Presence of Hazardous Weather. Dynamic Graph-Search Algorithm for Global Path Planning in Presence of Hazardous Weather. *J. Intelligent Robotic Sys. 69*, 285–295.

*Gertler, J.*, 2012: U.S. Unmanned Aerial Systems. Congressional Research Service. https://www.fas.org/sgp/crs/natsec/R42136.pdf.

*Gyöngyösi, A.Z., Kardos, P., Kurunczi, R.,* and *Bottyán, Z.,* 2013: Development of a complex dynamical modeling system for the meteorological support of unmanned aerial operation in Hungary. Proceedings of International Conference on 28 – 31 May 2013, Atlanta, GA, USA.

*Hansen, B.*, 2007: A Fuzzy Logic–Based Analog Forecasting System for Ceiling and Visibility. *Weather Forecast. 22*, 1319–1330

*Hadobács, K., Tuba, Z., Wantuch, F., Bottyán, Z.,* and *Vidnyánszky, Z.*, 2013: A pilóta nélküli légijárművek meteorológiai támogató rendszerének kialakítása és alkalmazhatóságának bemutatása esettanulmányokon keresztül. *Repüléstudományi Közlemények 25*, 405–421. (in Hungarian)

*Hágel, E.*, 2009: Development and operational application of a short-range ensemble prediction system based on the ALADIN limited area model. Ph.D. Thesis, Eötvös Loránd University, Faculty of Science.

*Hirardelli, J.E.G.,* and *Glahn, B.*, 2010: The Meteorological Development Laboratory's Aviation Weather Prediction System. *Weather Forecast. 25*, 1027–1051.

*Hong, S.-Y., Dudhia, J.,* and *Chen, S.-H.*, 2004: A Revised Approach to Ice Microphysical Processes for the Bulk Parameterization of Clouds and Precipitation. *Month. Weather Rev. 132*, 103–120.

*Horányi, A., Mile, M.,* and *Szűcs, M.*, 2011: Latest developments around the ALADIN operational short-range ensemble prediction system in Hungary. *Tellus A 63*, 642–651.

*Hu, X.-M., Nielsen-Gammon, J.W.,* and *Zhang, F.*, 2010: Evaluation of three planetary boundary layer schemes in the WRF model. *J. Appl. Meteorol. Climatol. 49*, 1831–1844.

*Jacobs, A.J.M.* and *Maat, N.*, 2005: Numerical guidance methods for decision support in aviation meteorological forecasting. *Weather Forecast. 20*, 82–100.

*Kain, J. S.*, 2004: The Kain–Fritsch Convective Parameterization: An Update. *J. Appl. Meteorol. 43*, 170–181.

*Marius, O.J, Ólafsson, H., Ágústsson, H., Rögnvaldsson, Ó.,* and *Reuder, J.*, 2012: Improving High-Resolution Numerical Weather Simulations by Assimilating Data from an Unmanned Aerial System. *Month. Weather Rev.140*, 3734–3756.

*Martin, S., Bange, J.* and *Beyrich, F.*, 2011: Meteorological profiling of the lower troposphere using the research UAS "M2AV Carolo". *Atmos. Measure. Tech. 4*, 705–716.

*Meyer, M.A., Butterfield, K.B., Murray, W.S., Smith, R.E.* and *Booker, J.M.*, 2002: Guidelines for eliciting expert judgment as probabilities or fuzzy logic. In (Eds.: *Ross, T.J., Booker, J.M.* and *Parkinson, W.J.*) Fuzzy Logic and Probability Applications: Bridging the gap. Society for Industrial and Applied Mathematics, 105–123.

*Mikó, G., Kazi, K., Solymosi, J.* and *Földes, J.*, 2009: UAS Development at BHE Bonn Hungary Ltd. 10th International Symposium of Hungarian Researchers on Computational Intelligence and Informatics, Proceedings. 2009, November 12-14, Budapest, Budapesti Műszaki Főiskola, 803–820.

*Mireles, M., Kirth, R., Pederson, L.* and *Elford, C. H.*, 2003: Meteorological Techniques (Revision 26 April 2006). No. AFWA/TN-98/002-REV. Air Force Weather Agency Offutt AFB NE.

*Mlawer, E.J., Taubman, S.J., Brown, P.D., Iacono, M.J.,* and *Clough, S.A.*, 1997: Radiative transfer for inhomogeneous atmospheres: RRTM, a validated correlated k-model for the longwave. *J. Geophys. Res.: Atmos. 102(D14)*, 16663–16682.

*Murphy, A., H.*, 1992: Climatology, persistence, and their linear combination as standards of reference in skill scores. *Weather Forecast. 7*, 692–698.

*Nurmi, P.*, 2003: Recommendations on the verification of local weather forecasts. The Library ECMWF Shinfield Park Reading, Berks RG2 9AX, 21 p.

*Østbø, M., Osen P., Rokseth, G., Homleid O. V.* and *Sevaldrud T.*, 2004: Exploiting meteorology toenhance the efficiency and safety of UAS operations. Forsvarets Forskningsinstitutt, Norwegian Defence Research Establishment FFI/RAPPORT-2004/00981, 50 p.

*Passner, J.E., Dumais, R.E., Flanigan, Jr. R.* and *Kirby, S.*, 2009: Using the Advanced Research Version of the Weather Research and Forecast Model in Support of ScanEagle Unmanned Aircraft System Test Flights. No. ARL-TR-4746, Computational and Information Sciences Directorate, ARL, 49 p.

*Pásztor, L., Szabó, J.* and *Bakacsi, Zs.*, 2010: Digital processing and upgrading of legacy data collected during the 1:25.000 scale Kreybig soil survey. *Acta Geodaetica et Geophysica Hungarica 45*, 127–136.

*Restás, Á.*, 2013: On Half Way between the Military and Civil Use - Disaster Management Supported by UAS Applications. In (Eds. *Bale, P., Alderson, R.)* AUVSI 2013 Exhibition and Conference, Washington, USA, 2013. August 12-*15*, 1–10.

*Restás, A.* and *Dudás, Z.*, 2013: Some aspect of human features of the use of Unmanned Aerial Systems in a disaster-specific division International Conference on Unmanned Aircraft Systems. (ICUAS), 2013_28-31 May 2013 in Atlanta, GA, USA, DOI: 10.1109/ICUAS.2013.6564791.

*Reuder, J., Brisset, P., Jonassen, M., Müller, M.* and *Mayer, S.*, 2009: The Small Unmanned Meteorological Observer SUMO: A new tool for atmospheric boundary layer research. *Meteorol. Zeit.18,* 141–147.

*Saaty, T.L.*, 1977: A scaling method for priorities in hierarchical structures. *J. Math.Psychol.15*, 234–281.

*Saaty, T.L.*, 1991: Some mathematical concepts of analytic hierarchy process. *Behaviormetrika 29*, 1–9.

*Seity Y., Brousseau P., Malardel S., Hello G., Bénard P., Bouttier F., Lac C.,* and *Masson V.*, 2011: The AROME-France Convective-Scale Operational Model. *Mon. Weather Rev. 139*, 976–999.

*Skamarock, W.C., Klemp, J.B., Dudhia, J., Gill, D.O., Barker, D.M., Duda, M.G., Huang, X-Y., Wang, W.* and *Powers, J.G.*, 2008: A description of the Advanced Research WRF Version 3. NCAR/TN-475 + STR NCAR Technical Note.

*Somlyai, L., Turóczi, A.* and *Molnár, A.*, 2012: Atmospheric analyser for mobile robots. *Computational* Intelligence and Informatics (CINTI), 2012 IEEE 13th International Symposium on Date 20–22 November, 2012 Budapest.

*Souders, C.G.* and *Showalter, R.C.*, 2008: Transformation of NAS to NEXTGEN and FAA's weather architecture impacts: an update. Aerospace Meteorology, AMS 88th Annual Meeting.

*Sousounis, P.J.*, 2005: Short term turbulence forecasts over the Atlantic Ocean using WRF. Preprints, World Weather Research Program Symposium on Nowcasting and Very Short Range Forecasting, September 5-9 2005. Toulouse, France.

*Stenmark, A., Hole, L.R., Voss, P., Reuder, J.* and *Jonassen, . M.O.*, 2014: The Influence of Nunataks on Atmospheric Boundary Layer Convection During Summer in Dronning Maud Land, Antarctica." *J. Geophys.Res. Atmospheres 119* (11) 6537–6548.

*Sun, X., Cai, C.* and *Shen, X.*, 2014: A New Cloud Model Based Human-Machine Cooperative Path Planning Method. *J. Intelligent Robotic Sys.*

*Szabó, Z. A.*, 2014: Pilóta nélküli repülőgépeken alkalmazható szondázási módszerek vizsgálata és fejlesztése. MSc Thesis, Department of Meteorology Eötvös Loránd University (In Hungarian).

*Szabó, Z.A., Istenes, Z., Gyöngyösi, A.Z., Bottyán, Zs., Weidinger, T.* and *Balczó, M.*, 2013: Sounding the planetary boundary layer with Unmanned Aerial Vehicles (UAS). *Repüléstudományi Közlemények 25,* 422–434. (In Hungarian.)

*Toth, Z.*, 1989: Long-Range Weather Forecasting Using an Analog Approach. *J.Climate 2*, 594–607.

*Tuba, Z., Bottyán Z., Wantuch, F. Vidnyánszky, Z.* and *Hadobács K.*, 2013a: Meteorological support model for meteorological support in military mission planning. *Hadmérnök 8*, 294–304. (in Hungarian)

*Tuba, Z., Vidnyánszky, Z., Bottyán, Z., Wantuch, F.* and *Hadobács, K.*, 2013b: Application of Analytic Hierarchy Process (AHP) in fuzzy logic-based meteorological support system of unmanned aerial vehicles. *Acad. Appl. Res. Military Sci. 12*, 221–228.

*Tuba, Z.*, 2014: Selected questions of Unmanned Aerial Vehicles (UASs) and visibility. *Repüléstudományi Közlemények 26*, 94–105. (in Hungarian)

*Varga, Á.* and *Balczó, M.*, 2013: Development of a multi-hole probe for atmospheric boundary layer Measurements. PHYSMOD 2013 – International Workshop on Physical Modeling of Flow and Dispersion Phenomena EnFlo Laboratory, University of Surrey, UK, 16th – 18 th September 2013. http://www.dapple.org.uk/Physmod.html

*Wang, W., Bruyère, C., Duda, M. G., Dudhia, J., Gill, D., Lin, H. C., Michalakes, J., Rizvi, S.* and *Zhang, X.*, 2009: WRF-ARW Version 3 Modeling System User's Guide, July 2009, Mesoscale & Microscale Meteorology Division, National Center for Atmospheric Research, Boulder, USA Tech. Note.

*Wantuch, F.*, 2001: Visibility and fog forecasting based on decision tree method. *Időjárás 105*, 29–38.

*Wantuch, F., Bottyán, Z., Tuba, Z.* and *Hadobács, K.*, 2013: Statistical Methods and Weather Based Decision Making in Meteorological Support for Unmanned Aerial Vehicles (UASs). Proceedings of International Conference on 28 – 31 May 2013, Atlanta, GA, USA.

*Watts, A.C., Ambrosia, W.G.* and *Hinkley, E.A.*, 2012: Unmanned Aircraft Systems in Remote Sensing and Scientific Research: Classification and Considerations of Use. *Remote Sensing 4*, 1671–1692.

*Weidinger, T., Cuxart, J., Gyongyosi, A.Z., Wrenger, B., Istenes, Z., Bottyan, Z., Simó, G., Tatrai, D., Jericevic, A., Matjacic, B., Kiss, M.* and *Jozsa, J.*, 2014: An experimental and numerical study of the ABL structure in the Pannonian plain (PABLS13). AMS, 21st Symposium on Boundary Layers and Turbulence. June 09 - 13, 2014, Leeds, United Kingdom. ams.confex.com/ams/21BLT/webprogram/21BLT.html

*Williams, K.W.*, 2004: A Summary of Unmanned Aircraft Accident/Incident Data: Human Factors Implications. Final report, Federal Aviation Administration Oklahoma City Ok Civil Aeromedical Inst., ADA460102, 17 p.

# IDŐJÁRÁS

*Quarterly Journal of the Hungarian Meteorological Service*
*Vol. 119, No. 3, July – September, 2015, pp. 337–354*


# Development, data processing and preliminary results of an urban human comfort monitoring and information system


**János Unger*, Tamás Gál, Zoltán Csépe, Enikő Lelovics, Ágnes Gulyás**

*Department of Climatology and Landscape Ecology, University of Szeged*
*P.O.Box 653, 6701 Szeged, Hungary*

**Corresponding author E-mail:* unger@geo.u-szeged.hu



*(Manuscript received in final form April 22, 2014)*



**Abstract**—In this study, the infrastructure development and operation of an urban human comfort monitoring network and information system in Szeged and the related preliminary research results are discussed. The selection of the representative sites of the network is based primarily on the pattern of the local climate zones in and around the city. After the processing of the incoming data (air temperature and relative humidity, as well as global radiation and wind speed), a human comfort index (PET) is calculated from the four meteorological parameters are with a neural network method (MLP), then the measured and calculated parameters interpolated linearly into a regular grid with 500 m resolution. As public information, maps and graphs about the thermal and human comfort conditions appear in 10-minute time steps as a real-time visualisation on the internet. As the preliminary case studies show, the largest intra-urban thermal differences between the LCZ areas in a two-day period occurred in the nocturnal hours reaching even 5 °C in early spring. In the spatial distribution of human comfort conditions, there are distinct differences in the strength of the loading or favorable environmental conditions between the neighborhoods during the daytime. Finally, the utilization possibilities of the results in the future are detailed.



*Key-words:* local climate zones (LCZ), representative measurement sites, monitoring network, psychologically equivalent temperature (PET), multilayer perceptron, thermal and human comfort maps, real-time visualization, Szeged, Hungary

## *1. Introduction*

Examination taking place in the field of urban environmental changes due to the large number of people affected is considered as an important task. The urban environments are specific – compared to the natural ones – because of the alteration in land cover and surface geometry characteristics as well as the human activity, which may significantly affect the energy and water balance of the area leading to local-scale climate modifications in the atmosphere of cities. As a result, the so-called *urban climate* develops (e.g., *Oke*, 1987). The residents are affected directly to the alterations taking place in the *urban canopy layer* (a layer of air between the average height of the buildings and the street level). The most significant modification is the change in the thermal environment (the *urban heat island* phenomenon, UHI), as well as in the human bioclimatic (thermal comfort) conditions influenced by the thermal environment and other weather parameters.

The importance of the investigation of these issues is supported that in cases of some of the already loading or unfavorable weather situations, the city still adheres to these effects. For example, at heat wave situations in cities the nocturnal cooling weakens, thus the periods characterized by significant physiological load are extended.

Within larger settlements due to the intra-urban heterogeneity of the physical attributes of the surface, the thermal modifying effect is also different. It can be assumed that in many respects, the interactions between the urban parameters and thermal comfort as well as some elements of the weather phenomena within the city are not yet known sufficiently. These interactions can only be analyzed properly using detailed and long-term (several years) measurements, like detection and analysis of the characteristics of these urban thermal patterns. This analysis can be performed with the help of a *monitoring network* installed representatively and in appropriate density. For automatic monitoring network set up in the urban canopy layer, there can be found some international – mainly U.S., Japan, and Taiwan – examples, while in Europe there are very few of these, and none of them are aimed at the detection of patterns of human comfort conditions. A network began to be build from 1999 on with temperature sensors located from the center in different directions radially in London (*Watkins et al.*, 2002), while in Florence, there is a system with temperature-humidity sensors operating since 2004, whose elements observe the thermal features of the city's various built-up districts (*Petralli et al.*, 2013). The most complex network (utilizing meteorological stations and sensors) so far was started up in 2011 in Birmingham. Its development is now in progress and its elements are installed at higher density in the downtown area while less densely in the outskirts of the city (HiTEmp Project, 2014).

However, obviously it is not a realistic option to establish monitoring stations network to all major urban areas, therefore, in the long run, the presentation and prediction of the prevailing thermal comfort conditions in urban areas only through the proper downscaling of weather forecasting models is possible. Development of such a method, however, is only possible using representative and high resolution measurement data in space and time, as well as parameters characterizing the urban surface and geometry in an appropriate manner. The forecasting of weather processes in urban areas – at least in the structure and functioning of the models used – is similar to the issue of climate change prediction. Because urban areas significantly influence the local climate, in order to estimate the possible outcomes of climate change, these areas should be taken into account. At the same time – as the majority of the world's population already lives in cities –, if the urban areas are implemented to climate models in appropriate manner and they are transposed to the climate models, it will be possible to have correct forecasts for these areas in the future.

In the present paper, we aim to show the principle and practice of the siting and configuration of a representative urban human comfort monitoring system and its data processing. Furthermore, we aim to present the preliminary results related to the spatial distribution of the intra-urban human comfort conditions and their real-time visualization as a public information, and finally, to show the utilization possibilities of the results in the future.

## *2. Local climate zones (LCZ), station place selection, monitoring network*

The main purpose of the LCZ system is the characterization of the local environment around a temperature measurement site in terms of its ability to influence the local thermal climate. Therefore, the number of types is not too large and their separation is based on objective, measurable parameters. LCZs are defined as "regions of uniform surface cover, structure, material, and human activity that span hundreds of meters to several kilometres in horizontal scale" (*Stewart* and *Oke*, 2012). Their names reflect the main characteristics of the types (*Table 1*).

The LCZ types can be distinguished by typical value ranges of measurable physical properties. These properties describe the surface geometry and cover (sky view factor, aspect ratio, fractions of building, pervious and impervious surfaces, height of roughness elements, terrain roughness class) as well as the thermal, radiative, and anthropogenic energy (surface admittance and albedo, anthropogenic heat output) features of the surface. As a result, the LCZ system consists of ten 'built' and seven 'land cover' LCZ types (*Table 1*). Although, originally it was not designed for mapping, mapping of the urban terrain the system can be efficiently used as to determine areas which are relatively homogeneous in surface properties and human activities.

In the context of the LCZ classification system, the UHI intensity is not an "urban-rural" temperature difference ($\Delta T_{u-r}$), but a temperature difference between pairs of LCZ types ($\Delta T_{LCZ\ X-Y}$), that is an inter-zone temperature difference (*Stewart et al.*, 2013). Consequently, the usage of the system allows the objective comparison of the thermal reactions in different areas within a city and between cities (intra-urban and inter-urban comparisons).

*Table 1.* Names and codes of the LCZ types (after *Stewart* and *Oke*, 2012)

| Built types | | Land cover types | |
|---|---|---|---|
| LCZ 1 | compact high-rise | LCZ A | dense trees |
| LCZ 2 | compact mid-rise | LCZ B | scattered trees |
| LCZ 3 | compact low-rise | LCZ C | bush, scrub |
| LCZ 4 | open high-rise | LCZ D | low plants |
| LCZ 5 | open mid-rise | LCZ E | bare rock / paved |
| LCZ 6 | open low-rise | LCZ F | bare soil / sand |
| LCZ 7 | lightweight low-rise | LCZ G | water |
| LCZ 8 | large low-rise | | |
| LCZ 9 | sparsely built | | |
| LCZ 10 | heavy industry | | |

### *2.1. LCZs in Szeged*

Szeged is located in the south-eastern part of Hungary (46°N, 20°E) at 79 m above sea level on a flat terrain with a population of 160,000 within an urbanized area of about 40 km$^2$. The area is in Köppen's climatic region Cfb with an annual mean temperature of 10.4 °C and an annual amount of precipitation of 497 mm (*Unger et al.*, 2001). The study area covers an 11.5 km × 8.5 km rectangle in and around Szeged (*Fig. 1*).

In order to apply the LCZ system in the study area, that is to delineate the types occurring therein, a recently developed automated method was used (*Lelovics et al.*, 2014). *Fig. 1.* shows the obtained seven 'built' and four 'land cover' LCZ types and their pattern in and around Szeged.

### *2.2. Installed and already existing stations*

Within the framework of an EU project (URBAN-PATH Project, 2014) a monitoring network with 23 stations (air temperature, *T* and relative humidity, *RH*) was set up in Szeged. Additionally, data series from the stations of the

Hungarian Meteorological Service (HMS) are added. One of them is at the same place where the station D-1 is located (global radiation, $G$ and wind speed, $u$) and the other is at the University of Szeged (station 5-1) ($T$, $RH$, $G$) (*Fig. 2*). Altogether, the whole network consists of 24 measurement sites.

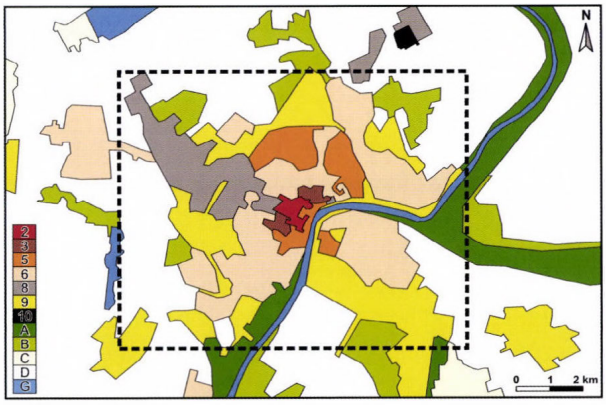


*Fig. 1.* The obtained LCZ map in Szeged (LCZ 2 – compact mid-rise, LCZ 3 – compact low-rise, LCZ 5 – open mid-rise, LCZ 6 – open low-rise, LCZ 8 – large low-rise, LCZ 9 – sparsely built, LCZ A – dense trees, LCZ B – scattered trees, LCZ C – bush, scrub, LCZ D – low plants, LCZ G – water) and the study area (broken line).


*Fig. 2.* Station locations of the urban monitoring network in Szeged with their notations (first number indicates the LCZ type, second one indicates the station number in a given LCZ type) (a – station, b – main road, c – water, d – urbanized area) (after *Lelovics et al.* 2014).

In order to have a representative urban human comfort monitoring network within the seven delineated 'built' LCZ areas, the siting and configuration of 22 stations from the above mentioned 24 ones were based on: (i) the distance of the site from the border of the LCZ zone within it was located; (ii) the ability of the selected network geometry to reproduce the spatial distribution of mean temperature surplus pattern estimated by an empirical model (*Balázs et al.*, 2009); (iii) the site's representativeness of its microenvironment; and (iv) the site's suitability for instrument installation. Thus, in summary, two stations (D-1, D-2) represent the rural area, while the other 22 stations the different built-up areas of the city (*Lelovics et al.*, 2014) (*Fig. 2*).

### *2.3. Measuring equipments*

In each monitoring station, the measurement is provided by a Sensirion SHT25 sensor in a radiation protection screen (220×310 mm) at the end of a 60 cm console. The accuracy of the sensor is 0.4 °C and 3% for the temperature and relative humidity, respectively. The radiation protection shield is the same as the model used by the HMS. The consoles are mounted on lamp posts at a height of 4 m above the ground for security reasons. As the air in the urban canyon is well-mixed, the temperature measured at this height is representative for the lower air layers too (but not for the air near the wall or ground) (*Nakamura* and *Oke,* 1988). At the beginning of the console, there are two boxes (*Fig. 3*). The upper one contains the central processor, data storage (microSD) card, GPRS/EDGE/3G modem, battery, and charger. The lower box is utilized in the case of 20 stations where the local electricity provider has made it possible to use the power for the station, and it contains only a separate power switch. At the remaining 4 stations, there is direct access to the power so they do not need any additional boxes.

*Fig. 3.* One of the stations of the monitoring network on a lamp post (temperature and relative humidity sensors are inside of the radiation shield cylinder).

The system time of the stations (and the whole monitoring system) is in UTC regularly synchronized by the main server. Most of the stations (17 items) have continuous power supply, but seven stations have power supply only when the city lights are on. These seven stations use the power of built in batteries during daytime or at power failure. These stations can operate up to 10 days using only battery power. The stations measure the parameters every minute, and they send the readings with some technical information (battery voltage, temperature inside the box, sensor status) into the main server (Dell PowerEdge T420 tower server) every 10 minutes. If there is no mobile internet connection or the main server does not receive the data, the station tries to send it repeatedly until it succeeded. If the station's battery level is low, the station increases the time between two data transfer to decrease the power consumption. One station (D-1) is located in the garden of the HMS station in order to provide calibration information for the network.

## *3. Data processing*

### *3.1. Calculation of the human bioclimatological index (PET)*

The human (bioclimatological) comfort sensation is formed as the complex effect of air temperature, air humidity, radiation and wind conditions. In order to characterize this comfort sensation, one of the rational indices, the physiologically equivalent temperature (*PET*) is used, which is defined as 'the temperature (in °C) of a standardized fictitious environment (where the mean radiation temperature is the air temperature, vapor pressure is 12 hPa, and wind speed is 0.1 $ms^{-1}$), in which the body, in order to maintain its energy balance, gives the same physiological responses like in the complex real-world conditions' (*Mayer* and *Höppe*, 1987).

The PET value categories were initially defined according to thermal sensations and physiological stress levels of Central European people, where the comfortable thermal heat sensation (no stress level) are indicated by a range of 18–23 °C (*Matzarakis* and *Mayer,* 1996). Furthermore, ranges of 13–18 °C and 23–29 °C mean slightly cool and slightly warm sensations, that is slightly cool stress and slightly heat stress levels, respectively, etc.

For the calculation of the PET index, an algorithm, the multilayer perceptron (MLP) network structure (*Haykin*, 1999) was developed (*Fig. 4*). It consists of neurons organized in layers. The neuron's differentiable outputs have non-linearity, which ensure that the output of the network is a continuous differentiable function of the weights. The output layer can be linear or non-linear. Even in the simplest case when an MLP contains only one hidden layer, it implements nonlinear mapping in his parameters. MLP use the error backpropagation learning algorithm, which is an iterative learning process based on an instantaneous gradient.

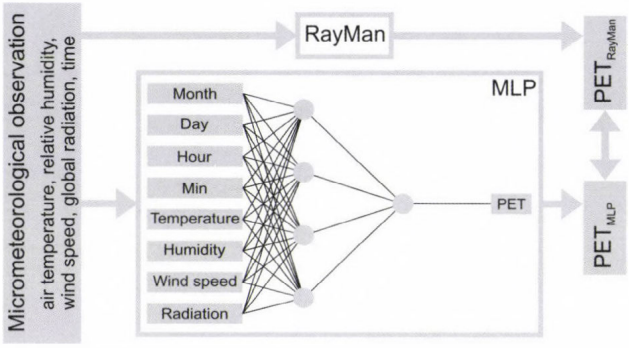


*Fig. 4.* Flow chart of the development of the MLP

In our case, the input data (air temperature, relative humidity, wind speed, global radiation, time) are derived from the results of the field measurements carried out in different urban microenvironments in Szeged between 2009 and 2013 (e.g., *Kántor* and *Unger,* 2010; *Égerházi et al.*, 2012a, 2012b) (*Fig. 4*). The target output data for the learning was a PET dataset calculated from the same input by the widely used RayMan software (*Matzarakis et al.,* 2007). The MLP model always has one hidden layer and MLP has several parameters that need to be set. They are training time, learning rate, hidden layers, and neurons in the layers. The training time was 1500 epochs, the learning rate started from 0.3 and it was reduced in each step. This helps to stop the network from diverging from the target output as well as to improve the general performance. The number of hidden layers and the nodes in each layer were generated automatically by the WEKA data mining software (*Hall et al.*, 2009). The MLP with these options was applied for predicting the PET index.

### *3.2. Estimation of the wind and global radiation*

For PET calculation in one site in the urban area, the wind speed and radiation data measured there would be ideal. In contrary, if the aim is the monitoring of the thermal comfort conditions in local scale, the direct measurement is not appropriate as the wind speed and radiation measured on site are highly affected by several micro scale phenomena like the arrangement of the nearby obstacles and their effect for the shading and wind flow. Moreover, the deployment of expensive wind and radiation sensors in every urban monitoring site is also not practical because of safety and financial reasons. By virtue of these reasons we used mean wind speed ($u_{UCL}$) in the urban canopy layer and the undisturbed global radiation ($G$). The height of the UCL is Szeged in assumed about 30 meters based on the available building database.

As we mentioned, in the study area, the global radiation data are available from the two HMS stations (sites D-1 and 5-1, see Section 2.3). For every monitoring sites, we used the nearest measured global radiation data.

Application of the different forms of logarithmic wind profile (*Oke*, 1987; *Foken*, 2008) for the reduction of the wind speed is prevalent in several thermal comfort studies (*Spagnolo* and *de Dear*, 2003; *Bröde et al.*, 2012). However, this method is questionable if the sum of the roughness length ($z_0$) and the displacement height ($z_d$) are higher than the height where we want to calculate the wind speed, because the logarithmic approximation gives 0 $ms^{-1}$ in these cases (*Oke*, 1987; *Foken*, 2008). Therefore, in our study we had to find another solution, because the values of the roughness parameters in urban area (*Gál* and *Unger*, 2009) exceed this limitation. For the estimation of the mean wind speed in UCL, we applied a new method developed for this purpose, however it is mainly based on the power law equation (*Counihan*, 1975):

$$u_1 = u_2 \cdot \left( \frac{z_1}{z_2} \right)^{\alpha}, \tag{1}$$

where $u_1$ and $u_2$ are the wind speeds at $z_1$ and $z_2$ heights, respectively, and $\alpha$ is estimated as a function of $z_0$:

$$\alpha \approx \frac{1}{\ln\left( \frac{\sqrt{z_1 \cdot z_2}}{z_0} \right)}. \tag{2}$$

Firstly, we used the Roughness Mapping Tool developed by *Gál* and *Unger* (2013). This is a standalone software for calculation the roughness parameters ($z_0$, $z_d$) using building and tree crown database. With this software we calculated $z_0$ and $z_d$ at the monitoring sites and 8 additional areas. These additional areas are the sites of the earlier thermal comfort studies in Szeged between 2009 and 2012 (*Égerházi et al.*, 2012a, 2012b; *Kántor et al.*, 2011, 2012), and for these areas 59 523 individual wind speed readings are available. We calculated the 10-minute average wind speeds ($u_{UCL}$) from the 1-minute data of these field measurements and compared them to the 10 minute average wind speed data ($u_{10}$) from the HMS station. We assumed that $u_{UCL}$ is constant inside the UCL and is equal to $u_{10}$. Finally, we got 1615 data pairs after filtering out the no- and very weak wind situations ($u<1$ $ms^{-1}$).

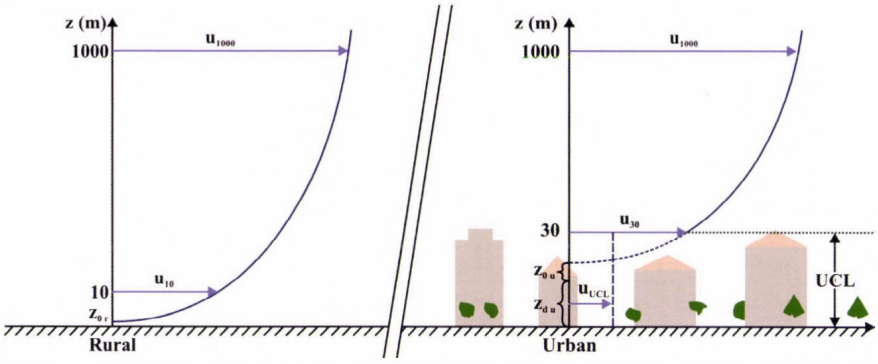


*Fig. 5.* Concept of the wind speed reduction (for explanation of symbols see the text).

Secondly, the wind speed at a height 1000 m ($u_{1000}$) was calculated from $u_{10}$ using the logarithmic formula assuming that this $u_{1000}$ value is the regional wind speed unaffected by the drag of the surface (*Fig. 5*). As a next step we determined the wind speed at the top of the UCL ($u_{30}$) and we calculated a constant ($k$) with the minimization of the mean square error (MSE) (*Scharf*, 1991) which describes the difference between $u_{30}$ and the measured $u_{UCL}$ (*Fig. 5*). This constant is 0.3331 (MSE=0.3284).

Finally, we obtained the following formula for the wind reduction:

$$u_{UCL} = u_{10} \cdot \left(\frac{1000}{10}\right)^{\alpha_1} \cdot \left(\frac{30 - z_{du}}{1000 - z_{du}}\right)^{\alpha_2} \cdot k \,, \tag{1}$$

where

$$\alpha_1 \approx \frac{1}{\ln\left(\frac{\sqrt{10 \cdot 1000}}{z_{0r}}\right)} \quad \alpha_2 \approx \frac{1}{\ln\left(\frac{\sqrt{(1000 - z_{du}) \cdot (30 - z_{du})}}{z_{0u}}\right)},$$

and subscripts $r$ and $u$ mark the rural and urban sites.

In Equation (1) all value are constants for a given station inside the urban area, except the $u_{10}$ what is measured in the rural station, therefore a complex wind reduction constant ($R$) was calculated for each monitoring site (*Table 2*) from the constants in this equation. We used this value to calculate the wind speed for the stations from the wind speed measured at D-1 (rural) station at the same time as the time of the PET calculation.

*Table 2.* Displacement height ($z_d$), roughness length ($z_0$), and complex wind reduction constant ($R$) at urban stations

| Station ID | $z_d$ (m) | $z_0$ (m) | $R$ |
|---|---|---|---|
| 2–1 | 8.7183 | 1.7455 | 0.2932 |
| 3–1 | 6.3586 | 1.4968 | 0.3116 |
| 5–1 | 6.0872 | 1.6751 | 0.3065 |
| 5–2 | 4.6924 | 2.2986 | 0.2937 |
| 5–3 | 7.6809 | 2.0346 | 0.2887 |
| 5–4 | 5.7750 | 2.8261 | 0.2765 |
| 6–1 | 1.7582 | 0.6740 | 0.3663 |
| 6–2 | 1.4402 | 0.4290 | 0.3856 |
| 6–3 | 1.0717 | 0.3134 | 0.3982 |
| 6–4 | 2.6706 | 0.8682 | 0.3521 |
| 6–5 | 3.4694 | 1.0783 | 0.3392 |
| 6–6 | 3.1466 | 0.9509 | 0.3463 |
| 6–7 | 1.5964 | 0.4782 | 0.3809 |
| 6–8 | 3.1734 | 1.1458 | 0.3372 |
| 6–9 | 1.5275 | 0.4108 | 0.3870 |
| 6–10 | 1.2339 | 0.5226 | 0.3784 |
| 8–1 | 1.8155 | 0.2798 | 0.4001 |
| 8–2 | 2.1910 | 0.2509 | 0.4028 |
| 9–1 | 0.1703 | 0.2000 | 0.4157 |
| 9–2 | 0.7589 | 0.2199 | 0.4111 |
| 9–3 | 0.2805 | 0.2000 | 0.4154 |
| 9–4 | 0.7641 | 0.2177 | 0.4115 |

### *3.3. Operational data processing and display*

After the transmission of the station data into the main server every 10 minutes, the automatic data procession system creates the final two (site and spatial) databases (*Fig. 6*) in order to make it possible to present these data as charts and maps on the public homepage of the project (urban-path.hu). Using this public display system, all of the measured and calculated parameters can be accessed a way that the time of the maps and charts can be freely modified by the visitors.

Data received from the monitoring network are stored in one text file per day on the server, and also stored in a MySQL database. Every 10 minutes a Java software calculates the PET value describing the human comfort conditions (see Section 3.1.) for each station using the temperature and relative humidity values measured there, as well as global radiation and wind speed data measured at the

HMS stations (*Fig. 6*). The results of this calculation are also stored in the MySQL database (*Fig. 6*). On the homepage the data, stored in the MySQL database are displayed by charts using PHP scripts.

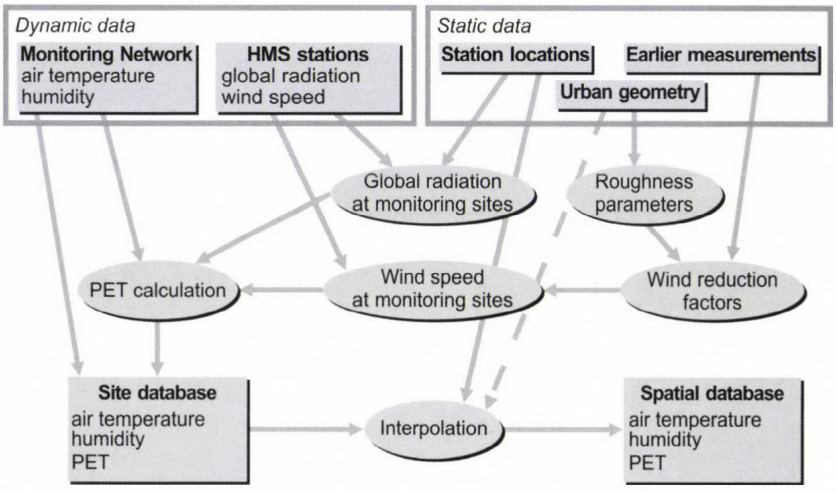


*Fig. 6.* Flow chart of the automatic data processing of the monitoring system.

For the automatic interpolation of the spatial patterns of the measured and calculated data, a Java software was developed. This program applies simple linear interpolation for a 500 m resolution grid of the study area using the data of the three nearest station of each grid point. In order to avoid the incorrect interpolation in the edge of the study area, the two rural stations are considered as background stations, thus, at the bordering (non-urban) grid points we used the data of the nearest rural station, and all of these points were added to the original measurement points for the interpolation (*Fig. 6*). The coordinates of the grid points and stations are in the Unified Hungarian Projection, but at the end of the interpolation they were converted to WGS84 latitude and longitude coordinates, because it is more appropriate for the further processing (drawing maps with GrADS, comparing the measurements with weather prediction models). At the first hand, we applied a weighting constant (currently it is 1) in the interpolation. After further investigations, we will alter this constant using the statistical connection between the surface parameters (e.g., built-up ratio, SVF, green area, water surface) and the measured temperature, relative humidity, or PET values in order to increase the precision of the interpolation (*Fig. 6*). The final patterns are stored in another, spatial database, which is

technically a NetCDF file. The public project homepage presents these patterns as maps created by GrADS and PHP scripts.

## *4. Intra-urban variation of the measured and calculated parameters*

In this section, the intra-urban differences in the thermal and human comfort conditions are illustrated in selecting time periods, when the weather conditions promoted the microclimatic effects of the spatially varied surface features.

### *4.1. Temperature data series – comparison of LCZs' thermal reactions*

The distinct thermal behavior of the different LCZ areas is shown during a 48 h cloudless period between March 29 and 31, 2014 (from morning to morning) as an example. This period is characterized as a pleasant spring weather. According to the data of the rural HMS station, the insolation was undisturbed during the daylight hours with maximum values of 750–780 $Wm^{-2}$. The air movement was moderate (0–3 $ms^{-1}$) except of the first few (daytime) hours (~4–5 $ms^{-1}$). The days were rather warm with maximum values of 18–20 °C, but the mornings were a bit chilly with the minimum values of 2–4 °C because of the intense nocturnal cooling provided by the cloudless sky.

In order to compare the temperature variations of LCZs during the 48 h period, the areal averages were calculated for every LCZ area. As the number of stations located at these areas is different because of the different areal extent of LCZs (from one station in LCZ 2 to ten in LCZ 6, see *Fig. 2*), the *T*-averages are calculated based on original data with different number of sites. As a result seven temperature series are compared ($\Delta T_{LCZ\ X-Y}$), in accordance with the number of LCZs in the study area (except 'heavy industry' (*Fig. 7*).

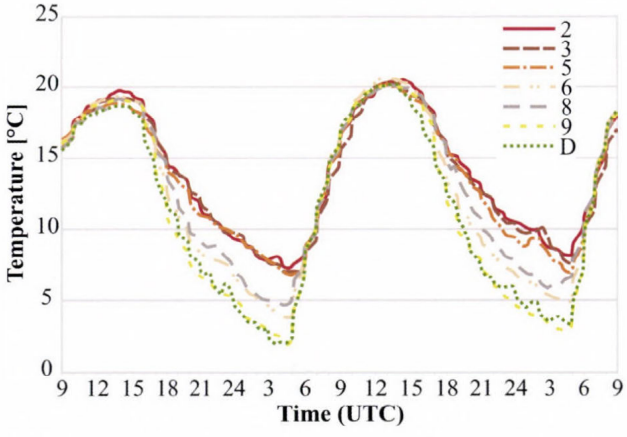


*Fig. 7.* Temporal variation of the mean LCZ temperatures during a 48 h period (March 29–31, 2014).

As *Fig. 7* shows, the *T*-curves follow the regular shape of the daily temperature cycle in spring, that is warming in the daytime until early afternoon (~8–10 hours) then cooling until dawn (14–16 hours). As expected, LCZ 2 area is the warmest and LCZ 9 and LCZ D types are the coolest, but this is really prevalent at night, as in the daytime the curves move almost together. The largest temperature differences occur in the nocturnal hours: for example, at 4.30 UTC, $\Delta T_{LCZ\ 2\text{–}D} \sim 5$ °C, $\Delta T_{LCZ\ 5\text{–}D} \sim 4.5$ °C, but $\Delta T_{LCZ\ 8\text{–}D} \sim 2{,}5$ °C only, while $\Delta T_{LCZ\ 9\text{–}D} \sim 0$ °C at both nights. This can be explained by the slower cooling of the built-up areas compared to the open and more vegetated rural areas because of the radiation processes at the mentioned weather conditions.

### *4.2. Maps on temperature, relative humidity, and human comfort*

During the processing of incoming data (see Section 3), high resolution maps are produced automatically showing the spatial structures of the thermal, humidity, and human comfort conditions, which appear on the project website continuously updated in 10-minute intervals (online) from June 2014.

As an example, in the case of air temperature and relative humidity, we present the situations in the evening hours (*Fig. 8*). That day was also a typical nice spring one with some cloud drift, so the global radiation was a bit disturbed, therefore in the most intensive period, it varied between 550 and 780 Wm $^{2}$. The temperature reached 19°C at the rural HMS station and it was about 10 °C at 20:00 UTC. The daytime wind speed was 2–3 ms$^{-1}$, then it decreased to about 1 ms$^{-1}$ in the evening.

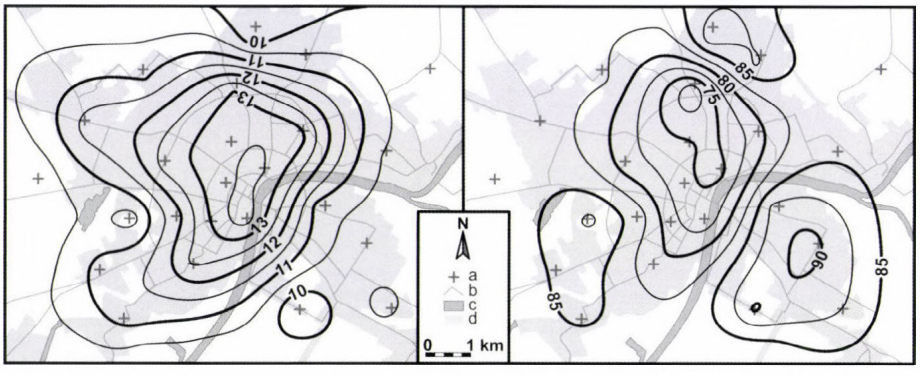


*Fig. 8.* Intra-urban patterns of temperature (°C) and relative humidity (%) at 20:00 UTC, April 7, 2014 (a – station, b – main road, c – water, d – urbanized area).

The *T*-pattern shows a typical 'island-like' shape with a maximum of over 13.5 °C in the inner city. The values decrease toward the outskirts to about 10 °C (as mentioned above in the case of rural HMS stations). A small deviation from the quasi-concentric shape can be found in the western parts of the city, where small lakes and large green areas are predominant. An opposite case can be experienced for the RH: the largest values (85–90%) occur in the periphery and the smallest ones (under 75%) in the inner parts stretching a bit toward the hosing estates in the north-eastern parts of the city. The shape of the temperature pattern is mostly similar to the results of the previous UHI measurement campaign in Szeged (*Unger et al.*, 2001; *Balázs et al.*, 2009), thus the selection of the sites was really representative.

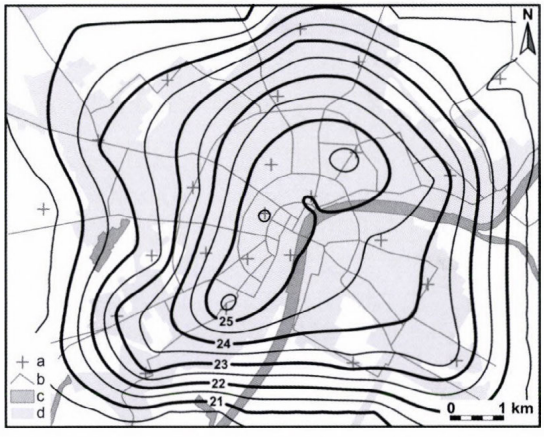


*Fig. 9.* Intra-urban pattern of human comfort conditions (PET °C) at 12:00 UTC, April 7, 2014 (a – station, b – main road, c – water, d – urbanized area).

In the case of human comfort conditions, the *PET*-pattern for the daytime (12:00 UTC) is presented. At that time, the distribution of temperature (not shown) is almost homogeneous in the study area (with a variation of less than 0.5 °C around 17 °C), but in the *PET* values a range of 20.5–25.5 °C occurs. Accordingly, there is comfortable thermal heat sensation (no stress level) in outer parts of the city (below 23 °C *PET*), and much of the city has been experiencing a very slightly warm sensation (slight heat stress level) (from 23 to 25.5 °C *PET* in the inner parts). Consequently, already in this nice and not too warm early spring day, the environmental conditions in the inner urban parts can be a bit loading for the people. This can be explained by the altered wind conditions (lower wind speeds in the inner urban parts) with rather uniform insolation. This (thermal) load could be strengthened by the fact that after the colder winter days, the thermal contrast (e.g., stronger sunshine) is rather large for the unprepared (not accustomed) people staying outdoors.

## *5. Conclusions and outlook*

Based on this study, the following conclusions can be drawn in accordance with the aims set in Section 1.

Besides the two already existing measurement points, 22 additional sites were selected within the seven delineated local climate zones in Szeged in order to develop a representative urban human comfort monitoring network and information system.

The incoming data (*T*, *RH* from 24 stations, *G*, *T*, and *RH* from the urban HMS station, as well as *G* and *v* from the two HMS stations) were processed by the following steps: firstly, G estimation for each station where it is not measured, then wind reduction for each station using roughness parameters and logarithmic wind profile, and final adjustment using previous street-level wind measurements. Secondly, PET calculation from the four meteorological parameters with a neural network method (MLP) was processed, followed by a linear interpolation of the measured and calculated parameters into a regular grid with 500 m resolution.

As public information, the maps about the thermal and human comfort conditions, and additionally, different graphs about the temporal variations of *T*, *RH*, and PET value appear in 10-minute time steps as a real-time visualization on the project homepage (URBAN-PATH Project, 2014).

According to the preliminary outcomes as case studies, the largest intra-urban thermal differences between the LCZ areas in a two-day period occurred in the nocturnal hours reaching even 5 °C in early spring. These results confirm the findings of *Stewart* and *Oke* (2012), that is the thermal influence of any change or difference in landscapes (e.g., the different levels of urbanization) are better demonstrated using LCZ difference concept than a simple but generally not clear urban-rural approach, and additionally, it provides an opportunity for intra- and inter-urban comparisons. In the spatial distribution of human comfort conditions, there are distinct differences in the strength of the loading or favorable environmental conditions between the neighborhoods during the daytime. As the inhabitants can meet large differences even within relatively short distances, the urban areas can not be considered homogeneous from this respect.

In summary, as a result of the infrastructure development and related research in the frame of the URBAN-PATH project, an operating urban human comfort monitoring network and information system was established in Szeged.

The utilization possibilities of the results in the future are related to the high-resolution weather prediction models which can be applied in the urban environments – these are real alternatives of urban climate measurement networks –, but their results are not adequate enough so far (*Case et al.*, 2008; *Chen et al.*, 2011; *Salamanca et al.*, 2011). Real time predictions of urban meteorological environment are based not only on the attributes of static urban parameters (built-up ratio, sky-view factor, building heights, etc.), because these data are basically constant in the prognostic time-scales. On the other hand, the

actual weather of a given urban region strongly depends on physical processes working in macro- and meso-scales. The mentioned processes can be taken into account only using a well-defined, telescopic downscaling method with the help of a high resolution numerical weather prediction model (such as WRF). Today these high resolution models are directly able to predict the urban meteorological effects and give adequate data for a complex urban weather prediction system. Nevertheless, the basic urban surface data sets and their attributes which are needed to make a successful forecast will have to be specified. Since the urban weather factors mainly work on meso-$\gamma$ and micro-$\alpha$ scales, the applied numerical model will be able to run with 300 m horizontal resolution and dense vertical layering. Based on the mentioned challenges, it is important to implement a high-resolution urban static database into the WRF system moreover, the global and local (urban) meteorological data assimilation procedures are required. An WRF-based urban meteorological prediction system can be able to give fundamental data for some new research aspects such as military, urban planning, public health, etc., applications.

***Acknowledgements:*** The study was supported by the Hungary-Serbia IPA Cross-border Co-operation Programme (HUSRB/1203/122/166 – URBAN-PATH), in case of the second author by the Hungarian Scientific Research Fund (OTKA PD-100352) and by the János Bolyai Research Scholarship of the Hungarian Academy of Sciences, and in case of the fourth author by the TÁMOP 4.2.4. A/2-11-1-2012-0001 „National Excellence Program – Elaborating and operating an inland student and researcher personal support system convergence program", which project was subsidized by the EU and co-financed by the European Social Fund.

## *References*

*Balázs, B., Unger, J., Gál, T., Sümeghy, Z., Geiger, J.,* and *Szegedi, S.*, 2009: Simulation of the mean urban heat island using 2D surface parameters: empirical modeling, verification and extension. *Meteorol. Appl. 16,* 275–287.

*Bröde, P., Fiala, D., Błażejczyk, K., Holmér, I., Jendritzky, G., Kampmann, B., Tinz, B.,* and *Havenith, G.*, 2012: Deriving the operational procedure for the Universal Thermal Climate Index (UTCI). *Int. J. Biometeorol. 56,* 481–494.

*Case, J., Crosson, W., Kumar, S.V., Lapenta, W.M.,* and *Peters-Lidard, C.D.*, 2008: Impacts of high-resolution land surface initialization on regional sensible weather forecasts from the WRF model. *J. Hydromet. 9,* 1249–1266.

*Chen, F., Kusaka, H., Bornstein, R., Ching, J., Grimmond, C.S.B., Grossman-Clarke, S., Loridan, T., Manning, K.W., Martilli, A., Miao, S., Sailor, D., Salamanca, F.P., Taha, H., Tewari, M., Wang, X., Wyszogrodzki, A.A.,* and *Zhang, C.*, 2011: The integrated WRF/urban modelling system: development, evaluation, and applications to urban environmental problems. *Int. J. Climatol. 31,* 273–288.

*Counihan, J.*, 1975: Adiabatic atmospheric boundary layers: A review and analysis of data from the period 1880-1972. *Atmos. Environ. 9,* 871–905.

*Égerházi, L., Kántor, N., Takács, Á.,* and *Unger, J.*, 2012a: Patterns of attendance and thermal conditions on a pedestrian street. Proceed of the 8th Int. Conf. on Urban Climate. Dublin, Ireland, Paper no. 170.

*Égerházi, L., Kántor, N., Takács, Á., Gál, T.,* and *Unger, J.*, 2012b: Thermal stress maps validation with on-site measurements in a playground. Proceed of the 8th Int. Conf. on Urban Climate. Dublin, Ireland, Paper no. 169.

*Foken, T.*, 2008: Angewandte Meteorologie. Springer, Berlin–Heidelberg.
*Gál, T.* and *Unger, J.*, 2009: Detection of ventilation paths using high-resolution roughness parameter mapping in a large urban area. *Build. Environ. 44*, 198–206.
*Gál, T.* and *Unger, J.*, 2013: Calculation of the aerodynamical roughness parameters using building and tree-crown database. In (eds: *Pajtókné Tari I, Tóth A.)* Changing Earth, Changing Society, Changing Learning – The role of renewable energy in regional development Int. Conf. Eger, Hungary, 43–48.
*Hall, M., Frank, E., Holmes, G., Pfahringer, B., Reutemann, P.*, and *Witten, I.H.*, 2009: The WEKA data mining software: an update. *ACM SIGKDD Explorations Newsletter 11*, 10–18.
*Haykin, S.*, 1999: Neural Networks: a comprehensive foundation (2nd ed.). Prentice Hall, Upper Saddle River, NJ.
HiTemp Project, 2014: High Density Measurements within the Urban Environment. http://www.birmingham.ac.uk/schools/gees/centres/bucl/hitemp/index.aspx. Last accessed: April 10, 2014.
*Kántor, N.* and *Unger, J.*, 2010: Benefits and opportunities of adapting GIS in thermal comfort studies in resting places: An urban park as an example. *Landsc. Urban Plan. 98*, 36–46.
*Kántor, N., Gulyás, Á., Égerházi, L.*, and *Unger, J.*, 2011: Assessments of the outdoor thermal conditions in Szeged, Hungary: thermal sensation ranges for local residents. In (eds: *Gerdes, A., Kottmeier, C.* and *Wagner, A.*) Climate and Construction Int. Conf. Karlsruhe, Germany, 181–190.
*Kántor, N., Égerházi, L.*, and *Unger, J.*, 2012: Subjective estimation of thermal environment in recreational urban spaces—Part 1: investigations in Szeged, Hungary. *Int. J. Biometeorol. 56*, 1075–1088.
*Lelovics, E., Unger, J., Gál, T.*, and *Gál, C.V.*, 2014: Design of an urban monitoring network based on Local Climate Zone mapping and temperature pattern modeling. *Climate Res.* (doi: 10.3354/cr01220)
*Matzarakis, A.* and *Mayer, H.*, 1996: Another kind of environmental stress: thermal stress. *WHO Newsletter 18*, 7–10.
*Matzarakis, A., Rutz, F.* and *Mayer, H.*, 2007: Modelling radiation fluxes in simple and complex environments—application of the RayMan model. *Int. J. Biometeorol. 51*, 323–334.
*Mayer, H.* and *Höppe, P.*, 1987: Thermal comfort of man in different urban environments. *Theor. Appl. Climatol. 38*, 43–49.
*Nakamura, Y.* and *Oke, T.R.*, 1988: Wind, temperature and stability conditions in an east-west oriented urban canyon. *Atmos. Environ. 22*, 2691–2700
*Oke, T.R.*, 1987: Boundary Layer Climates. (2nd ed.) Routledge, University Press, Cambridge.
*Petralli, M., Masetti, L., Brandani, G.*, and *Orlandini, S.*, 2013: Urban planning indicators: useful tools to measure the effect of urbanization and vegetation on summer air temperatures. *Int. J. Climatol. 34*, 1236–1244.
*Salamanca, F., Martilli, A., Tewari, M.*, and *Chen, F.*, 2011: A study of the urban boundary layer using different urban parameterizations and high-resolution urban canopy parameters with WRF. *J. Appl. Meteorol. Climatol. 50*, 1107–1128.
*Scharf, L.L.*, 1991: Statistical signal processing. Vol. 98. Reading, MA: Addison-Wesley.
*Spagnolo, J.* and *de Dear, R.*, 2003: A human thermal climatology of subtropical Sydney. *Int. J. Climatol. 23*, 1383–1395.
*Stewart, I.D.* and *Oke, T.R.*, 2012: Local Climate Zones for urban temperature studies. *Bull. Am. Meteorol. Soc. 93*, 1879–1900.
*Stewart, I.D., Oke, T.R.*, and *Krayenhoff, E.S.*, 2014: Evaluation of the 'local climate zone' scheme using temperature observations and model simulations. *Int. J. Climatol. 34*, 1062–1080.
*Unger, J., Sümeghy, Z., Gulyás, Á., Bottyán Z.* and *Mucsi, L.*, 2001: Land-use and meteorological aspects of the urban heat island. *Meteorol. Appl. 8*, 189–194.
URBAN-PATH Project, 2014: Evaluations and Public Display of Urban Patterns of Human Thermal Conditions. http://urban-path.hu/. Last accessed: April 20, 2014.
*Watkins, R., Palmer, J., Kolokotroni, M.* and *Littlefair, P.*, 2002: The London heat island: Results from summertime monitoring. *Build. Serv. Eng. Res. Technol. 23*, 97–106.

# IDŐJÁRÁS

*Quarterly Journal of the Hungarian Meteorological Service*
*Vol. 119, No. 3, July – September, 2015, pp. 355–378*


# Regional air quality models and the regulation of atmospheric emissions


**Bernard E.A. Fisher*[1], Charles Chemel [2], Ranjeet S. Sokhi [3], Xavier V. Francis [4], Keith J. Vincent [5], Anthony J. Dore [6], Stephen Griffiths [7], Paul Sutton [8], and Raymond D. Wright [9]**

[1] *Retired from Environment Agency, Reading, UK beafisher@cantab.net*
*Permanent address: Little Beeches, Headley Road, Leatherhead KT22 8PT, UK*

[2] *National Centre for Atmospheric Science, Centre for Atmospheric and Instrumentation Research, University of Hertfordshire, Hatfield, UK c.chemel@herts.ac.uk*

[3] *Centre for Atmospheric and Instrumentation Research, University of Hertfordshire, Hatfield, UK r.s.sokhi@herts.ac.uk*

[4] *Centre for Atmospheric and Instrumentation Research, University of Hertfordshire, Hatfield, UK X.Francis@herts.ac.uk*

[5] *Ricardo-AEA, Harwell, UK Keith.Vincent@ricardo-aea.co.uk*

[6] *Centre for Ecology and Hydrology, Penicuik, UK tony.dore@ceh.ac.uk*

[7] *E.ON Technologies, Ratcliffe-on-Soar, UK Stephen.Griffiths@eon.com*

[8] *RWE npower, Swindon, UK paul.sutton@rwenpower.com*

[9] *Spacefleet Ltd, UK rdw@spacefleet.co.uk*

**Corresponding author*



*(Manuscript received in final form October 13, 2014)*



**Abstract**—This paper investigates regional air quality model performance and the regulation of atmospheric emissions. Although evaluation of regional models cannot be reduced to a set of rules, the paper shows ways of developing better understanding of model performance. It draws on studies in recent years by the Environment Agency to quantify the uncertainty in predictions of regional air quality models. It is argued that a decision by a regulator on how to use a regional air quality model should be based on both operational evaluation (involving comparison with observation) and diagnostic

evaluation (for developing understanding of the model), using operational and diagnostic metrics. Operational and diagnostic evaluations were undertaken, using a 'constructor' (CMAQ) and a 'seer' type (TRACK-ADMS) regional air quality model, for the secondary pollutants $PM_{10}$, $PM_{2.5}$ and ozone, though for episodic ozone it was not possible to define an appropriate performance metric.

Neither type of model showed clearly better performance when applied to long-term average concentrations. There was not enough information to set a minimum margin of error in operational evaluations but margins of 20% or more are to be expected. Unlike operational metrics there is no obvious way of deriving diagnostic metrics. However a footprint diagnostic metric was shown to be a way to reveal the behaviour of $PM_{10}$ and $PM_{2.5}$ in both types of model. It is therefore suggested that seer models are used to reveal the structure of a model's underlying mathematical equations from which diagnostic metrics can be formed.

In the absence of an objective basis for setting acceptance criteria for models, it is proposed that the underlying pragmatic principle should be to use whatever has comparable accuracy with the best existing international practice. For regulatory applications, the error expected in current types of air quality models should be a consideration in any decision made on the basis of models.

*Key-words*: Inter-comparison, regional air quality, model, footprint, metric, diagnostic, operational, evaluation, seer, constructor

## *1. Introduction*

This paper addresses the question "When is a regional air quality model good enough to be the basis for making a decision about emission reductions to meet limit values?", accepting that the use of an environmental model may only be part of the decision making process. Model evaluation studies involve selecting appropriate metrics or diagnostics (parameters summarising key aspects of the behaviour of a model), and showing that the model can predict the metrics with appropriate accuracy compared with observations.

Regional model development has made considerable progress in recent decades and complex air quality models are essential for assessing secondary pollutants, such as wet deposition, ozone and particulate matter. However just because regional models are the only tools for assessing secondary pollutants, such as ozone and particulate matter, this does not ensure that they are adequate to make decisions about emission reductions.

The paper draws on studies in recent years by the Environment Agency to quantify the uncertainty in predictions of regional air quality models, the latest of which is the CREMO, Comparison of Regional Models, project. The results of the project are described in a number of reports (*Derwent*, 2013; *Fisher*, 2013; *Hayman et al.*, 2013a, 2013b, 2013c, and 2013d). These are used to draw conclusions about whether regional air quality models describing atmospheric concentrations over some 100's to a few 1000 kilometres, are an adequate basis for making decisions about emission reductions to meet environmental criteria.

## *2. General discussion of environmental models*

The way environmental models have been developed and used has been discussed in the literature (*Edwards*, 2010). One can refer to attempts to ensure that models are used properly (*Pilkey-Jarvis* and *Pilkey*, 2008). Air quality models include parameters which are assigned values for the problem in hand, to distinguish them from dependent variables, such as pollutant concentration or deposition. Parameters are usually mathematical functions of coefficients and dependent variables, representing a physical process.

It is rare for there to be sufficient observational data to be able to test exhaustively the behaviour of an environmental model. More often than not for policy applications, one is interested in the behaviour of an environmental system under conditions which have never occurred in nature and one is therefore investigating model scenarios which cannot be explicitly tested. In such situations the qualitative behaviour of the system described by the mathematical model is the only realistic goal. The environmental model can generally be approximated by a set of time dependent non-linear ordinary differential equations. In regional air quality models the synoptic meteorological conditions describe the motion of air masses crossing the main source regions. Under steady synoptic conditions regional pollutant concentrations may build up or decay. Assuming steady meteorological conditions persist for long enough, the solution of the set of mathematical equations tends in time towards a stationary point, though in nature the long time limits are not necessarily reached as meteorological conditions are never steady. However the behavior at stationary points under such idealistic conditions reveals something about the structure of the mathematical system, even if such conditions do not occur in reality. Of special interest are the specific parameter values at points where the qualitative behaviour changes, say from a tendency to decay from initial values to the growth in concentration (see later for a suspected example for ozone of a bifurcation). For this reason two broad categories of model can be distinguished: (1) those which reveal the underlying structure of the mathematical system, and (2) those which try to emulate the full complexity of the environmental system.

*Edwards* (2010) describes these two broad modelling approaches in relation to climate modelling: in type (1) *model seers*[1] use models to understand and explore the climate system with emphasis on its sensitivity to changing variables and processes. In type (2) *model constructors* seek to capture the full complexity of the climate system, which can then be used for various applications, promoted by the power of modern computing. Constructors seek to include more realism, including all known physical processes that influence the climate. Seers tend to focus on modelling the most fundamental and understood processes and to use a variety of models. The 'state of the art' for seers depends

[1] Definition. A *seer* is one who has insight. The common implication that a seer can predict the future is not relevant in the context of this paper.

on the model application. For constructors a single 'state of the art' model exists, which uses the most up to date observations as input and evaluation, and contains the most detailed and physically realistic parameterisations. This does not separate good from bad modelling practice but illustrates two different strategies for extending knowledge. Seers are generally interested in simple models, which promote understanding, while constructors ignore simple models and focus on complex comprehensive models. Regulators prefer a single model which can be regarded as 'fit for purpose' for making a policy decision, but one conclusion from this paper is not to rely on such a narrow approach to regional modelling.

### *3. Advances in air pollution assessment*

Regulators, such as the Environment Agency in the U.K., need to know whether a model can be used for decision making and this discussion has prompted model comparison exercises, starting with the comparison of dispersion models (*Hall et al.*, 2000a, 2000b) describing concentrations in the near-field out to 20 km from a source, and relatively simple acid deposition assessment models (*Abbott et al.*, 2003), where the model inter-comparison was used to gain understanding of model uncertainty. This paper focuses on the secondary pollutants, particulate matter (PM)[2], both $PM_{10}$ and $PM_{2.5}$ and ozone ($O_3$). The last decade or so has seen an enormous increase in the sophistication of computer programs, making calculations of secondary pollutants more accessible. The practical implementation of the US Environmental Protection Agency (USEPA) supported CMAQ (Community Multi-scale Air Quality) modelling system, which follows the constructor approach, has been notable. Documentation on CMAQ is available from the official CMAQ website (http://www.cmaq-model.org) [accessed 21 May 2013]. Regulators therefore need to be able to assess the capabilities of different types of air quality models with different levels of sophistication. This has promoted the constructors' approach. However, just because regional models are the only way of assessing secondary pollutants, this does not mean that they are good enough for regulation (*Pilkey-Jarvis* and *Pilkey*, 2008).

Secondary $PM_{2.5}$ is generated on a regional scale, so that the $PM_{2.5}$ concentration is a mixture of local and regional components. Regional models are the only way of assessing the impact of individual sources on the regional component of the $PM_{2.5}$ concentration and of estimating the population exposure. The contribution from local sources is not included within the regional component, because only concentration variations over regional scales, typically

[2] $PM_{10}$ particulate matter less than or equal to 10 microns (50% cut off);
$PM_{2.5}$ particulate matter less than or equal to 2.5 microns (50% cut off).

5 km or more, are treated in regional models such as CMAQ. A correction factor to take account of local sources needs to be included.

Regulators face a problem when applying complex, constructor models, such as CMAQ. In principle it is desirable that the results of a calculation can be replicated. However this becomes increasingly difficult as models become more complex. The detailed configuration may be difficult to set up on different computer platforms and decisions about which input data sets and options to apply become complicated to document.

Comparison of model predictions against observations is known as 'operational' evaluation. 'Diagnostic' assessment involves understanding the behaviour and response of a model system (*Dennis et al.*, 2010). Following the broad model categorisation described in Section 2, seers tend to consider 'diagnostic' evaluation, while constructors tend to focus mainly on the 'operational' evaluation of models. The operational performance of different types of regional models has been compared in the Model Evaluation Exercise for the UK Department for Environment, Food and Rural Affairs (Defra) (*Carslaw* 2011a, 2011b, and 2011c) and the Air Quality Modelling Evaluation International Initiative, AQMEII, (http://aqmeii.jrc.ec.europa.eu/ [accessed 21 May, 2013]). *Dore et al.* (2013) presented results of the Defra Model Evaluation Exercise which encompassed a wider set of models than comparisons described in this paper. Phase one of the AQMEII intercomparison (*Solazzo et al.*, 2012) involved 10 regional models. Four models were applied to both the European and North American domains; five models were applied to just the European domain and one model was applied to the North American domain. In the second phase of AQMEII (the Air Quality Model Evaluation International Inter-comparison) the earlier regional model inter-comparison assessment was extended to on-line air quality models in which the air quality and meteorological models were coupled together. The $PM_{10}$ and $PM_{2.5}$ concentrations simulated by eight on-line coupled models, run by seventeen independent groups from Europe and North America, were compared with each other and with observations (*Im et al.*, 2014).

In HTAP, the taskforce on the Hemispheric Transport of Air Pollutants, modelling inter-comparison, the predictions of the change in surface ozone as a result of continental scale changes in emissions were compared in 14 global chemical transport models. In this case *Wild et al.* (2012) did not use a seer model to understand the result, but rather used a simple scaling model to represent the source-receptor relationships found from the results in the full models. One global transport model was used to investigate the range of emission changes over which this simple, linearised model is accurate enough for practical, policy applications.

Generally the constructionist models used in the CREMO, AQMEII and HTAP inter-comparisons are too complex for it to be possible to diagnose which

factors have greatest influence on a model's performance. For particulate matter, model prediction was disappointing suggesting it is difficult to include all factors affecting concentrations.

Seer and constructor models have been used to evaluate policy decisions in the areas of air quality and acid deposition. Examples of a seer model in the UK include the semi-empirical TRACK-ADMS model, which is much simpler than CMAQ (*Abbott et al.* 2003; *Abbott et al.,* 2007) and was used to show that the average $PM_{10}$ concentration would have been 3 $\mu g\ m^{-3}$ higher in 2005 without the industrial policy intervention of the Environment Agency between 1990 and 2005 (*Vincent* and *Abbott,* 2008). Using the more complex, constructor model CMAQ, *Chemel et al.* (2014) estimated that the major industrial sources in the UK made up between 10 to 20% of the $PM_{2.5}$ concentration depending on location in 2006.

The type of a model used at the policy stage may not be the same as that used in the scientific stages of model evaluation. Instead it could involve model emulation.[3] As an example of the emulation methodology, a statistical emulation of the moderately complex constructor model, The Air Pollution Model (TAPM)[4] was used to estimate the consequences on human health, expressed as the number of life years lost, for one year's emission from a coal-fired power station (*Fisher et al.,* 2010). A range of emission conditions were evaluated without re-running TAPM for every set of conditions.

Simple, order of magnitude estimates, sometimes called 'back of envelope' calculations, can be considered to be a type of seer model. Provided they predict approximately similar responses to input changes as more complex, constructor models there is justification for using them in integrated assessments of air quality policy. This does not mean that the constructor models should be neglected by regulators and left to specialists. The constructor model provides the essential test bed for exploring understanding of the response of a model to changes in input over a wide range of conditions. Thus for regulators both the model *seer* and the model *constructor* approaches have important roles.

---

[3] For an explanation of an emulator, see http://mucm.aston.ac.uk/MUCM/MUCMToolkit/index.php?page=MetaOverviewEmulators.html [accessed 21 May, 2013]. If a computer simulation is computationally expensive, so that evaluating a constructor model for a choice of inputs takes a significant amount of computing time, one may be limited to evaluating the model at a small number of different input data sets. However one may want to know model predictions at a large number of different input values. One can deal with this problem by building an emulator: a statistical model of the model, constructed from a fairly small number of runs of the constructor model. The emulator will predict both output values, and report uncertainty in any prediction. In the Managing Uncertainty in Computer Models (MUCM) project, a toolkit for constructing Gaussian process emulators is described in which all parameter values and their interactions have uncertainty described by Gaussian functions. Gaussian functions possess convenient properties, making emulator formulation easy.

[4] The moderately complex meso-scale model, TAPM, was applied with UK emissions and meteorology in 2003 to illustrate the approach. The use of TAPM was an efficient way to generate a set of results distributed through parameter space. It would not have been practical at the time to have generated enough CMAQ results to build an emulator.

## *4. Model evaluation protocols and metrics*

In the CREMO project, different versions of the constructor model CMAQ were compared with three air quality models developed in the UK which may be regarded as seer models: the Fine Resolution Atmosphere Multi-Pollutant Exchange (FRAME) model for acid deposition (*Dore et al.* 2007), the Trajectory model with Atmospheric Chemical Kinetics–Atmospheric Dispersion Modelling System (TRACK-ADMS) model for annual audits (*Abbott et al.,* 2007) and the Ozone Source–Receptor Model (OSRM) for ozone (*Hayman et al.*, 2010). An Environment Agency report (*Hayman et al.*, 2013a) lists the sites, measurements and methods available in the UK for evaluating models against observations, as well as summarising the models. The aim was to establish whether the models met acceptance criteria as part of an evaluation protocol and not to establish which model had the best performance judged against observations.

Defra (*Derwent et al.*, 2010), and informally the USEPA (*Dennis et al.*, 2010), have published protocols for operational model evaluation using familiar statistical measures. Benchmarking procedures (*Thunis et al.*, 2011a) have also been produced. The optimal set-up (the set-up requiring the lowest computer resource and least preparation) for running constructor models efficiently over a year or more, to answer a policy question or a regulatory issue, cannot be specified precisely. The process involves setting up (1) emissions, (2) initial and boundary conditions, (3) running a meso-model to determine the meteorological fields, and then (4) running a chemical transport model, such as CMAQ. Although a model complies with an operational evaluation protocol, the model should not be used under emissions or meteorological conditions which have not occurred during the testing of the model.

The acceptance criteria set in the Ambient Air Quality Directive (*EC,* 2008) also set operational performance limits and are of great importance, because they impose compliance requirements on EU countries. The Directive allows models which satisfy the criteria to be used for air quality assessment to reduce the number of sampling sites, to prepare plans and abatement measures and to determine where the pollution is coming from. The guidance published by *FAIRMODE* (2011) and the guidance on $NO_2$ (*Denby,* 2011) interpret the Directive, elaborating on text in the Directive, such as 'relative directive error', but also describing its limitations.

In the Defra Model Evaluation Protocol (*Derwent et al.*, 2010) predictions of the model should be accepted if the percentage of model predictions within a factor of two (*FAC2*) of the observations is greater than 50 per cent. The normalised mean bias (*NMB*) is defined as:

$$NMB = \frac{\sum_{i=1}^{N} M_i - O_i}{\sum_{i=1}^{N} O_i}, \tag{1}$$

where $N$ is the number of observations, $M_i$ are the calculated values, $O_i$ are the observed values. The *NMB* should satisfy $-0.2 \leq NMB \leq 0.2$ in the Defra Model Evaluation Protocol. The *NMB* puts a higher weighting on model performance at higher concentrations, a distortion, but one which might be reasonable, given the greater concern over the occurrence of high concentrations. It would also be important to consider carefully the quality of the observations and the size of the sample $N$, the number of observed–calculated pairs.

A comparison of seer regional transport models (*Abbott et al.,* 2003) suggested that these simpler types of models could meet the *FAC2* criterion when calculating acid deposition. The set of possible statistical measures used to evaluate the constructor model CMAQ (*Chemel et al.,* 2010) included the percentage within a factor of two (*FAC2*) and the normalised mean bias (*NMB*). As part of the model intercomparison within CREMO (*Chemel et al.*, 2011), all the models considered (CMAQ v4.6, CMAQ v4.7, TRACK-ADMS and FRAME) were shown to satisfy the *FAC2* criterion, that 50 per cent of the modelled results should be within a factor of two of the annual mean concentrations for *all* the species considered. In contrast, none of the models satisfied the criterion that the normalised mean bias *NMB* should be in the range –20 to 20 per cent, for *all* the species considered, which included $PM_{10}$.

An *acceptance* criterion for ozone could refer to the annual average ozone concentration or to the peak ozone level during episodes. The annual average ozone depends largely on domain boundary conditions and removal within the domain, while episodic ozone concentrations rely on regional generation within the domain. It is therefore necessary to distinguish between an acceptance criterion for shorter periods, such as episodes, and an acceptance criterion for annual average ozone. There is no commonly accepted agreement over the best choice of metric in the operational evaluation of regional ozone models. There are examples of diagnostic ozone metrics in the review by *Middleton et al.* (2007), while *Rao et al.* (2011) argue in favour of the seasonal average as the most suitable operational metric.

## *5. Diagnostic evaluation*

### *5.1. Footprint metric*

A systematic procedure for setting a diagnostic evaluation protocol cannot be defined as this involves understanding model behaviour. A regulator is primarily interested in attributing concentrations to emissions. Thus diagnostic evaluation in the CREMO project was focused on the differences in the footprint of sources calculated by different regional models used for regulation. A 'footprint' metric is a response function, showing how concentrations or deposition are influenced spatially by emissions from a single specified source, such as a power station. Footprints are obtained from the difference between the concentration or

deposition, when all sources are included, and the concentration or deposition, when all sources, except for the specified source under consideration, are included. In the seer air quality models discussed in this paper, the individual footprints can be calculated directly. The footprint of secondary pollutants, such as particulate matter, depend directly on model parameters determining the formation by chemical reactions and removal by wet and dry deposition, which eventually lead to complete removal from the atmosphere after a number of days. In constructor models, such as CMAQ, the footprint determined after much computation appears to be distantly related to the original equations although the same removal processes influence behaviour. Consideration of the footprint metric can therefore link the performance of a seer type of regional model to the constructor type of model.

A footprint metric has two purposes: (a) it is a diagnostic of a seer or constructor model type, showing the change in concentration from the emission at a point source leading to understanding of the overall system behavior; and (b) for regulatory purposes, it shows how emission reductions may change concentrations.

A quantitative approach to evaluating footprints is to consider the distance dependent structure of the footprint of a single source (*Fisher et al.*, 2011). The weighted average concentration given by the average concentration along a typical trajectory, excluding dilution arising from horizontal dispersion, is obtained by multiplying the concentration by the distance from the source. This footprint metric is defined by:

$$\frac{r}{2\pi}\int_0^{2\pi} C(r,\theta)d\theta \tag{2}$$

where $C(r, \theta)$ is the concentration at a distance $r$ from the specified source in a direction $\theta$.

In CREMO the footprint profiles were normalised by the value of the near-field concentration, 30 km from the source, and this is illustrated in the profiles in the smaller figures in *Fig. 1*. The dependence of the $PM_{10}$ and $PM_{2.5}$ concentrations along a radial trajectory does not decrease rapidly with distance because of the gradual production of secondary aerosol in the atmosphere. A numerical diagnostic can be defined as the distance between the point source and the point at which the radial average secondary $PM_{10}$ or $PM_{2.5}$ concentration takes its maximum value. This diagnostic summarises the influence of the source on secondary aerosol formation.

The average dependence of the concentration with distance shown in *Fig. 1* (Eq. (2) without the distance $r$ in the numerator) does decay rapidly with distance, because the average concentration contains a factor proportional to the inverse of the distance from the source ($1/r$) arising from the spread of air mass trajectories.

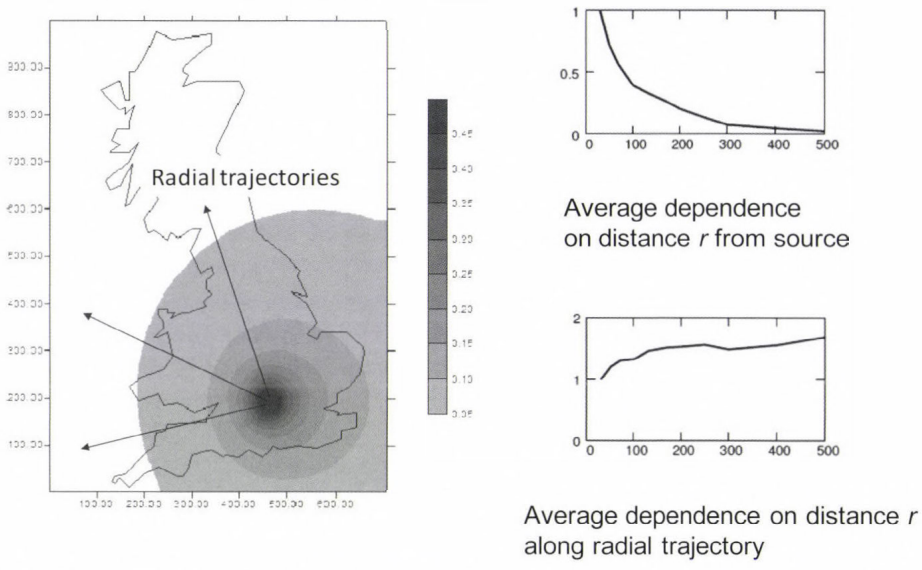


*Fig. 1.* Schematic illustration of the annual average $PM_{10}$ concentration footprint in $\mu gm^{-3}$ from a major stationary point source such as a power station. The main picture shows contours of the concentrations of $PM_{10}$ in $\mu gm^{-3}$, with distances along the axes in kilometres. The *top* small right hand figure shows the concentration along a typical, radial trajectory as a function of distance in kilometres, normalised by the value of the near-field concentration 30km from the source. The *bottom* small right hand figure shows the average weighted concentration along a radial trajectory, excluding dilution arising from horizontal dispersion by multiplying the concentration by the distance from the source (Eq. (2)).

When making policy decisions, a regulator should understand the underlying structure of the model used in the assessment, for which the first step is to understand how the model responds to emission changes. As the next step in diagnostic evaluation using footprints, a regulator needs to know whether footprints can be aggregated to assess a source control strategy. This means that if $\Delta q_i$ is the reduction in the source strength of the $i$th source under the control strategy, the reduction in concentration under the control strategy is approximately equal to $\Delta C$, where:

$$\Delta C = \sum_i \Delta q_i G_i \tag{3}$$

and $G_i$ is the footprint of the $i$th source of unit source strength. If Eq. (3) is a reasonable approximation, a reduction strategy can follow a sequential change in emissions, tracking in order which emission reductions are most effective.

### *5.2. Episode metric*

The occurrence of photochemical episodes, when high ozone concentrations are generated, suggests the need to be aware of a variety of possible behaviours. Under steady meteorological conditions, ozone would be expected to tend towards a limit, which is the long-term solution of a system of ordinary differential equations for a given choice of VOC emission strengths. Under some conditions, corresponding to lower VOC emission rates under strong winds and high atmospheric dilution, the ozone limit value would be expected to be close to the initial ozone concentration close to the background ozone concentration. This represents an approximate balance between the production and destruction of ozone over the domain. Under other conditions, corresponding to higher VOC emission rates under light winds and low dilution, the limit ozone value may be far from the initial state, corresponding to the build-up of ozone in an anticyclonic episode. The large difference in the limiting ozone concentration between these two emission and meteorological situations corresponds to a bifurcation in the steady-state behaviour of the differential equations describing the ozone system. This does not imply any discontinuity in ozone concentration, but differences in the limit values of the solution of the underlying differential equations. A large change in the limiting ozone concentration occurs for a small change in emissions near a bifurcation, so a sensitivity analysis would break down near the bifurcation point.

The occurrence of ozone episodes will to some extent influence the long-term average ozone concentration, although the occurrence of episodes may vary considerably from year to year depending on weather conditions. Ozone formation can be attributed to specific sources during an episode using constructor models. An ozone footprint during an episode has been calculated using the CMAQ model (*Yu et al.*, 2008) by investigating changes in ozone formation when the emissions from a specified source are altered. The 'integrated downwind ozone production' (IDOP) described by *Derwent* and *Nelson* (2003) is a footprint metric during an episode. IDOP describes how much ozone is produced in the downwind environment under ideal ozone producing conditions by each VOC species of a specified stationary source from selected runs of the Photochemical Trajectory Model (*Derwent et al.*, 2009), which one could class as a seer model. Using IDOP as a metric is a convenient, precautionary approach to regulation when screening VOC emissions. In cases when the IDOP approach suggests that an emission is not acceptable, more complex models of a seer type, such as OSRM, or of a

constructor type, such as CMAQ, need to be applied to test the conclusion. An alternative metric to IDOP is whether a 30% reduction in emissions of VOC or NOx suppresses the formation of an ozone episode.

### *5.3. Diagnostic evaluation of individual processes*

Another kind of diagnostic evaluation involves the behaviour of individual processes within a model, although it is not always possible to compare individual processes exactly when they are embedded within a complex model. When *Derwent* (2013) compared six chemical mechanisms (CRI, CB-05, CBM-4, SAPRC-99, SAPRC-07 and OSRM) within the Photochemical Trajectory Model (PTM), he found that the differences in the details of the chemical reaction scheme are not the most important factor in explaining differences between the predictions of ozone.

The Integrated Process Rate analysis of the CMAQ model undertaken by *Francis et al.* (2011) was used to understand the causes of an episode of high ozone over south-east England in 2003. The contributions of cloud processes, chemical processes, advection, diffusion, vertical advection, vertical diffusion, horizontal advection and dry deposition, at different model heights were considered. For this episode, in a south-east England domain, meteorological processes were shown to have the greatest influence.

## *6. Examples of operational evaluation*

In this section some examples of the operational evaluation of constructor and seer models are described. The seer model TRACK-ADMS was developed to enable the Environment Agency to assess contributions from major industrial sources (*Abbott* and *Vincent* 2007; *Abbott et al.*, 2003; *Vincent* and *Abbott,* 2008). TRACK-ADMS assumes simplified meteorology to calculate the long-term average atmospheric concentration. It contains some degree of data assimilation which improves predictions (by applying a bias correction). The model is suited to calculating the contributions from large industrial sources and has been subject to uncertainty analysis by undertaking a Monte Carlo analysis of the variation in output over plausible ranges of input parameters. Its limitation is that one cannot be sure that the choice of parameter input values used to evaluate the model, is appropriate in future emission scenarios when emissions and boundary conditions over the model domain may be very different from the ones used to test the model.

*Table 1* from *Chemel et al.* (2011) shows an example from the CREMO project of calculating $PM_{10}$ concentrations across the UK, comparing the performance of the CMAQ model, with a resolution set of 5 km, against the model TRACK-ADMS, with a resolution of 1 km. Observations from some 40 rural and background sites in the UK Automatic Urban and Rural Network

(AURN) are used in the evaluation, for which no correction for local sources is applied. Many more parameters need to be specified in the CMAQ model compared with TRACK-ADMS leading to more opportunities for errors to arise in the input data.

*Table 1.* Comparison of performance in predicting annual average $PM_{10}$ concentration at rural AURN sites in the UK in 2003, for which the local contribution should be minimal, for two versions of a constructor model, and a seer model

| **Model metric $PM_{10}$ for 2003** | **CMAQ v4.6** | **CMAQ v4.7** | **TRACK-ADMS** |
|---|---|---|---|
| *FAC2* (%) | 88.2 | 100.0 | 100.0 |
| *r* (correlation coefficient) | 0.09 | 0.0 | 0.45 |
| *NMB* | –0.33 | –0.09 | –0.20 |
| Single power station contribution (%) | 0.34 | 0.28 | 0.28 |

Based on the *NMB* metric, no systematic difference can be seen between the performance of the two versions of the CMAQ model, of the constructor type, and that of the simpler, seer model TRACK-ADMS. A negative *NMB* bias implies a model under-prediction and so a margin of error should be included in model predictions. Results in *Table 1* suggest that the margin of error for $PM_{10}$ is about 20%.

There is not sufficient observational data in 2006 in the UK on which to test the performance of regional model predictions of $PM_{2.5}$. However the CMAQ model has also been used to simulate air quality over North America and Europe for the year 2006 (*Appel et al.,* 2012) as part of the AQMEII project (*Galmarini* and *Rao,* 2011). *Table 2* shows the seasonal, domain averaged, normalised mean biases (*NMB*) of daily average $PM_{2.5}$ concentrations from the CMAQ model for the North American Air Quality System network and the European AirBase network in the year 2006. As far as possible, the CMAQ model configurations were similar for North America and Europe, with both simulations utilising version 4.7.1 of CMAQ. The North American simulation used 34 vertical layers and a 12 km horizontal grid spacing, while the European simulation used 34 vertical layers and an 18 km horizontal grid spacing covering most of Europe. The overestimate of $PM_{2.5}$ at North American sites is thought to arise from an overestimate in the unspeciated $PM_{2.5}$ mass (*Appel et al.,* 2012), which makes up a significant proportion of the $PM_{2.5}$ mass in version 4.7.1 of the CMAQ model. Improvements to the way this component is treated are incorporated in later versions of CMAQ. If one considers all the models for

which predictions were available in AQMEII, then generally there appears to be significant under-prediction of both $PM_{10}$ and $PM_{2.5}$ (*Schere et al.,* 2012).

*Table 3* shows the seasonal, domain-wide normalised mean biases of daily average $PM_{10}$ concentrations for the North American Air Quality System and European AirBase networks from the CMAQ model. The model performance for $PM_{2.5}$ and $PM_{10}$, especially for the European domain, shows large under-prediction and occurs in other constructor models where the finest grid resolution is some kilometres or more, not just in CMAQ (*Solazzo et al.,* 2012).

*Table 2. NMB* of daily average $PM_{2.5}$ comparisons between predictions and observations in different seasons of 2006 over North America and Europe made under AQMEII (*Appel et al.* 2012) using the CMAQ model

| Season and domain | Approximate number of sites | *NMB* |
|---|---|---|
| Winter, North America | 958 | 0.304 |
| Winter, Europe | 160 | –0.550 |
| Spring, North America | 958 | 0.189 |
| Spring, Europe | 160 | –0.369 |
| Summer, North America | 958 | –0.046 |
| Summer, Europe | 160 | –0.372 |
| Autumn, North America | 958 | 0.363 |
| Autumn, Europe | 160 | –0.242 |

*Table 3. NMB* of daily average $PM_{10}$ comparisons between predictions and observations for different seasons in 2006 over North America and Europe made under AQMEII (*Appel et al.* 2012) using the CMAQ model

| Season and domain | Approximate number of sites | *NMB* |
|---|---|---|
| Winter, North America | 956 | –0.479 |
| Winter, Europe | 1000 | –0.648 |
| Spring, North America | 956 | –0.565 |
| Spring, Europe | 1000 | –0.562 |
| Summer, North America | 956 | –0.574 |
| Summer, Europe | 1000 | –0.612 |
| Autumn, North America | 956 | –0.465 |
| Autumn, Europe | 1000 | –0.468 |

The general tendency for constructor models with realistic chemistry and transport to under-predict particulate concentrations can be readily interpreted as either (1) due to the omission of local combustion source contributions in models with grid resolution of 5 km or more, or (2) due to the neglect or to the inaccurate estimate of the emissions of non-combustion, windblown or re-suspended dust (especially for the coarse fraction of particulate, the difference between $PM_{10}$ and $PM_{2.5}$) or (3) inaccuracies in the instrumentation or the site description (rural, background *etc.*) in the observational network.

In constructor models, such as CMAQ, short-term average concentrations, such as daily concentrations, can be calculated. In *Table 4* from *Chemel et al.* (2010), the performance of CMAQ v4.6 is shown for the daily variation of the two main secondary species of interest, ozone and $PM_{10}$[5]. The model performance for daytime ozone concentrations over a year is seen to be superior to that of $PM_{10}$.

*Table 4.* Comparison of performance in predicting the daily maximum ozone and daily mean $PM_{10}$ concentrations at AURN sites in the UK in 2003 for CMAQ v4.6

| **CMAQ v4.6 metric** | **Maximum daily running eight-hour mean ozone** | **Daily mean $PM_{10}$** |
|---|---|---|
| *NMB* | 0.05 | –0.34 |
| *r* (correlation coefficient) | 0.69 | 0.47 |
| *FAC2* (%) | 76.7 | 26.8 |
| Number of sites | ~40 | ~40 |

The CMAQ ozone *NMB* in *Table 4* for the UK in 2003 is within ±0.1. The ozone predictions in 2003 from the OSRM Lagrangian trajectory model for the UK in 2003, described by *Hayman et al.* (2010), also satisfy this performance measure. The AQMEII project provided CMAQ performance statistics for ozone for the many hundreds of ozone monitoring sites in Europe and North America. The *NMB* for daytime ozone over a year is generally within ±0.1, apart from during the summer season in Europe. Given the similar level of model performance from diverse models, a *NMB* of within ±0.1 appears to be achievable for the daytime ozone concentrations over a year with the current generation of photochemical models.

[5] The paper by Chemel *et al.* (2010) contains many more performance statistics than those summarised in *Table 4*. The daily $PM_{10}$ *NMB* is equivalent to the annual average $PM_{10}$ *NMB* in *Table 1* apart from rounding errors.

Using the seer OSRM and constructor CMAQ models, the impact of an oil refinery in southern England, with VOC emissions ~0.2 kg/s and NOx emissions ~0.2 kg/s, on annual average ozone concentrations in 2003 was assessed in CREMO. The predicted change in the annual average ozone concentration along a horizontal transect through the refinery (*Hayman et al.*, 2013d) shows that the emissions from the refinery led to a decrease in ozone on average in both models (of magnitude $<0.2$ μg $m^{-3}$) out to distances of a few hundred kilometres. The decrease is thought to be caused by the reaction of ozone with NO releases. The similarity in the operational performance of the OSRM and CMAQ models gives confidence in the simpler, seer OSRM model, which was designed to develop national policy for regulating ozone. However a full understanding of the performance of regional models over the complete range of conditions of interest cannot be based purely on operational performance metrics. Diagnostic evaluation is also required.

## *7. Examples of diagnostic evaluation*

The modelling of the $PM_{2.5}$ and $PM_{10}$ footprint from a power station ought be better than the regional predictions discussed in the previous section, because (1) there is no locally derived coarse particulate, (2) the primary source strength, which consists largely of inorganic compounds, is better known and (3) the plume chemistry without secondary organics is simpler. Examples from CREMO of the footprint of particulate matter from a power station source, are given in *Figs. 2* and *3* using the distance weighted footprint introduced schematically in Figure 1. The average concentration along a radial trajectory is normalised by the concentration in the near field, 30 km from the source.

Footprints used in diagnostic evaluations cannot be compared directly with observations. However they are useful for diagnosing how models are treating processes within the model. In *Fig. 2* the distance-dependent weightings of the annual average $PM_{10}$ concentration in a power station footprint are compared for three types of models. Broadly the models show little dependence on distance suggesting that the removal by wet and dry deposition is largely in balance with production by chemical transformation. The detailed behaviour is different, presumably because of differences in details of the models' structure, parameters and the input data sets, even for the two models whose structure is similar (CMAQ v4.6 and CMAQ v4.7). *Sutton et al.* (2013) showed that apparently small differences in the temporal profile of ammonia emissions over the year in 2003 (although the spatial distribution of the annual total ammonia emission was identical) can make differences to the prediction of the annual spatial distribution of components of $PM_{2.5}$ and of acid deposition. This suggests that differences in the set-up of model runs can make differences to the spatial distribution, even if the

models themselves (CMAQ v4.6 and CMAQ v4.7) are formulated in a similar way and demonstrate similar behaviour.

The distance-dependent weighting of the sulphur deposition from a power station shows a general decrease out to distance of 500km, while the distance-dependent weighting of the nitrogen deposition shows an increase out to the same distance[6].

In *Fig. 3*, the distance-dependent weightings of $PM_{2.5}$ and $NO_2$ for different kinds of sources investigated in CREMO are shown. Different distance dependencies are demonstrated. Small-scale variations in the plots may be the result of edge effects in the domains from which the footprints are plotted.

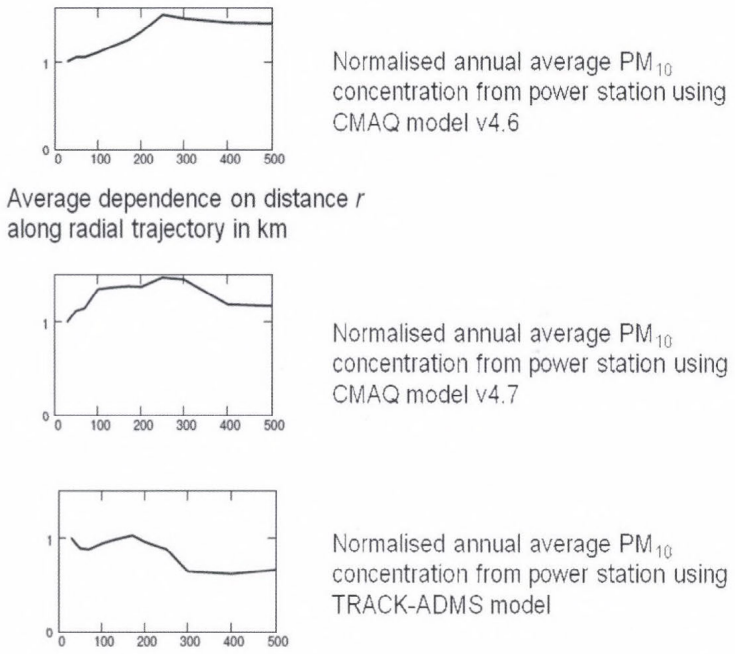


*Fig. 2.* Dependence of the $PM_{10}$ concentration on distance in kilometres along a radial trajectory, derived from the footprint of a power station source in central southern England, using Eq. (2), normalised by the value of the concentration near the source at 30km, for two versions of the constructor model CMAQ (v4.6 and v4.7), *top two figures*, and for the seer model TRACK-ADMS, *bottom figure*.

[6] The deposition footprints are not shown in this paper.

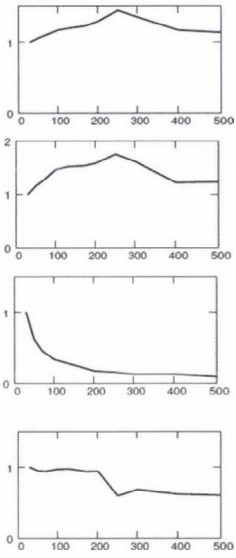


*Fig. 3. Top two figures*: Normalised dependence of the $PM_{2.5}$ concentration on distance in kilometres along a radial trajectory, derived from the footprint of a power station source, using Eq. (2), for two versions of the constructor model CMAQ (v4.6 and v4.7). *Bottom two figures*: Normalised dependence of the $NO_2$ concentration on distance in kilometres for Heathrow Airport and normalised dependence of the $PM_{2.5}$ concentration on distance in kilometres for an oil refinery in southern England from results of the constructor model CMAQ v4.6. Different distance dependencies are demonstrated in the footprints.

The EMEP model (NMI, 2010) is a constructor model and has been used to derive the contribution from individual countries to the regional concentration of $PM_{2.5}$ over Europe using grid cells of dimension 50 km×50 km. A diagnostic metric is the set of individual country footprints for a 15 per cent change in emissions, equivalent to the annual country-to-grid source–receptor matrices, see http://www.emep.int/SR_data/index_sr.html [accessed 21 May 2013]. *Fig. 4* shows the circumferentially averaged footprint of the UK centred on the middle of a grid cell in central England. The footprint is plotted at distances greater than 150 km from the centre of the country, because the national footprint of $PM_{2.5}$ concentration is distorted by the irregular distribution of sources over the country. The EMEP footprint for the UK is compared with the footprint from the typical power station analysed in CREMO. It is seen that, out to distances of 500 km, the balance between production and loss is approximately maintained in both the footprint calculations. As expected, atmospheric loss mechanisms from wet and dry deposition begin to dominate beyond this distance. The footprints are expressed in concentration units. The maximum $PM_{2.5}$ concentrations in the two cases are about 0.8 and 0.2 $\mu gm^{-3}$, respectively.

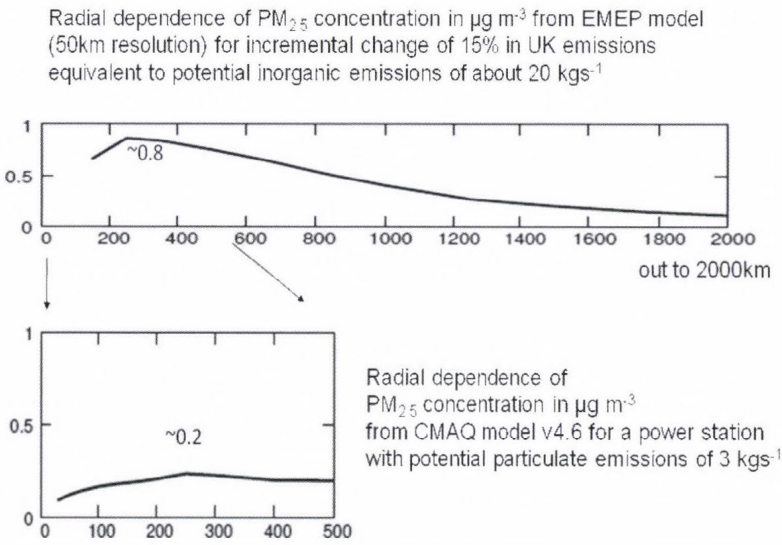


*Fig. 4. Top:* Dependence of the $PM_{2.5}$ concentration in $\mu gm^{-3}$ on distance in kilometres, in 2003, along a radial trajectory starting in central England, based on a 15% reduction in UK emissions, based on the EMEP model (Klein *et al.* 2011). *Bottom:* Dependence of $PM_{2.5}$ concentration in $\mu gm^{-3}$ on distance in 2003, along a radial trajectory, from the footprint of a power station source. Notional potential source strengths for the two types of sources (in $kgs^{-1}$) and the maximum values of the $PM_{2.5}$ concentrations in the two calculations (0.8 and 0.2 $\mu gm^{-3}$) are shown.

Although the species profiles ($SO_2$ : NOx: $NH_3$) of the UK emissions and a single coal-fired power station source are different, an approximate estimate can be made of the dominant precursor emissions, using the sum of primary, precursor species ($SO_2$ + NOx + NH3 + primary $PM_{2.5}$). Although only rough estimates, there is consistency in magnitude in the two cases. The 15% incremental change in UK emissions is six times the power station source strength and gives roughly four times the maximum $PM_{2.5}$ concentration of the power station. The distance-dependent weighting is different in detail. This may be a result of the different spatial resolution of the two models or the result of detailed differences in the treatment of particle formation in the two models.

The footprint is seen to be a valuable metric for diagnosing the behaviour of both constructor and seer air quality models. There is no objective way of deriving diagnostic metrics, though the structure of seer models are likely to indicate aspects of both types of models from which diagnostic metrics can be formulated.

## *8. Conclusions*

The evaluation of models is thus not a wholly objective procedure i.e. it cannot be reduced to a set of rules. However it can be made more systematic by the use of checklists (*Risbey et al.*, 2001) and by systematically evaluating the performance of air quality models, as described by *Thunis et al.* (2011a,b) and *FAIRMODE* (2011) and illustrated by *Chemel et al.* (2010) and *Pederzoli et al.* (2011). Moreover if consistency is shown between the predictions of models which have been developed for performance (the model constructors' approach) and models used to develop understanding (the model seers' approach), then this gives greater confidence in the decisions made.

The operational and diagnostic evaluation of regional air quality models of the seer and constructor type for regulating secondary atmospheric pollutants, such ozone, $PM_{10}$ and $PM_{2.5}$ have been illustrated. There was no clear separation between the operational performance of a seer and a constructor regional air quality model, using observational data sets and the commonly applied operational metrics *FAC*2 and *NMB*. A margin of error shown by operational evaluations of a model should be added to the predictions when the model is used to show compliance with a limit value. However it is not possible from the results of operational evaluations shown in this paper to set a minimum margin of error though this could be at least 20% for annual average concentrations of $PM_{10}$ and $PM_{2.5}$. For long-term average ozone the margin of error appears to be smaller, but interest is really in episodic ozone for which no generally accepted metric has been agreed.

Diagnostic evaluation is needed to justify the use of regional air quality models under conditions where no observational data is available. Although widely applied metrics based on statistical variables are used in operational evaluation, no commonly agreed, standard set of diagnostics exists, which can be used to understand the performance of constructionist regional models. However it is hoped that the continued use of seer models will generate metrics for diagnostic evaluation on a case by case basis.

The footprint metric is shown to be a useful diagnostic for both user and constructor models. The footprint shows similar behaviour in the regional seer and constructor air quality models analysed. It illustrates clearly the balance between the production and loss of $PM_{10}$ and $PM_{2.5}$ from a specified point source, such as a power station, out to distances of 500km beyond which removal processes dominate. For ozone the system behaviour is fundamentally different in episodic and non-episodic conditions. Unlike operational metrics there is no obvious way of deriving diagnostic metrics. However seer models are likely to reveal directly the structure of a model's underlying mathematical equations from which diagnostic metrics can be formed.

***Acknowledgements:*** The principal author acknowledges valuable discussions held with colleagues within the context of the CREMO project when he was working at the Environment Agency and under the letter of agreement between Defra, the Environment Agency and the US Environmental Protection Agency establishing cooperation on exposure science. The CREMO project was supported by the Environment Agency of England under contract (20073/R&D SC060037). The partners included the University of Hertfordshire, AEA Technology, the Joint Environment Programme of the power industry, CEH Edinburgh, RD Scientific and Hayman Atmospheric Consulting. Some of these organisations made significant contributions in kind to the work programme. Results of this work may not necessarily reflect the views of the Environment Agency or any individual CREMO participant and no official endorsement should be inferred.

## *References*

*Abbott, J., Hayman, G., Vincent, K., Metcalfe, S., Dore, T., Skeffington, R., Whitehead, P., Whyatt, D., Passant, N.* and *Woodfield, M.*, 2003: Uncertainty in acid deposition modelling and critical loads. *Environment Agency Technical Report P4-083(5)/1.* Bristol: Environment Agency.

*Abbott, J.A., Vincent, K.J.* and *Stedman, J.R.*, 2007: Methods for auditing the contribution of Environment Agency regulated processes to pollution. *Environment Agency Science Report SC030172/SR2.* Bristol: Environment Agency. https://publications.environment-agency.gov.uk/skeleton/publications/ViewPublication.aspx?id=b839fd39-b1db-4fdd-9d8a-40e3ee476c19 [accessed May 21, 2013].

*Abbott, J.* and *Vincent, K.*, 2007: Auditing the contribution of Environment Agency regulated processes to pollution. *Environment Agency Science Report SC030172/SR3.* Bristol: Environment Agency.https://publications.environment-agency.gov.uk/skeleton/publications/ViewPublication.aspx?id=65c9d2a8-87f9-4a2e-b67e-a69c5b244905 [accessed May 21, 2013].

*Appel, W., Chemel, C., Roselle, S.J., Francis, X.V., Hu, R.-M., Sokhi, R.S., Rao, S.T.* and *Galmarini, S.*, 2012: Examination of the Community Multiscale Air Quality (CMAQ) model performance over the North American and European domains. *Atmos. Environ. 53*,142–155.

*Carslaw, D.*, 2011a: Defra urban model evaluation analysis – Phase 1. London: Defra. Available from: http://uk-air.defra.gov.uk/library/reports?report_id=654 [accessed May 21, 2013].

*Carslaw, D.*, 2011b: Defra regional and transboundary model evaluation analysis – Phase 1. London: Defra. Available from: http://uk-air.defra.gov.uk/library/reports?report_id=653 [accessed May 21, 2013].

*Carslaw, D.*, 2011c: Defra deposition model evaluation analysis – Phase 1. London: Defra. Available from: http://uk-air.defra.gov.uk/library/reports?report_id=652 [accessed May 21, 2013].

*Chemel, C., Sokhi, R.S., Yu, Y., Hayman, G.D., Vincent, K.J., Dore, A.J., Tang, Y.S., Prain, H.D.* and *Fisher, B.E.A.*, 2010: Evaluation of a CMAQ simulation at high resolution over the UK for the calendar year 2003. *Atmos. Environ. 44*, 2927–2939.

*Chemel, C., Sokhi, R.S., Dore, A.J., Sutton, P., Vincent, K.J., Griffiths, S.J., Hayman, G.D., Wright, R., Baggaley, M., Hallsworth, S., Prain, H.D.* and *Fisher, B.E.A.*, 2011: Predictions of UK regulated power station contributions to regional air pollution and deposition: a model comparison exercise. *J. Air Waste Manage. Ass. 61*, 1236–1245.

*Chemel, C., Fisher B.E.A., Kong X., Francis X.V., Sokhi R.S., Good N., Collins W.J.* and *Folberth G.A.*, 2014: Application of chemical transport model CMAQ to policy decisions regarding $PM_{2.5}$ in the UK. *Atmos. Environ. 82*, 410-417.

*Denby, B.*, 2011: Guide on modelling nitrogen dioxide ($NO_2$) for air quality assessment and planning relevant to the European Air Quality Directive. Result of activities in the Forum for Air Quality Modelling in Europe. *FAIRMODE Working Group 1, Version 4.6. ETC/ACM Technical Paper 2011/15.* Bilthoven, The Netherlands, European Topic Centre on Air Pollution and Climate Change Mitigation, RIVM.

*Dennis, R., Fox, T., Fuentes, M., Gilliland, A., Hanna, S., Hogrefe, C., Irwin, J., Rao, S.T., Scheffe, R., Schere, K., Steyn, D.* and *Venkatram, A.*, 2010: A framework for evaluating regional-scale numerical photochemical modeling systems. *Environ. Fluid Mech. 10*, 471–489.

*Derwent, R.* and *Nelson, N.*, 2003: Development of a reactivity index for the control of the emissions of organic compounds. *R&D Technical Report P4-105 RC8309*. Bristol: Environment Agency.

*Derwent, R., Witham, C., Redington, A., Jenkin, M., Stedman, J., Yardley, R.* and *Hayman, G.*, 2009: Particulate matter at a rural location in southern England during 2006: Model sensitivities to precursor emissions. *Atmos. Environ. 43*, 689–696.

*Derwent, D., Fraser, A., Abbott, J., Jenkin, M., Willis, P.* and *Murrells, T.*, 2010: Evaluating the performance of air quality models. *Report prepared for the UK Department for Environment, Food and Rural Affairs*, Issue 3/June 2010. London: Defra. Available from:http://uk-air.defra.gov.uk/reports/cat05/1006241607_100608_MIP_Final_Version.pdf [accessed May 21, 2013].

*Derwent, R.D.*, 2013: Chemical mechanism choice: impacts of ozone precursor emissions reductions in the United Kingdom on episodic peak ozone in the United Kingdom. *Environment Agency Report SC060037e/R*. Bristol: Environment Agency. https://publications.environment-agency.gov.uk/skeleton/publications/ViewPublication.aspx?id=cf825d8d-f061-44cb-9293-51b96939d244 [Accessed May 20, 2013].

*Dore A.J., Vieno, M., Tang, Y.S., Dragosits, U., Dosio, A., Weston, K.J.* and *Sutton, M.A.*, 2007: Modelling the atmospheric transport and deposition of sulphur and nitrogen over the United Kingdom and assessment of the influence of $SO_2$ emissions from international shipping. *Atmos. Environ. 41*, 2355–2367.

*Dore, A.J., Carslaw, D., Chemel, C., Derwent, R.G., Fisher, B.E.A., Griffiths, S.J., Lawrence, S., Metcalfe, S.E., Redington, A., Simpson, D., Sokhi, R., Sutton, P., Vieno, M.* and *Whyatt, J.D.*, 2013: Evaluation and inter-comparison of acid deposition models for the UK. *Air Pollution Modeling and its Application XXII* (ed. D G. Steyn, P.J.H. Builtjes and R.M.A. Timmermans), pp 505-10. Dordrecht: Springer.

*EC*, 2008: Directive 2008/50/EC of the European Parliament and of the Council of 21 May 2008 on Ambient air quality and cleaner air for Europe. *Official Journal of the European Union, L152*, 11 June 2008, 1–44.

*Edwards, P.N.*, 2010: A vast machine Computer models, climate data and the politics of global warming, The MIT Press, Cambridge Massachusetts, London, England.

*FAIRMODE (Forum for Air Quality Modelling in Europe)*, 2011: The application of models under the European Union's Air Quality Directive: A technical reference guide. *Technical Report No 10/2011*. Copenhagen: European Environment Agency. Available from: http://www.eea.europa.eu/publications/fairmode [accessed May 21, 2013].

*Fisher, B.E.A.*, 2013: Comparison of simple and advanced regional models (CREMO): Outcomes for the Environment Agency. *Environment Agency Report SC060037/R*. Bristol: Environment Agency.https://publications.environment-agency.gov.uk/skeleton/publications/ViewPublication.aspx?id=cf825d8d-f061-44cb-9293-51b96939d244 [Accessed May 20, 2013].

*Fisher, B., Chemel, C., Hu, R.-M.* and *Sokhi, R.*, 2010: Emulating complex calculations for regulatory decisions. *Air Pollution Modeling and its Application XX*, (ed. D.G. Steyn and S.T. Rao), pp. 195–199. Dordrecht: Springer.

*Fisher, B. E. A., Chemel, C., Francis, X.V., Hu, R.-M., Sokhi, R.S., Hayman, G.D., Vincent, K.J., Dore, A.J., Griffiths, S., Sutton, P.* and *Wright, R.D.*, 2011: Diagnostic evaluation of complex and simple atmospheric chemical transport models by considering single source impacts in the UK. *Air Pollution Modeling and its Application XXI*, (ed.D.G. Steyn and S. Trini Castelli), pp 427–431. Dordrecht: Springer.

*Francis, X., Chemel, C., Sokhi ,R.S., Norton, E.G., Ricketts, H.* and *Fisher, B.*, 2011: Mechanisms responsible for the build-up of ozone over South East England during the August 2003 heat wave. *Atmos. Environ. 45*, 6880–6890.

*Galmarini S.* and *Rao S.T.*, 2011: The AQMEII two-continent Regional Air Quality Model evaluation study: Fueling ideas with unprecedented data. *Atmos. Environ. 45*, 2464.

*Hall, D.J., Spanton, A.M., Dunkerley, F., Bennett, M.* and *Griffiths, R.F.*, 2000a: A review of dispersion model inter-comparison studies using ISC, R91, AERMOD and ADMS. *Environment Agency Technical Report P353*, Environment Agency, Bristol.

*Hall, D.J., Spanton, A.M., Dunkerley, F., Bennett, M.* and *Griffiths, R.F.*, 2000b: An inter-comparison of the AERMOD and ADMS and ISC dispersion models for regulatory applications. *Environment Agency Technical Report P362*, Environment Agency, Bristol.

*Hayman, G.D., Abbott, J., Davies, T., Thomson, C.L., Jenkin, M.E., Thetford, R.* and *Fitzgerald, P.*, 2010: The Ozone Source–Receptor Model: a UK ozone policy tool. *Atmos. Environ. 44*, 4283–4297.

*Hayman, G., Sokhi, R., Chemel, C., Griffiths, S., Vincent, K., Dore, A.J., Sutton, P.* and *Wright, R.*, 2013a: Comparison of simple and advanced regional models (CREMO): Model evaluation protocol. *Environment Agency Report SC060037a/R.* Bristol: Environment Agency. https://publications.environment-agency.gov.uk/skeleton/publications/ViewPublication.aspx?id=cf825d8d-f061-44cb-9293-51b96939d244 [Accessed May 20, 2013].

*Hayman, G., Sokhi, R., Chemel, C., Griffiths, S., Vincent, K., Dore, A.J., Sutton, P.* and *Wright, D.R.*, 2013b: Comparison of simple and advanced regional models (CREMO): Model evaluation report. *Environment Agency Report SC060037b/R.* Bristol: Environment Agency.https://publications.environment-agency.gov.uk/skeleton/publications/ViewPublication.aspx?id=cf825d8d-f061-44cb-9293-51b96939d244 [Accessed May 20, 2013].

*Hayman, G., Sokhi, R., Chemel, C., Griffiths, S., Vincent, K., Dore, A.J., Sutton, P.* and *Wright, R.*, 2013c: Comparison of simple and advanced regional models (CREMO): Ozone diagnostics. *Environment Agency Report SC060037c/R.* Bristol: Environment Agency.https://publications.environment-agency.gov.uk/skeleton/publications/ViewPublication.aspx?id=cf825d8d-f061-44cb-9293-51b96939d244 [Accessed May 20, 2013].

*Hayman, G., Sokhi, R., Chemel, C., Griffiths, S., Vincent, K., Dore, A.J., Sutton, P.* and *Wright, R.*, 2013d. Comparison of simple and advanced regional models (CREMO): Model evaluation: Ground-level ozone. *Environment Agency Report SC060037d/R.* Bristol: Environment Agency. https://publications.environment-agency.gov.uk/skeleton/publications/ViewPublication.aspx?id=cf825d8d-f061-44cb-9293-51b96939d244 [Accessed 20 May 2013].

*Im, U., Bianconi, R., Solazzo, E., Kioutsioukis, I., Badia, A., Balzarini, A., Baró, R., Bellasio, R., Brunner, D., Chemel, C., Curci, G., van der Gon, H.D., Flemming, J., Forkel, R., Giordano, L., Jiménez-Guerrero, P., Hirtl, M., Hodzic, A., Honzak, L., Jorba, O., Knote, C., Makar, P.A., Manders-Groot, A., Neal, L., Pérez, J.L., Pirovano, G., Pouliot, G., San Jose, R., Savage, N., Schroder, W., Sokhi, R.S., Syrakov, D., Torian, A., Tuccella, P., Wang, K., Werhahn, J., Wolke, R., Zabkar, R., Zhang, Y., Zhang, J., Hogrefe, C.* and *Galmarini, S.*, 2014. Evaluation of operational online-coupled regional air quality models over Europe and North America in the context of AQMEII phase 2. Part II: Particulate matter., *Atmos. Environ.* http://dx.doi.org/10.1016/j.atmosenv.2014.08.072

*Klein, H., Gauss M., Nyiri A.* and *Steensen B.M.*, 2011: Transboundary air pollution by main pollutants (S, N, $O_3$) and PM: The United Kingdom. *MSC-W Data Note 1/2011.* Oslo: Norwegian Meteorological Institute.

*Middleton, D.R., Luhana L.* and *Sokhi R.S.*, 2007: Overview of indicators for estimating the contribution of Environment Agency regulated sources to regional ozone. *Environment Agency Report SC030171/SR3.* Bristol: Environment Agency.

*NMI*, 2010: Transboundary acidification, eutrophication and ground-level ozone in Europe for 2008. *EMEP Status Report 2010.* Oslo: Norwegian Meteorological Institute. Available from: http://emep.int/publ/reports/2010/status_report_1_2010.pdf [accessed May 21, 2013].

*Pederzoli, A., Thunis, P., Georgieva, E., Borge, R.* and *Carruthers, D.*, 2011: Performance criteria for the benchmarking of air quality model regulatory applications: the 'target' approach.*14th Conference on Harmonisation within Atmospheric Dispersion Modelling for Regulatory Purposes*, 2–6 October 2011, Kos, Greece.

*Pilkey-Jarvis, L.* and *Pilkey, O.H.*, 2008: Useless arithmetic: ten points to ponder when using mathematical models in environmental decision making. *Public Administration Review 68*, 470–479.

*Rao, S.T., Porter, P.S., Mobley, J.D.* and *Hurley, F.*, 2011: Understanding the spatio-temporal variability in air pollution concentrations, *EM*, the Air and Waste Management Association Magazine for Environmental Managers, November 2011, 42–48.

*Risbey, J., Van Der Sluijs, J.P., Ravetz, J.* and *Jannsen, P.*, 2001: A check list for quality assurance in environmental modelling. *Report Number NW&S-E-2001-11.* Utrecht: Department of Science, Technology and Society, Utrecht University. Available from: http://www.nusap.net/downloads/reports/E2001-11.pdf.

*Schere, K., Vautard, R., Solazzo, E., Hogrefe, C.* and *Galmarini, S.*, 2012: Results and lessons learned from Phase 1 of the AQMEII. *EM*, the Air and Waste Management Association Magazine for Environmental Managers, July 2012, 30–37.

*Solazzo, E., Bianconi, R., Pirovano, G., Matthias, V., Vautard, R., Moran, M.D., Appel, K.W., Bessagnet, B., Brandt, J., Christensen, J.H., Chemel, C., Coll, I., Ferreira, J., Forkel, R., Francis, X.V., Grell, G., Grossi, P., Hansen, A.B., Miranda, A.I., Nopmongcol, U., Prank, M., Sartelet, K.N., Schaap, M., Silver, J.D., Sokhi, R.S., Vira, J., Werhahn, J., Wolkem, R., Yarwood, G., Zhang, J., Rao, S.T.* and *Galmarini, S.*, 2012: Operational model evaluation for particulate matter in Europe and North America in the context of AQMEII. *Atmos. Environ. 53*, 75–92.

*Sutton, P., Chemel, C., Griffiths, S.* and *Sokhi, R.S.*, 2013: Investigation, using CMAQ, of sensitivity of air quality modelling to input ammonia emissions. *Air Pollution Modeling and its Application XXII* (ed. D G. Steyn, P.J.H. Builtjes and R.M.A. Timmermans), pp 571-6. Dordrecht: Springer.*Thunis, P., Georgieva, E.* and *Galmarini, S.*, 2011a: A procedure for air quality models benchmarking. Version 2. Ispra, Italy: European Commission, Joint Research Centre. Available from: http://fairmode.ew.eea.europa.eu/models-benchmarking-sg4. [accessed July 2, 2013].

*Thunis, P., Georgieva, E.* and *Pederzoli, A.*, 2011b: The DELTA tool and Benchmarking report template. Concepts and user guide. Version 2. Ispra, Italy: European Commission Joint Research Centre. Available from: http://fairmode.ew.eea.europa.eu/models-benchmarking-sg4 [accessed July 2, 2013].

*Vincent, K.* and *Abbott, J.*, 2008: Air quality and deposition benefits from Environment Agency regulation. *Environment Agency Science Report SC060108*. Bristol: Environment Agency. https://publications.environment-agency.gov.uk/skeleton/publications/ViewPublication.aspx?id=a98e1cd3-7d34-40ef-8f68-2e401db1bfa4 [accessed May 20, 2013].

*Wild, O., Fiore, A.M., Shindell, D.T., Doherty, R.M., Collins, W.J., Dentener, F.J., Schultz, M.G., Gong, S., MacKenzie, I.A., Zeng, G., Hess, P., Duncan, B.N., Bergmann, D.J., Szopa, S., Jonson, J.E., T. J. Keating, T.J.* and *Zuber, A.*, 2012: Modelling future changes in surface ozone: a parameterized approach. *Atmos. Chem. Phys. 12*, 2037–2054.

*Yu, Y., Sokhi, R.S., Kitwiroon, N., Middleton, D.R.* and *Fisher, B.*, 2008: Performance characteristics of MM5–SMOKE–CMAQ for a summer photochemical episode in southeast England, United Kingdom. *Atmos. Environ. 42*, 4870–4883.

# IDŐJÁRÁS

*Quarterly Journal of the Hungarian Meteorological Service*
*Vol. 119, No. 3, July – September, 2015, pp. 379–398*


# Combined closure single-column atmospheric boundary layer model


**Árpád Bordás*** and **Tamás Weidinger**

*Department of Meteorology, Eötvös Loránd University,*
*P.O. Box 32, H-1518 Budapest, Hungary;*

**Corresponding author E-mail: abordas@caesar.elte.hu*



*(Manuscript received in final form March 20, 2015)*



**Abstract**—This paper presents a development of the first order combined closure (local and nonlocal) single-column atmospheric boundary layer model. The model simulates the turbulent mixing of sensible heat, moisture, and momentum as a split between small scale (subgrid) and large scale (supergrid) processes according to the estimated ratio between local and nonlocal mixing. To verify the validity of the model, an evaluation process was conducted. The evaluation process included controlled offline numerical experiments and tests using the Wangara Experiment database. The obtained vertical profiles and estimated boundary layer heights are in good agreement with the Wangara observation data. Furthermore, uncertainty range affected by the choice of profile functions when estimating the ratio between local and nonlocal mixing processes was analyzed.



*Key-worlds:* atmospheric boundary layer, turbulent mixing, single-column model, combined (local and nonlocal) approach, Wangara Experiment


## *1. Introduction*

Almost all human and biological activities take place in the atmospheric boundary layer (ABL), where the direct effects of the Earth's surface are noticeable. Therefore, the description of the boundary layer characteristics as well as the simulation of the turbulent mixing processes in the ABL are important for weather prediction, air pollution, and environmental modeling. When neglecting horizontal advection, the governing ABL equations in single-column (1D) form for the northern hemisphere are:

$$\frac{\partial \theta}{\partial t} = -\frac{\partial \left(\overline{w'\theta'}\right)}{\partial z}, \tag{1}$$

$$\frac{\partial q}{\partial t} = -\frac{\partial \left(\overline{w'q'}\right)}{\partial z}, \tag{2}$$

$$\frac{\partial u}{\partial t} = f\left(v - v_g\right) - \frac{\partial \left(\overline{u'w'}\right)}{\partial z}, \tag{3}$$

$$\frac{\partial v}{\partial t} = -f\left(u - u_g\right) - \frac{\partial \left(\overline{v'w'}\right)}{\partial z}, \tag{4}$$

where $\theta$ is the potential temperature, $q$ is the specific humidity, $u$ and $v$ are the horizontal wind velocity components, $u_g$ and $v_g$ are the corresponding geostrophic wind components, $\overline{w'\theta'}$, $\overline{w'q'}$, $\overline{u'w'}$, and $\overline{v'w'}$ represent vertical fluxes, $f$ denotes the Coriolis parameter, and $z$ is the vertical coordinate.

Single-column ABL models differ in the main mixing assumption and the approach to the closure problem (*Stull*, 1988; *Foken*, 2006). The choice of a model depends on the aim of investigation and on the modelers' conception. Assuming that the turbulence is analogous to molecular diffusion, different types of first and higher order local closure procedures were developed. This approach is reasonable during conditions of stable and neutral static stability, when the scale of turbulent motion is much smaller than the scale of mean motion. In the convective ABL, where the boundary layer is directly affected by the solar heating of the surface, much of the mixing is caused by buoyant plumes originating in the surface layer and rising to the top of the boundary layer. When using nonlocal mixing schemes (*Blackadar* 1978; *Zhang* and *Anthes*, 1982; *Fiedler* and *Moeng*, 1985), the effects of local mixing during convective conditions are neglected and turbulent mixing is simulated by different size discrete convective elements. To simulate both local (small scale) and nonlocal (large scale) mixing processes simultaneously, combined closure (local and nonlocal) mixing schemes (*Stull*, 1984; *Pleim* and *Chang*, 1992 *Pleim*, 2007a; *Bordás*, 2008) were developed.

Single-column models are very useful tools in ABL investigation. Such models are comprehensive enough to illustrate basic ABL characteristics, simulate boundary layer processes (*Holtslag* and *Boville*, 1993), and compare different parameterization processes (*Alapaty et al.*, 1997; *Bosveld et al.*, 2014). Nesting 1D models in 3D environment, such as MM5 (*Berg* and *Zhong*, 2005; *Pleim*, 2007b) and WRF (*Hu et al.*, 2010; *Shin* and *Hong*, 2011; *Xie et al.*, 2012; *Kleczek et al.*, 2014), we can provide detailed and accurate information of the ABL structure.

The aim of our study is to represent the designed first order single-column ABL model (mixing concept, calculation of turbulent mixing rates, and estimation of the ABL height), which employs a combined (local and nonlocal) mixing scheme, as well as to introduce the model evaluation process done by controlled offline numerical experiments and the Wangara Experiment database. In stable and neutral static conditions, turbulent mixing is simulated as a subgrid (local) process. In unstable conditions, depending on the calculated ratio between local and nonlocal mixing of heat, the model simulates turbulent mixing of sensible heat, moisture, and momentum as a split between small scale and large scale processes. In addition, we analyzed how the type of profile function affected the uncertainty range when estimating the local versus nonlocal character of the turbulent mixing.

## *2. Estimation of the local to nonlocal mixing ratio*

For the combined modeling of the boundary layer processes, it is necessary to define the explicit local and nonlocal vertical fluxes. Many ABL models (*Troen* and *Mahrt*, 1986; *Holtslag* and *Boville*, 1993; *Noh et al.* 2003, *Hong et al.*, 2006) simulate the nonlocal mixing of the different prognostic variables ($c$; $\theta$, $q$, $u$, $v$) including gradient adjustment term ($\gamma_c$) into eddy diffusivity equation as:

$$-\frac{\partial\left(\overline{w'c'}\right)}{\partial z}=\frac{\partial}{\partial z}\left[K_c\left(\frac{\partial c}{\partial z}-\gamma_c\right)\right], \tag{5}$$

where $K_c$ denotes the vertical eddy diffusivity for the quantity of interest. The gradient adjustment term, representing nonlocal influences on the turbulent mixing, can be estimated as (*Holtslag* and *Boville*, 1993):

$$\gamma_c=a\frac{w_*\left(\overline{w'c'}\right)_0}{w_m^2 h}, \tag{6}$$

where $\left(\overline{w'c'}\right)_0$ is the surface kinematic flux of the transported variable, $w_*$ represents the convective velocity scale, $w_m=u_*/\Phi_m$ (where $u_*$ is the friction velocity and $\Phi_m$ denotes the profile function for momentum), $h$ denotes the height of the boundary layer, and $a$ is a semi-empirical constant. Under neutral static conditions for which $w_*=0$, the gradient adjustment term vanishes. This approach is most valid for heat, since surface heat flux is the source and driver of convective turbulence. For other quantities, the surface heat flux is replaced by the surface flux of the transported quantity. However, nonlocal effects may

be driven by mechanisms completely unrelated to convective turbulence. For quantities that have no upward surface fluxes, these models revert to the local eddy diffusivity model.

Following *Pleim* (2007a) from Eq. (5), we can define the ratio between local and nonlocal heat mixing fluxes ($R$) as:

$$R = \frac{K_h \left| \partial\theta / \partial z \right|}{K_h \gamma_h}. \tag{7}$$

When estimating this ratio, it is possible to obtain information about the physical characteristics of the convective boundary layer applicable to any prognostic variable. The surface sensible heat flux can be approximated as:

$$\left(\overline{w'\theta'}\right)_0 = -\kappa \frac{u_* z_s}{\Phi_h} \frac{\partial\theta}{\partial z}, \tag{8}$$

where $z_s$ is the thickness of the surface layer ($z_s = 0.1h$), and $\Phi_h$ denotes the profile function for heat. The convective velocity scale, defined by *Troen* and *Mahrt* (1986) as $w_* = \left[\beta\left(\overline{w'\theta_v'}\right)_0 h\right]^{1/3}$, is estimated in the form:

$$w_* = u_* \kappa^{-\frac{1}{3}} \left(-\frac{h}{L}\right)^{\frac{1}{3}}, \tag{9}$$

where $L$ represents the Monin-Obukhov length scale, and $\kappa$ is the von Kármán constant. The Monin-Obukhov length scale is calculated as:

$$L = -\frac{u_*^3}{\beta\kappa\left(\overline{w'\theta'}\right)_0}, \tag{10}$$

where $\beta$ denotes the buoyancy parameter ($\beta = g / T_0$, $g$ is the acceleration due to gravity, and $T_0$ is the average temperature in the surface layer). According to Eq. (6) to Eq. (10), the ratio between local and nonlocal mixing can be expressed as:

$$R = \left[0.1a\kappa^{\frac{2}{3}} \left(-\frac{h}{L}\right)^{\frac{1}{3}} \frac{\Phi_m^2}{\Phi_h}\right]^{-1}. \tag{11}$$

It can also be linked to the ratio of the nonlocal flux to the total flux ($f_{conv}$), defined by *Pleim* (2007a), as:

$$f_{conv} = \frac{1}{R+1}. \tag{12}$$

The local versus nonlocal turbulent mixing ratio ($R$) defined by Eq. (11) behaves as a function of stability ($-h/L$) and depends on the choice of profile functions for momentum and heat ($\Phi_m^2 / \Phi_h$). Comparing different profile functions, we can analyze the uncertainty caused by the choice of profile functions. *Table 1* lists four often used profile functions for unstable stratification, intervals of definition, and the von Kármán constant used by different authors. The detailed comparison of the profile functions for both stable and unstable conditions, as well as the effects of uncertainties on the calculation of surface layer fluxes are provided by *Weidinger et al.* (2000), *Ács* and *Kovács* (2001), *Arya* (2001), and *Kramm et al.* (2013). *Fig. 1* illustrates how $\Phi_m^2 / \Phi_h$, obtained by the listed profile functions, depends as a function of non-dimensional height ($z/L$). For *Dyer*'s (1974) profile functions, $\Phi_m^2 / \Phi_h$ equals 1 throughout the interval of definition ($-1 \le z/L \le 0$). When using the *Businger et al.* (1971) functions, $\Phi_m^2 / \Phi_h$ is greater than 1, while when applying the *Dyer* and *Bradley* (1982) functions, $\Phi_m^2 / \Phi_h$ is smaller than 1. For both universal function types, $\Phi_m^2 / \Phi_h$ is decreasing about 30% in the first part of the considered interval of definition ($-1 \le z/L \le 0$) and is nearly constant in the second part of the considered interval ($-2 \le z/L \le -1$). For the *Zilitinkevich* and *Chalikov* (1968) functions, $\Phi_m^2 / \Phi_h$ is decreasing rapidly in the total interval of definition ($-1.2 \le z/L \le 0$).

As the aim of the subsequent analysis was to determine whether and to what extent the choice of profile function type influenced the uncertainty range, we used the *Dyer*-type profile functions for which $\Phi_m^2 / \Phi_h$ equals 1 in the interval of definition, and set the von Kármán constant to 0.41. The semi-empirical constant $a$ (see Eq. (6) and Eq. (11)) was set to 7.2 (*Holtslag* and *Boville*, 1993). *Fig. 2* shows how the ratio between local to nonlocal mixing processes ($R$) behaves as a function of stability. To estimate the uncertainty range caused by using different profile functions, the value of the semi-empirical constant $a$ was varied by ± 15% and ± 25%. The obtained results are also presented in *Fig. 2*. For $R = 1$, the local and nonlocal mixing processes are in balance. When the value is higher than 1, it is the local processes that dominate, while when the value is lower than 1, it is the nonlocal processes that prevail. Due to the inverse proportion between $R$ and $a$, when the value of the semi empirical constant is increasing, the effects of local mixing processes are decreasing. Nonlocal processes became dominant for very unstable conditions ($-h/L > 10$). During extremely convective conditions ($-h/L = 30$), the value of $R$ is not lower than 0.65. Our results verify the combined mixing range of the unstable ABL. The uncertainty range is not significantly affected by the choice of profile function type in estimation of the ratio between local versus nonlocal mixing.

*Table 1.* Some frequently used profile functions in the case of unstable stratification,

intervals of definition, and estimation of the von Kármán constant

| | profile function | interval | *k* |
|---|---|---|---|
| *Zilitinkevich* and *Chalikov* (1968) | $\Phi_m = \Phi_h = 1 + 1.45\frac{z}{L}$<br>$\Phi_m = \Phi_h = 0.417\left(-\frac{z}{L}\right)^{-}$ | $-0.16 \le \frac{z}{L} \le 0$<br>$-1.2 \le \frac{z}{L} \le -0.1$ | 0.43 |
| *Businger et al.* (1971) | $\Phi_m = \left(1-15\frac{z}{L}\right)^{-\frac{1}{4}}$<br>$\Phi_h = 0.74\left(1-9\frac{z}{L}\right)^{-\frac{1}{2}}$ | $-2 \le \frac{z}{L} \le 0$ | 0.35 |
| *Dyer* (1974) | $\Phi_m = \left(1-16\frac{z}{L}\right)^{-\frac{1}{4}}$<br>$\Phi_h = \left(1-16\frac{z}{L}\right)^{-\frac{1}{2}}$ | $-1 \le \frac{z}{L} \le 0$ | 0.41 |
| *Dyer* and *Bradley* (1982) | $\Phi_m = \left(1-28\frac{z}{L}\right)^{-\frac{1}{4}}$<br>$\Phi_h = \left(1-14\frac{z}{L}\right)^{-\frac{1}{2}}$ | $-4 \le \frac{z}{L} \le 0$ | 0.4 |

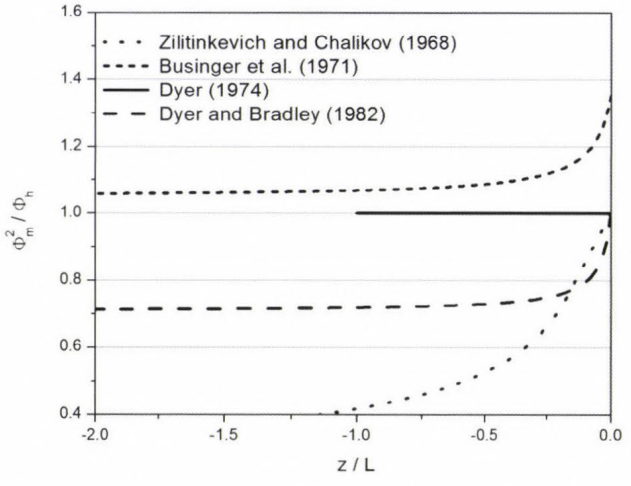


*Fig. 1.* $\Phi_m^2 / \Phi_h$ as a function of non-dimensional height ($z/L$) using different universal functions.

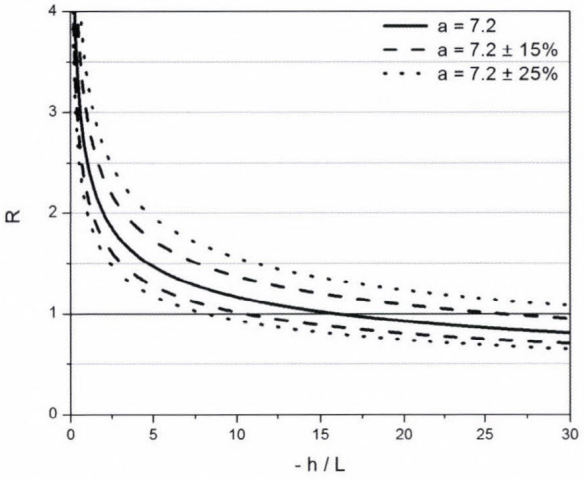


*Fig. 2.* The ratio between local and nonlocal turbulent mixing processes ($R$) as a function of stability.

## *3. Model description*

### *3.1. Mixing concept*

The model designed by the authors describes turbulent mixing during stable and neutral static conditions employing the standard eddy diffusion scheme. For unstable conditions, the model calculates the ratio between local and nonlocal mixing processes ($R$, defined by Eq. (11)) in every time step. According to the calculated ratio, turbulent mixing of sensible heat, moisture, and momentum are simulated as a split between local and nonlocal mixing processes employing a combined (local and nonlocal) closure mixing scheme (*Bordás*, 2008). Stability is defined by the bulk Richardson number method for the lowest model layer. The inclusion of the nonlocal mixing components of momentum can provide more realistic wind profiles for unstable conditions (*Frech* and *Mahrt*, 1995 *Brown* and *Grant*, 1997). However, it is not yet clear how the inclusion of the nonlocal mixing of momentum can improve general properties of a boundary layer model (*Noh et al.*, 2003).

The mixing scheme (*Bordás*, 2008) used for simulating turbulent mixing during unstable conditions combines the local eddy diffusion scheme and the nonlocal Blackadar scheme (*Blackadar,* 1978). The Blackadar scheme describes nonlocal mixing, transporting material directly from the lowest model layer to every other layer and symmetrically from each layer back to the surface layer as it is shown in *Fig. 3*. The explicit value of nonlocal exchange of the prognostic variable at layer $i$ can be calculated as $M(c_1 - c_i)$, where $M\,[\mathrm{s}^{-1}]$ is the convective

mixing rate. Such a model was applied as one of the mixing schemes in MM4 (*Zhang* and *Anthes*, 1982) and MM5 (*Zhang* and *Zheng*, 2004; *Berg* and *Zhong*, 2005) models to simulate boundary layer processes during free convection.

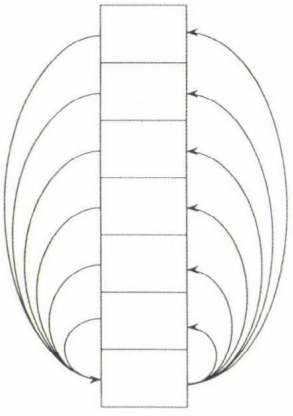

*Fig. 3.* Schematic representation of the Blackadar mixing scheme.

Since the total mixing is simulated as a split between local and nonlocal mixing components, we estimate the weighted vertical eddy diffusivity for heat and momentum ($K'_{hm}$) and the weighted upward mixing rate ($M'$) as:

$$K'_{hm} = \frac{R}{R+1} K_{hm} = (1 - f_{conv}) K_{hm}, \tag{13}$$

and

$$M' = \frac{1}{R+1} M = f_{conv} M . \tag{14}$$

At either extremes ($R \to \infty$ or $R = 0$), the mixing reverts to the simple eddy diffusivity scheme and Blackadar scheme, respectively.

### *3.2. Calculation of the vertical eddy diffusivity and convective mixing rate*

The model defines vertical eddy diffusivity for heat and momentum ($K_{hm}$) by boundary layer scaling, similarly to *Hotlsag* and *Boville* (1993) as:

$$K_{hm}(z) = \kappa \frac{u_* z}{\Phi_{hm}(z/L)} \left(1 - \frac{z}{h}\right)^2, \tag{15}$$

where $\Phi_{hm}$ is the corresponding profile function. The convective mixing rate ($M$) used for any prognostic variable was calculated according to *Pleim* (2007a) as:

$$M = -\frac{1}{h - z_1} \frac{F_{h1}}{\theta_v(z_2) - \theta_v(z_1)}, \tag{16}$$

where $F_{h1}$ is the sensible heat flux in the lowest model layer, $\theta_v(z_2)$ and $\theta_v(z_1)$ represent the virtual potential temperature at the top and bottom of the lowest model layer, respectively, and $z_1$ is the height of the lowest model level. The sensible heat flux in the lowest layer was defined as:

$$F_{h1} = -K_{h1} \frac{\theta_v(z_2) - \theta_v(z_1)}{\Delta z_1}, \tag{17}$$

where $K_{h1}$ denotes the vertical eddy diffusivity for heat in the lowest model layer estimated from the surface layer theory as in Eq. (16) and $\Delta z_1$ represents the thickness of the lowest model layer. Combining Eq. (17) and Eq. (18), the convective mixing rate can be calculated as:

$$M = \frac{K_{h1}}{(h - z_1)\Delta z_1}. \tag{18}$$

### *3.3. Determination of the ABL height*

The height of the ABL, one of the mean characteristics of the boundary layer, shows a strong diurnal variation. The model determines the ABL height by specifying a critical value of the bulk Richardson number ($Ri_b$), defined by:

$$h = Ri_b \frac{u(h)^2 + v(h)^2}{\beta\left[\theta_v(h) - \theta_s\right]}, \tag{19}$$

where $u(h)$ and $v(h)$ are the horizontal wind velocity components at $h$, $\theta_v(h)$ is the virtual potential temperature at $h$, and $\theta_s$ is an appropriate temperature of air near the surface. The near surface potential temperature ($\theta_s$) is calculated as (*Troen* and *Mahrt*, 1986):

$$\theta_s = \theta_v(z_1) + b\frac{\left(\overline{w'\theta_v'}\right)_0}{w_m}, \tag{20}$$

where $b$ is a semi-empirical constant ($b$ = 8.5, *Holtslag et al.*, 1990). The top of the ABL is diagnosed as the height where the bulk Richardson number is equal to the critical Richardson number.

## *4. Model evaluation*

Model evaluation plays an important role in model development. A good ABL model should be able to predict realistic vertical profiles of temperature, humidity, and winds, as well as simulate the morning growth, maximum height, and evening collapse of the boundary layer. During the evaluation process, our model was tested by controlled offline numerical experiments, where initial conditions and forcing were specified. Furthermore, the model tests were performed using the Wangara observational data. The model runs were done with equally spaced vertical layers in $z$ coordinates. Stability was defined by the surface layer bulk Richardson number as: $Ri_0 > 0.01$ for stable conditions, $-0.01 \leq Ri_0 \leq 0.01$ for neutral static conditions, and $Ri_0 < -0.01$ for the unstable boundary layer. For the test runs, *Dyer*'s (1974) profile functions were used, and the semi empirical constant $a$ necessary to estimate ratio between local and nonlocal mixing processes (see Eq. (12)) was set to 7.2 (*Holtslag* and *Boville*, 1993). The top of the ABL is diagnosed as the height where the bulk Richardson number is equal to the critical Richardson number, which value was set to 0.25 (*Holtslag et al.*, 1990).

### *4.1. Controlled offline numerical experiments*

The controlled offline experiments were performed for a dry atmosphere with a defined initial potential temperature ($\theta$) and horizontal wind ($u$ and $v$) profiles. The constant potential temperature increase of the lowest model level was determined with a magnitude of 0.16 K/h (*Nieuwstadt et al.*, 1992), the roughness length was set to 0.1 m, and the geostrophic wind components were $u_g$ = 10 m/s and $v_g$ = 0 m/s at all levels.

The simulated potential temperature profiles after the 4th and 8ht hour of integration obtained by estimating the ratio between local and nonlocal mixing processes ($R$) in every time step are presented in *Fig. 4*. The vertical model resolution was 50 m. The simulated profiles show a downward gradient from the ground up to 2/3 of the ABL height. *Fig. 5* compares profiles shown in *Fig. 4* (varying $R$), profiles obtained assuming that during unstable conditions the local and nonlocal mixing processes are in equilibrium ($R = 1$), and profiles simulated

by the local eddy diffusivity scheme ($R \to \infty$). As expected, the defined weak forcing local mixing processes were dominant and the profiles obtained by the varying ratio between local and nonlocal mixing processes showed a more local than a nonlocal character.

*Fig. 6* describes the time evolution of the ABL height simulated by different vertical model resolutions (25 m, 50 m, and 100 m) by the varying ratio between local and nonlocal mixing processes. Since weak forcing was used in the simulation, the ABL height increased slowly. The estimation of the boundary layer height was independent of vertical resolution. Performed controlled numerical experiments showed that simulated potential temperature ($\theta$) as well as horizontal wind ($u$ and $v$) profiles were also free of vertical model resolution. The profiles obtained for eastward ($u$) and northward ($v$) wind components simulated after the 4th and 8th hours of integration by varying $R$ are presented in *Fig. 7*. Model runs were done by 50 m vertical resolution. *Fig. 8* compares the horizontal wind profiles simulated by the eddy diffusivity scheme ($R \to \infty$), constant ($R = 1$), and varying ratio between local and nonlocal processes (profiles shown in *Fig. 7*). The differences among combined closure profiles are negligible. These profiles simulate slightly higher $v$ wind speeds in the mixed layer and slightly lower $u$ wind speeds near the top of the ABL than profiles obtained by local closure approach.

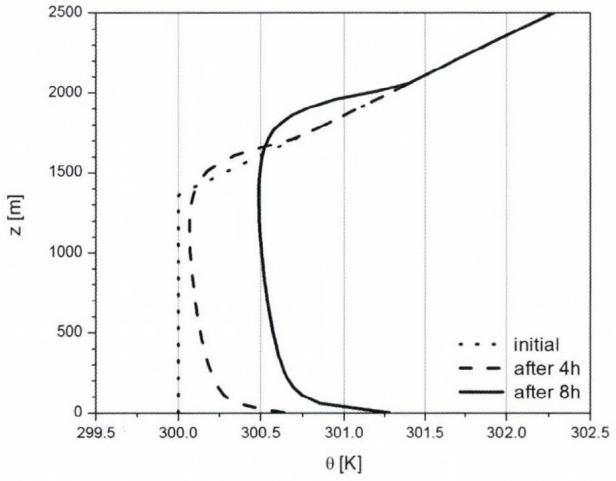


*Fig. 4.* Potential temperature profile at initial time and simulated after the 4th and 8th hour of integration.

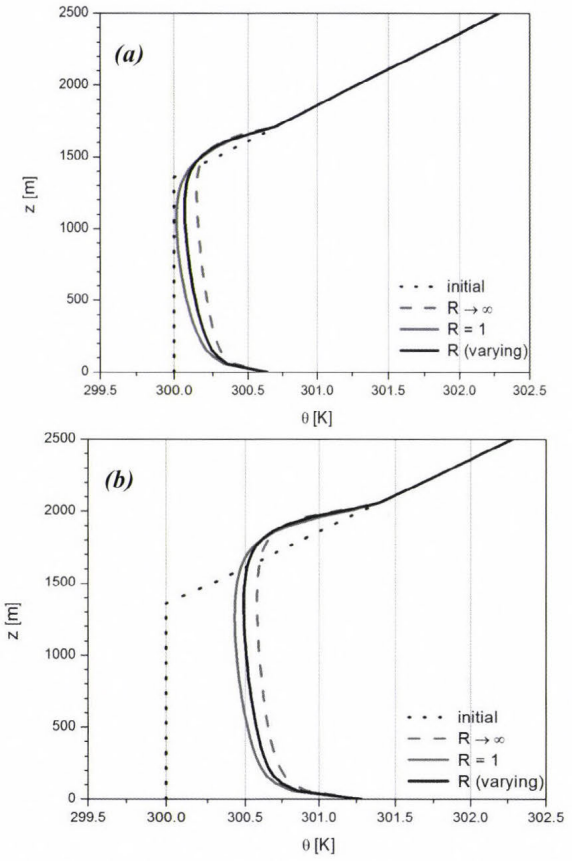


*Fig. 5.* Potential temperature profiles at initial time and simulated after the 4th *(a)* and 8th *(b)* hour of integration by different mixing approaches.

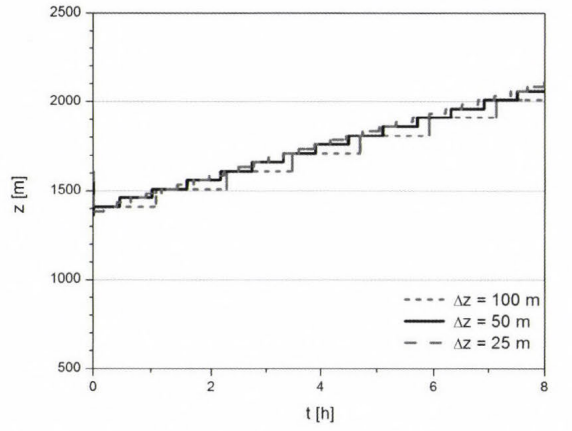


*Fig. 6.* Time evolution of the ABL height obtained by different vertical resolutions.

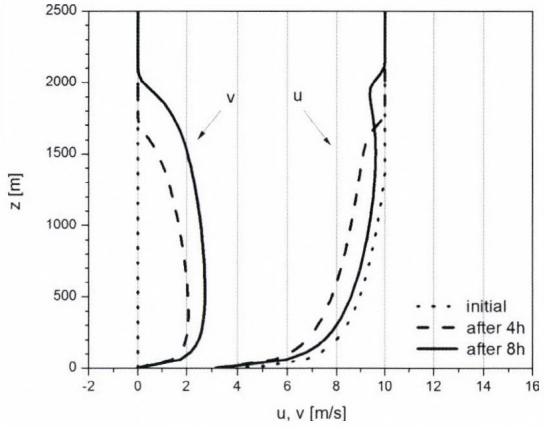


*Fig. 7.* Horizontal wind profiles at initial time and simulated after the 4th and 8th hour of integration.

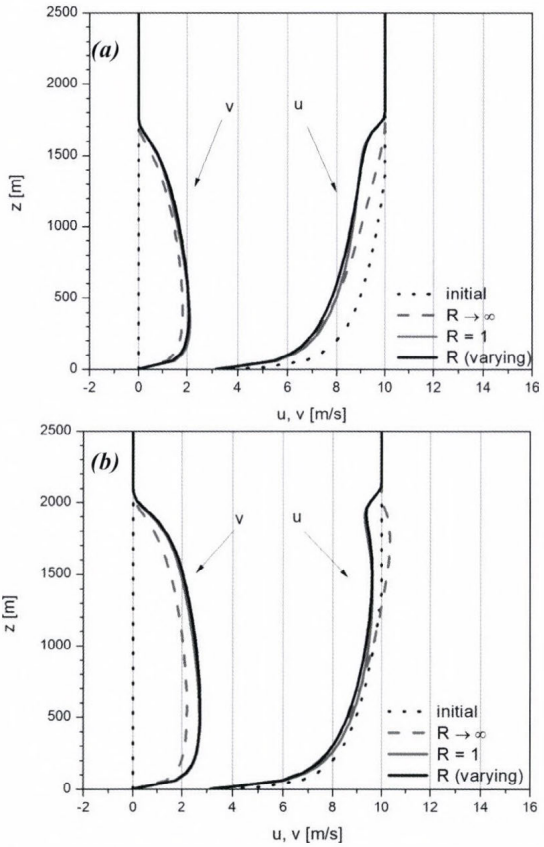


*Fig. 8.* Horizontal wind profiles at initial time and simulated after the 4th *(a)* and 8th *(b)* hour of integration by different mixing approaches.

*4.2. Comparison with the Wangara observations*

The Wangara campaign (*Clarke et al.*, 1971; *Hess et al.*, 1981) was one of the first field experiments to define the universal characteristics of the ABL. It was conducted in July and August 1967 near Hay (New South Wales, Australia). The name "Wangara" was taken from an Aboriginal word for "west wind", which was the primary focus of the experiment. The area was selected because of its flatness, small slope, and all-weather accessibility. The observational site was located over a sparsely and uniformly vegetated region close to a desert. Over such areas, errors arising from the insufficient representation of vegetation-atmosphere interactions should be at a minimum during simulations. The high density of the observational network and the availability of many meteorological parameters (pilot balloons were released hourly, radiosonde every three hours) made the Wangara database very popular for model comparison and evaluation studies.

Our model tests were done using the data for day 33 (August 16) of the Wangara database. This particular day has been used quite often as a test case for different types of ABL models (*Yamada* and *Mellor*, 1975; *Pleim* and *Xiu*, 1995; *Alpaty et al.*, 1997; *Xue et al.*, 2001.; *Cara-Lyn et al.*, 2010) because the sky was clear the whole day and horizontal advection was very weak. Our model calculations were done by a 50 m vertical model resolution. The vertical resolution of the Wangara data is 50 m from the land surface to 1000 m, and 100 m from 1000 m to 2000 m. The initial profiles for the potential temperature ($\theta$), water vapor mixing ratio ($q$), and horizontal wind components ($u$, $v$) were the observed values at 0900 LT (local time). The time variation of these quantities at the lowest model level were set explicitly as a lower boundary condition in the model. The virtual potential temperature was calculated using measured and simulated data for potential temperature and water vapor mixing ratio. According to *Yamada* and *Mellor* (1975), the roughness length was set to 0.01 m.

Observed and modeled (by varying $R$) virtual potential temperature profiles at four times during day 33 are shown in *Fig. 9*. The profile at 0900 LT shows a stable boundary layer. By 1200 LT, the inversion was dissipated and a convective layer was formed in both vertical profiles. The predicted top of the ABL is slightly underestimated. From 1200 LT to 1500 LT, the mean mixed layer warmed up by about 2 K. At 1800 LT, the profiles show a formed surface inversion with a well mixed residual layer.

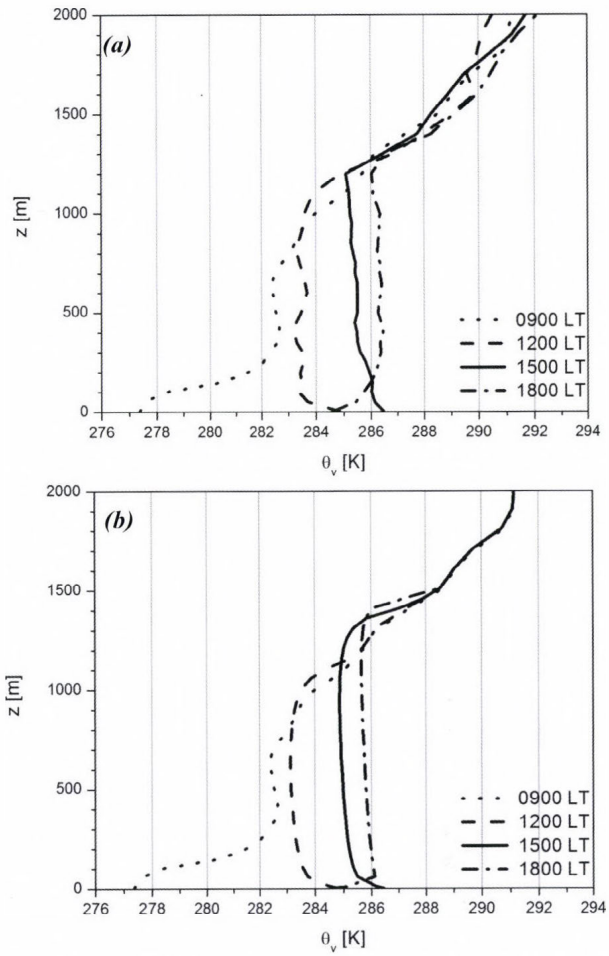


*Fig. 9.* The Wangara observational *(a)* and modeled *(b)* virtual potential temperature profiles.

*Fig. 10* compares the virtual potential temperature profiles obtained by the eddy diffusivity scheme ($R \to \infty$), a combined mixing scheme with constant ($R = 1$), and a varying (varying $R$) ratio between mixing processes at 1200 LT and 1500 LT. The predicted profiles for 1200 LT are very close to the observations. At lower altitudes it is the combined closure profiles, while near the top of the boundary layer it is the local closure profile that fit the Wangara data better. The differences between the simulated and observed profiles for 1500 LT are higher. In the lower part of the boundary layer, the best fit was obtained by the local closure profile. The combined closure profiles, on the other hand, estimate the height of the boundary layer better.

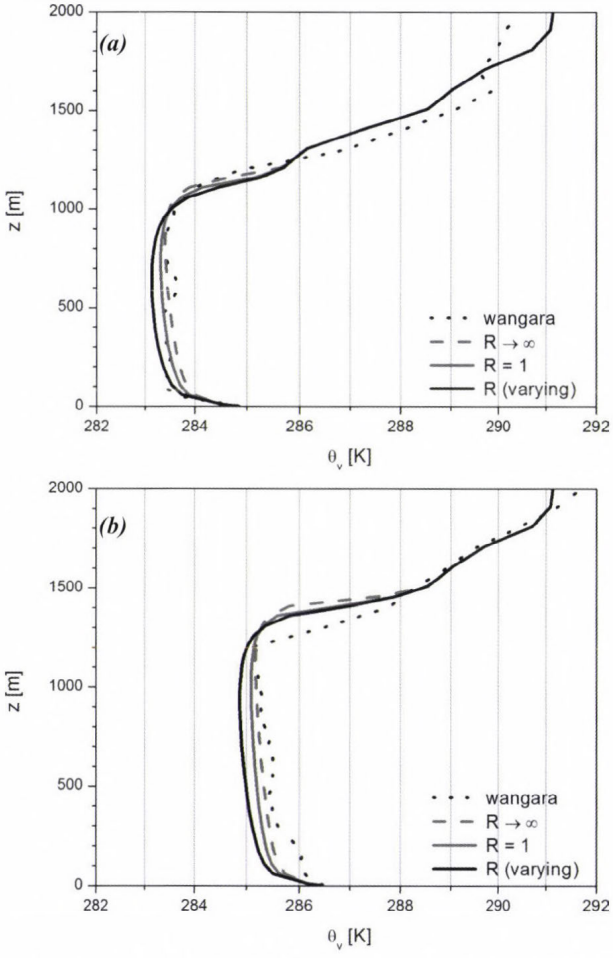


*Fig. 10.* Comparison of simulated and observational virtual temperature profiles at 1200 LT *(a)* and 1500 LT *(b)*.

The observed and modeled ABL heights are presented in *Fig. 11.* The observations were estimated using two methods from radiosonde measurements: as reported by *Yamada* and *Mellor* (1975), and by applying the determination process described in Section 3.3. The time resolution of the three ( $R \to \infty, R = 1$, and varying $R$) modeled ABL heights is one hour. The modeled and observed heights agree very well in timing of rise, and they also predict the collapse of the ABL. At 1800 LT, when the ground-based inversion was developed, the first observational method actually represents the top of the residual layer.

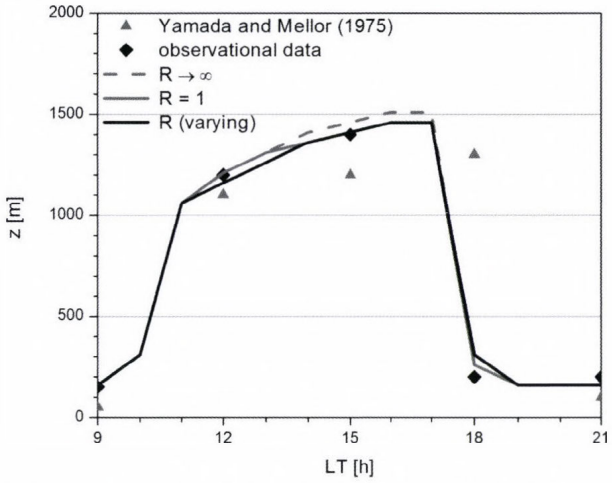


*Fig. 11.* Temporal evolution of the estimated and predicted height of the ABL for the Wangara simulation.

*Fig. 12* compares the observed and the three predicted ($R \to \infty$, $R = 1$, and varying $R$) horizontal wind profiles at 1200 LT and 1800 LT. Geostrophic wind profiles were estimated from a parabolic fit to the thermal wind data as suggested by *Yamada* and *Mellor* (1975). As a function of height and time, the resulting geostrophic winds were supplied to the model as input. The differences between the modeled profiles are very small, with the highest difference being approximately 0.5 m/s. These profiles show similar features to the observations. For 1200 LT, the $v$ profiles fit well, while the $u$ profiles underestimate the observational data. Underestimation is explicit from 800 m to the top of the boundary layer at 1150 m. The predicted winds at 1800 LT are close to the observations. The simulated $u$ profiles slightly underestimate, while $v$ profiles at lower altitudes overestimate the measured data. The average difference between the estimated and measured values is about 1 m/s. The differences between the observed and simulated profiles may be due to the uncertainty in geostrophic wind estimation (*Yamada* and *Mellor*, 1975).

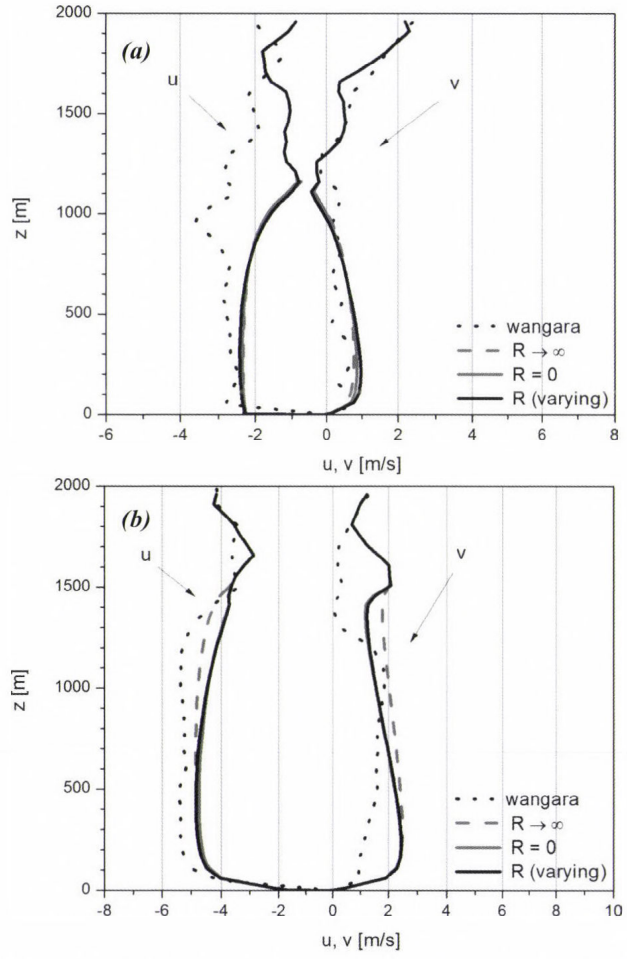


*Fig. 12.* Observed and simulated horizontal wind profiles at 1200 LT *(a)* and 1800 LT *(b)*.

## *5. Summary*

This paper presents a first order single-column (1D) ABL model with a combined closure approach. In order to describe ABL properties as accurately as possible, the model calculates the local to nonlocal mixing ratio in every time step. According to the current ratio, the model simulates the turbulent mixing of prognostic variables as a split between small scale and large scale components. The obtained mixing ratio values verify the combined character of the turbulent mixing during unstable conditions. It was also proven that the uncertainty range caused by the choice of profile function types does not have a significant bearing on the obtained results.

In order to verify the validity of the model, controlled offline numerical experiments were conducted. These experiments showed that the designed model is able to simulate realistic potential temperature and wind profiles, and indicate differences among local and combined closure. A comparison with the Wangara Experiment data demonstrated a good agreement between the measured and simulated vertical profiles and it also provided a reasonably accurate estimation of the ABL height during the temporal evolution and collapse. The next step in our work is to incorporate the presented single column model into the WRF model and compare the obtained model outputs with other first and higher order profiles simulated in 1D and 3D environments.

***Acknowledgements***: The authors thank the European Union and the European Social Fund for their financial support (grant agreement no. TÁMOP-4.2.1.B-11/2/KMR-2011-0001 "Critical infrastructure defense research") during the preparation of this paper. The financial support of the Hungarian Scientific Research Foundation (OTKA, project no. K83909, and no. NN109679) is also greatly appreciated.

## *References*

*Ács, F.* and *Kovács, M.*, 2001: The surface aerodynamic transfer parameterization method SAPA: description and performance analyses. *Időjárás 105*, 165–182.

*Alapaty, K., Pleim, J.E., Raman, S., Niyogi, D.S.,* and *Byune, D.W.*, 1997: Simulation of atmospheric boundary layer processes using local- and nonlocal-closure schemes. *J. Appl. Meteorol. 36*, 214–233.

*Arya, P.S.*, 2001: Introduction to micrometeorology. Academic Press, San Diego.

*Berg, L.K.* and *Zhong, S.*, 2005: Sensitivity of MM5-simulated boundary layer characteristics to turbulence parameterizations. *J. Appl. Meteorol. 44*, 1467–1483.

*Blackadar, A. K.*, 1978: Modeling pollutant transfer during daytime convection. 4th Symposium on Atmospheric Turbulence, Diffusion and Air Quality. Reno, NV, USA, 443–447.

*Bordás, Á.*, 2008: One-column vertical turbulent mixing model for the atmospheric convective layer. *Phys. Scr. T132*, 5.

*Bosveld, F.C., Baas, P., Steeneveld, G.-J., Holtslag, A.A.M., Angevine, W.M., Bazile, E., de Bruijn, E.I.F., Deacu, D., Edwards, J.M., Ek, M., Larson, V.E., Pleim, J.E., Matthias Raschendorfer, M.,* and *Svensson, G.*, 2014: The third GABLS intercomparison case for evaluation studies of boundary-layer models. Part B: results and process understanding. *Bound.-Lay. Meteorol. 152*, 157–187.

*Brown, A.R.* and *Grant, A.L.M.*, 1997: Non-local mixing of momentum in the convective boundary layer a review of flux-profile relationships. *Bound.-Lay. Meteorol. 84*, 1–22.

*Businger, J.A., Wyngaard, J.C., Izumi, Y.,* and *Bradley, E.F.*, 1971: Flux-profile relationships in the atmospheric surface layer. *J. Atmos. Sci. 28*, 181–189.

*Cara-Lyn L., Randall, D.,* and *Yamaguchi, T.*, 2010: A higher-order closure model with an explicit PBL top. *J. Atmos. Sci. 67*, 834–850.

*Clarke, R.H., Dyer, A.J., Brook, R.R., Reid, D.G.,* and *Troup, A.J.*, 1971: The Wangara Experiment: boundary layer data. *Tech. Paper No. 19*, CSIRO, Div. Meteor. Phys.

*Dyer, A. J.*, 1974: A review of flux-profile relationships. *Bound.-Lay. Meteorol. 7*, 363–372.

*Dyer, A.F.* and *Bradley, E.F.*, 1982: An alternative analysis of flux-gradient relationships at the 1967 ITCE. *Bound.-Lay. Meteorol. 22*, 3–19.

*Fiedler, B.H.* and *Moeng, C.-H.*, 1985: A practical integral closure model for mean vertical transport of a scalar in a convective boundary layer. *J. Atmos. Sci. 42*, 359–363.

*Foken, T.*, 2006: Angewandte Meteorologie, Mikrometeorologische Methoden. Springer, Heidelberg.

*Frech, M.* and *Mahrt, L.*, 1995: A two-scale mixing formulation for the atmospheric boundary layer. *Bound.-Lay. Meteorol. 73*, 91–104.

*Hess, G.D., Hicks, B.B.*, and *Yamada, T.*, 1981: The impact of the Wangara Experiment. *Bound.-Lay. Meteorol. 20*, 135–174.

*Holtslag, A.A.M.* and *Boville, B.A.*, 1993: Local versus nonlocal boundary-layer diffusion in a global climate model. *J. Climate 6*, 1825–1842.

*Holtslag, A.A.M., De Bruin, E.I.F.*, and *Pan, H.-L.*, 1990: A high resolution air mass transformation model for short-range weather forecasting. *Mon. Weather Rev. 118*, 1561–1575.

*Hong, S.-Y., Noh, Y.*, and *Dudhia, J.*, 2006: A new vertical diffusion package with an explicit treatment of entrainment process. *Mon. Weather Rev. 134*, 2318–2341.

*Hu, X.-M., Nielsen-Gammon, J.W.*, and *Zhang, F.*, 2010: Evaluation of three boundary layer schemes in the WRF model. *J. Appl. Metorolol Climate 49*, 1831–1844.

*Kleczek, M.A., Steeneveld, G.-J.*, and *Holtslag, A.A.M.*, 2014: Evaluation of the Weather Research and Forecasting mesoscale model for GABLS3: impact of boundary-layer schemes, boundary conditions and spin-up. *Bound.-Lay. Meteorol. 152*, 213–243.

*Kramm, G., Amaya, D.J., Foken, T.*, and *Mölders, N.*, 2013: Hans A. Panofsky's Integral Similarity Function – At Fifty, *Atmos. Climate Sci. 3*, 581–594.

*Noh, Y., Cheon, W.G., Hong, S.Y.*, and *Raasch, S.*, 2003: Improvement of the K-profile model for the planetary boundary layer based on large eddy simulation data. *Bound.-Lay. Meteorol. 107*, 401–427.

*Nieuwstadt, F.T.M., Mason, P.J., Moeng, C.-H.*, and *Schumann, U.*, 1992: Large Eddy Simulations of the Convective Boundary Layer: A Comparison of Four Computer Codes. In Turbulent Shear Flows Vol. 8, Springer, 343–367.

*Pleim, J.E.*, 2007a: A combined local and nonlocal closure model for the atmospheric boundary layer. Part I: model decription and testing. *J. Appl. Metorol. Climate 46*, 1383–1395.

*Pleim, J.E.*, 2007b: A combined local and nonlocal closure model for the atmospheric boundary layer. Part II: application and evaluation in a mesoscale meteorological model. *J. Appl. Metorol. Climate 46*, 1396–1409.

*Pleim, J.E.* and *Chang, J.S.*, 1992: A non-local closure model for vertical mixing in the convective boundary layer. *Atmos. Environ. 26A*, 965–981.

*Pleim, J.E.* and *Xiu, A.*, 1995: Development and testing of a surface flux and planetary boundary layer model for application in mesoscale models. *J. Appl. Meteorol. 34*, 16–34.

*Shin, H.H.* and *Hong, S.–Y.*, 2011: Intercomparison of Planetary Boundary-Layer Parametrizations in the WRF Model for a Single Day from CASES-99. *Bound.-Lay. Meteorol. 139*, 261–281.

*Stull, R.B.*, 1984: Transilient tubulence theory. Part I: The concept of eddy-mixing across finite distances. *J. Atmos. Sci. 41*, 3351–3367.

*Stull, R.B.*, 1988: An introduction to Boundary layer meteorology. Kluwer Academic Publ., Dordrecht.

*Troen, I.B.* and *Mahrt, L.*, 1986: A simple model of the atmospheric boundary layer; sensitivity to surface evaporation. *Bound.-Lay. Meteorol. 37*, 129–148.

*Weidinger, T., Pinto, J.*, and *Hotváth, L.*, 2000: Effects of uncertainties in universal functions, roughness length, and displacement height on the calculation of surface layer fluxes. *Meterorol. Z. 9*, 139–154.

*Xie, B., Fung, J.C.H, Chan, A.*, and *Lau, A.*, 2012: Evaluation of nonlocal and local planetary boundary layer schemes in the WRF model. *J. Geophys. Res. 117*, D12103.

*Xue, M., Droegemeier, K. K., Wong, V., Shapiro, A., Brewster, K., Carr, F., Weber, D., Liu, Y.*, and *Wang, D.*, 2001: The advanced regional prediction system (ARPS) – a multi-scale nonhydrostatic atmospheric simulation and prediction tool. Part II: model physics and applications. *Meteorol. Atmos. Phys. 76*, 143–165.

*Yamada, T.* and *Mellor, G.*, 1975: A simulation of the Wangara atmospheric boundary layer data. *J. Atom. Sci. 32*, 23099–2329.

*Zilitinkevich, S.S.* and *Chalikov, D.V.*, 1968. Determining the universal wind-velocity and temperature profiles in the atmospheric boundary layer. *Izv. Atmospheric and Oceanic Physics 4*, 2949–302. (English version 1659–170.)

*Zhang, D.* and *Anthes, R.A.*, 1982: A high-resolution model of the planetary layer – sensitivity tests and comparison with SESAME-79 data. *J. Appl. Meteor. 21*, 1594–1609.

*Zhang, D.L.* and *Zheng, W.Z.*, 2004: Diurnal cycles of surface winds and temperatures as simulated by five boundary layer parameterizations, *J. Appl. Meteor. 43*, 157–169.

# IDŐJÁRÁS

*Quarterly Journal of the Hungarian Meteorological Service*
*Vol. 119, No. 3, July – September, 2015, pp. 399–408*


# Effects of atmospheric ions on human well-being in indoor environment


**Levente Herczeg*** and **Norbert Érces**

*Department of Building Service Engineering and Process Engineering*
*Budapest University of Technology and Economics*
*Műegyetem rkp. 3, H-1111, Budapest*

*Corresponding author E-mail: l.herczeg@hfhc.hu



*(Manuscript received in final form October 15, 2014)*



**Abtract**—People spend a significant part of their days in buildings or in a box within some kind of means of transport. It is one of the main issues in our fast-paced world that typifies the twentieth and twenty-first centuries. Consequently, suitable environment creation plays an increasingly important part, which has significant influence on human comfort, health, and productivity as well. It turns out in pursuance of developments in various heating, ventilation and air conditioning (HVAC) systems that human comfort is affected not only by air temperature, humidity, and draught but also by meteorological, physiological, and psychological parameters. Airborne particles, so-called atmospheric ions assessments have been carried out in the course of these investigations. This paper presents effects of atmospheric ions on indoor environment and the occupants.



*Key-words*: atmospheric ions, human well-being, air quality, comfort spaces, measurement technique


## *1. Introduction*

The comfort in closed spaces is usually understood as thermal, air quality, acoustical, and illumination engineering comfort. The office plays a special role in providing adequate comfort as workers spend a longer time in closed spaces performing intellectual work. In the air-conditioning of comfort spaces, the primary task is to provide a pleasant indoor microclimate for the people staying in the room. In addition to thermal comfort, air quality is also regulated by international requirements and standards. In the occupied zone, a sufficient

amount of fresh air of appropriate quality must be provided for the people staying in the room. Hungarian technical regulations do not fully cover these aspects yet, hence the complaints frequently heard from employees working in air-conditioned spaces are the air has an unpleasant 'smell', they experience 'lack of air' or perhaps have headaches (*Kajtár* and *Hrustinszky*, 2001, 2002, 2003; *Kajtár* and *Herczeg*, 2012; *Kalmár* and *Kalmár,* 2013) In addition to the impact on human's health- and comfort factors, extensive studies were carried out on the effect of atmospheric ions.

## *2. Physical attributes of atmospheric ions*

According to Henri Hess (1802–1850), a Swiss chemist, every type of gases contains electrically – positively or negatively – charged particles called ions. One singular ion carries 4.77·10-10 electrostatic values (ESV) charge. Under this force, ions will migrate in an electric field according to the type of their charge. Basically, two types of ions are distinguished: small or molecular ions and large, i.e., Langevin ions. Certainly dimensional differences can be observed in regard to ion velocity as well. Under normal air conditions, small ions are moving at 1–2 cm/s, and large ones at 0.01–0.005 cm/s, depending on their size. Velocity of negatively charged ions is usually higher than in case of positive ones.

In nature, ions are formed because of the radiation of sun, cosmic rays, and fluctuations of radioactivity within the lithosphere on the Earth. Highly ionized gases are approaching the Earth surface due to a capillary action generated by wind suction. Considering the total number of ions in the air, it is in the order of 60%. Stage of atmospheric ionization is simultaneously influenced by other natural processes which attempt to destroy or neutralize the ions.

The most important factors and processes are:

- bonds between oppositely charged ions,
- neutral ions creation, aggregation with condensation centers,
- large ions creation, and
- absorption by solid or liquid conductors (*Kérdő et al.,* 1972).

### *2.1. Determination of the number of atmospheric ions*

Positively and negatively charged atmospheric ions in the air usually measured with the Ebert counter or with a modified version of that. The examined air sample is forced trough a cylindrical condenser with an electrode pole fitted in the middle. This electrode is oppositely charged than ions which should be measured, and only sufficiently high-speed ions are able to reach it. In the course of collision, pole subtracts electrons equally to the charge of ions. Based on the quantity of electrical discharges and the airflow measured by a damping plate, the number of ions can be determined in a given amount of air.

The ion concentration depends significantly on the time of day, weather conditions, and location, moreover the number of occupants and their activity (*Yaglou,*1935).

### *3. Effects of atmospheric ions on human physiology*

First interdisciplinary study of biological and medical influents of ionized air was published by *Dessauer* in 1931. In the course of their assessments, ionized air was conducted directly on the face of participants through a funnel. Exposure had been taking 15–60 minutes, at concentration of $10^6$ ions/cm$^3$. It was clearly established that positive and negative ions had different effects on human health, amongst healthy participants and inpatients too. Positive ions induced discomfort, headache, rising blood pressure and respiratory rate. Moreover, they generate occasionally a feeling of being sick. Negative ions had opposite influences which led to sense of refreshment and decreased blood-pressure.

Effects of atmospheric ions were evaluated in a more cautious way in a research had been carried out by Harvard School of Public Health in 1933. In the course of investigations, ions formed by small molecules were dispersed into the experimental space with a velocity of 1.3 cm/s. Concentrations of positive and negative ions were continuously varying between 5000–1 500 000 ions/cm$^3$. Applied ionizer could produce simultaneously positive and negative ions. Temperature in the experimental room was set according to the personal demands. Air-change rate was 35, without usage of a humidifier.

Examination series were divided into three groups:

- normal ground state,
- 2–4 hours after breakfast, and
- 3–5 hours after an easy lunch.

During the investigation, variations in metabolism, breathing, pulse rate, blood pressure, and body temperature were recorded in regard to each test persons, who aged from 10 to 68 years. The group of 60 participants was observed during 141, one or more hour long experiments under influence of ionized air. It was established that intake air can normalize body processes, i.e., accelerate physiological changes if personal results are above or below the normal rate. Significant influences of positive and negative charges could not be determined. However, based on evaluation of subjective physiological effects, the following statements can be made: exposure to positive ionization causes headache, nose and throat irritation. Negative ionization led to a feeling of being calm. A small group of test persons reported sense of freshness, especially affected by negative ionization (*Yaglou et al.,* 1933).

## *4. Measuring investigations of atmospheric ions*

### *4.1. Description of measurements*

To purpose of this chapter is to present how ion number is varying and what the influence of that is on occupants being in different places. Since 1930s, several measurements have been taken in areas in towns, subway stations, and residential enclosures, in order to answer these questions.

Under conditions of natural ion climate which is beneficial to health, numbers of positive and negative ions are equal to each other in terms of scale, and concentration of biological effective ions is in the range of 500–4000 ions/cm$^3$. Due to changes generated by civilisation, atmospheric ion concentration rates scattered in cities and industrial areas are fundamental. Number of large ions will be significantly increased by polluted air. Consequently small, biological effective, negatively charged ions are almost completely disappearing. Several studies were carried out by *Yaglou* and *Benjamin* between 1930 and 1934 in relation of various meteorological parameters. Seasonal phenomena, influences of temperature, humidity, clouds, precipitation, and changes in atmospheric pressure were also taken into consideration. Results from the three-year-long assessments show adequate similarity, presenting definite minimum ion concentration in winter, and maximum in summer. Winter of 1930–31 was extremely cold. Therefore, results for this period had been deleted afterwards. Indoor level of ionisation was lower than in outdoor air during winter and springtime of 1932–33. In summertime this deviation could not be observed. In comparison with measurements at Pacific, Atlantic, and Indian Oceans (1915–16), corresponding variation in ion concentrations was established. However, comparing results had not been considered sufficient to provide an adequate basis in regard to both land and water surface measurements. Related to the connection between yearly changes and ionization, no conclusions were made as further measurements had been considered inaccurate. Ion concentration influenced by air temperature and humidity was evaluated in a more adequate way. Increased wind velocity leads to a consequent decrease in ion concentration at any time of the year, independently from temperature levels. Low concentration of small ions starts to be appreciable below air temperature of 21 °C. Thus, minimal concentration in winter becomes out of question as the humidity is at the highest level and temperature is at the lowest level simultaneously. Presence of high ion concentration can be noticed at relative humidity of 75%, independently of temperature parameters. Ion concentration level is varied with both cloudy and partly cloudy weather. In fact, clouds which cover the sky completely or partly will decrease ion concentration significantly. There is similar effect both of light and moderate rain. Heavy rain and storms accompanied by lighting and very heavy precipitations will increase the level of negative ion

concentration definitely. If storm approaches its peak, this can reach the level of the zenith point of ion concentration 3000–3150 ions/cm$^3$. Indoor ion concentration depends considerably both on the amount and duration of precipitation and the direction of the wind. A few hours of light or moderate rain has no major impact on indoor ion concentration.

Number of ions formed by surface radioactivity is influenced by barometric effect which can be measured near the ground. If Earth's capillaries are under a decreased pressure, more ions will be released. This kind of "ground breathing" becomes heavy at an increased level of pressure. However, these are not significant changes.

### *4.2. Measurement results in Hungary*

Obviously, studies on atmospheric ionization have been made in Hungary too. István Kérdő candidates of medicine, and Ferenc Sváb electrical engineer had been performed two assessments, in Budapest on October 12, 1970 and in Stuttgart on July 28, 1972 (*Kérdő et al.*, 1972). Results of their studies are presented in *Table 1*.

*Table 1.* Variation of atmospheric ion number in urban area (*Kérdő et al.*, 1972)

| **Location** | **Temperature [$^0$C]** | **Relative humidity [%]** | **n+ [ions/cm$^3$]** | **n- [ions/cm$^3$]** | **n+/n- [-]** |
|---|---|---|---|---|---|
| Budapest, 200 m far from Danube | 21–18 | 56–62 | 120–130 | – | – |
| North, 14 km far from Budapest | 21 | 60 | 250–300 | 120–140 | 2.08–2.14 |
| Budapest, Nyugati square | 21 | 60 | 120–140 | 20–30 | 6.00–4.67 |
| Budapest, Jászai Mari square | 18 | – | 50–100 | 10–20 | 5.00 |
| Budapest, Boráros square | 18 | – | 130–170 | 20–40 | 6.50–4.25 |
| Budapest, Nagyvárad square | 18 | – | 100–130 | 20–30 | 5.00–4.33 |
| Stuttgart, Entrance of Wagenburg tunnel | 20 | 61 | 300–500 | 20 | 15–25 |
| Stuttgart, Kriegsberg road | 20 | 61 | 200–220 | 30–40 | 6.67–5.50 |
| Stuttgart,Bosch Hospital, 115 m altitude | 20 | – | 270–290 | 20–30 | 13.5–9.67 |
| Stuttgart, TV Tower | 20 | – | 110–130 | 120–130 | 0.92–1.00 |

The above mentioned phenomena can be observed, i.e., number of negatively charged ions could be considered negligible or non-measurable in higher polluted environment. However, results measured in the TV tower of Stuttgart verified the theory that unipolarity is near to one in clean environment, so positively and negatively charged ions are dimensionally equated to each other. It shows the importance of negative ions, which can primary affect the physiological parameter, one of the earlier mentioned factors influencing human comfort.

### *4.3. Recent researches*

After the first, remarkable researches in the 1930s which had been processed without achieving a real breakthrough, in the 1960s a new attempt was made in order to define effects of atmospheric ions on occupants in residential spaces. In the course of investigations it was discovered, that a significant amount of positively and negatively charged ions could be generated by humidifiers and vaporizers in the air conditioning devices. As it can be seen in *Table 1*, in case of TV Tower of Stuttgart, natural ions are approximately balanced, but usually more positively charged ions can be found in a cubic centimeter. In general, this number is below 1000 ions/cm$^3$ in a clean, natural environment. It can be observed that certain human activities, especially ones accompanied by a considerable heat load form positively charged ions. Therefore, man got used to the presence of positive ions more likely. In accordance with the study presented above, this could also give an explanation for the favorable effects of negative ions on human well-being, as the surplus of negatively charged ions could create a perceptible change in well-being. However, this statement was handled with care, even after the study of *Jennings* in 1964 (*Jennings* and *Givoni*, 1964) . As previous investigations, this was also performed in an artificial environment, where ion concentration in air could be increased above the natural level. All the experiments had been performed in the research lab chamber for environmental studies of American Society for Engineering Education (ASEE) which is a room with internal size of 7.5×3.5×2.55 meters. Both indoor air temperature and humidity were controlled by an air conditioning device. In the room, four ion generators were installed. Likewise in the 1930s, adjustable devices could be set for producing or counting either positive or negation ions. The pilot studies showed that there was no direct correlation between the ion concentration in the room and the number of ionizators, since two generators could produce the same high level of ion concentration as the four together. Still simultaneous use of the four devices were considered practical, in order to ensure homogeneity.

In the course of the assessment, 16 people (12 woman and 4 men) were employed as test persons. Before the ionization, each of them has gone through a general physical examination. Initial studies were performed between July 19 and 22, at a relative humidity of 50%. These were reproduced between July 25

and February 2, also at the same humidity level but at a temperature level of 30.5 °C in order to observe the reactions of the same test persons at mild heat stress. Both measurement series were remade between April 19 and May 26. Two groups of 6–8 persons were established and observed in the daytime and at night during each investigation. Three levels of ionization were distinguished:

- basic, when ionizators did not worked,
- negative ionization,
- positive ionization.

In the course of examinations, a special attention was paid to ensure random change in the three levels, in order to avoid any effects of the different ionization statuses. Ionizators had been operating at maximum output which resulted significant increasing in ion concentration day by day. *Table 2* shows the variation of the ion levels in the examination room with respect of different ionization statuses.

*Table 2.* Variation of ion levels in the examination room

| **Ion polarity** | 25.5 $^0$C, 50% relative humidity | | 30.5 $^0$C, 50% relative humidity | |
|---|---|---|---|---|
| | **Average level [ions/cm$^3$]** | **Constant deviation [ions/cm$^3$]** | **Average level [ions/cm$^3$]** | **Constant deviation [ions/cm$^3$]** |
| | | **Basic points** | | |
| Positive | 277 | 79 | 393 | 46 |
| Negative | 118 | 45 | 194 | 30 |
| | | **Measured levels** | | |
| Positive | 12245 | 1350 | 14819 | 1586 |
| Negative | 4766 | 587 | 5494 | 897 |

It can be observed, that 10 °C rise in temperature causes higher level ion concentration in the room. Approximately, it is increased by 1650 ions/cm$^3$ in ionized status and by 190 ions/cm$^3$ in basic. This change was considered a marginal one during the examination. In the course of the examination test persons were allowed to read, play games, and listen to the radio as well. It was

permitted to discuss only their well-being. Each test person had to fill a summary questionnaire about well-being during the three-hour-long time of observation, which contained scales of overall thermal comfort, sensible perspiration, pleasantness, tiredness, humidity sensation, air movement, and personal feelings or moods. Sensitivity of estimates is confirmed by the fact that human factors bring individual results. Moreover, subjective sense of human comfort could be influenced by the points of begin and end of the measuring period, the part of the day, and the actual season. If change caused by these "distortive" parameters occurs at the same time as an ionization process, evaluation will be more complicated. It can be said without presenting the enormous amount of results, that neither of test persons prefers the status of negative over-ionization (see *Table 2*) in such a determined way as the basic level of negative ion concentration in the room.

Furthermore, it can be established that if effect of ionization even exists, it must be far too slight to be significant. However, it comes up as a question, how occupants in the room are influenced by this comparatively insignificance (*Jennings* and *Givoni,* 1964).

### *5. Summary of the measurement results*

Researchers could get any definite results in the course of evaluation trough the method of significance analysis. During estimation of pleasantness, some evidence was found in the evening teams for the rejection of the hypotheses.

By taking all the groups into consideration, during the assessments at temperature of 30.5 °C, a probability of P=0.03 was determined. There is a question of how ionization affects the groups at a different level during daytime and at night. Mood votes could not provide adequate information to prove the existence of the ionization effect. This lack of information was obtained also in regard to tiredness votes.

Authors are aware of the fact that the statistical methods which used by them is not the only way to evaluate such an assessment. Nevertheless, effect of ionization probably could not be proved by other methods in a more accurate way either. Influence on different people is not so significant at the measured level of temperature and ion concentration that it should be remarkable from technical point of view.

By summarizing the results it can be declared, that ionization has no significant effect on occupant's well-being and health in residential spaces. All the studies declared that there was some detectable effect, but it was not evaluated exactly. However, air conditioning developers keep on being engaged in this issue, and in the course of technological innovation, more researches were made in the field of ionization in regard to different technologies and building structures.

## *6. Practical usage of ion air conditioning*

It was observed, that filters in air handling devices deionize the air almost completely, but cheaper window air conditioners generate a surplus of positive charge. Reinforced concrete building structures cause further problems, whereas due to the shadow effect of the iron structure, small air ions can not even enter the building or they become neutralized shortly after the entering. This is also caused by that floating condensation seed particles can be separated really gently from the indoor air. Deionization could be generated in that case as well, when plastic parts of the building envelope get electrostatic charge. If the process of air conditioning is assumed optimal from the point of view of ionization, corresponding level of ion concentration should be ensured in an artificial way. It causes further difficulties, that air ionization in central air handling units can not be considered a practical method, whereas ions will be quickly neutralized in the ducts of the distribution system. It was proved by measurements that a three-meter-long metal air duct can completely deionized the air flowing inside. According to the experiences, efficient level of ionization can be achieved if the ioniser is placed into the air inlet. It was a signal result, that number of floating bacteria was decreased significantly by ionizators in the air of bandage, surgical, and operating rooms of hospitals. Surplus of positive ion concentration was measured in an average room with central heating in ten minutes after the room was properly aired. Based on the assessment it can be established, that it is sufficient to provide only the negative ion supplements.

In addition to the buildings, measurements were conducted in different vehicles, in driver cabins of buses and cars, and in cabins of dockyard cranes. Similar results were obtained in regard both to the train set of Budapest Metro and to Russian researches. Rate of unipolarity was not influenced significantly in the course of travelling underground and above ground. Surplus positive ion concentration was measured in the cabins of dockyard cranes even if the window was open. In summertime improved, ion concentration was detected only if a moderate breeze was blowing.

## *References*

*Dessauer, F.*, 1931: Zehn Jahre Forschung auf dem Physikalisch Medizinischen Grengebiet. G. Thieme Leipzi. (In Deutsch)

*Jennings, B.H.* and *Givoni, B.*, 1964: Enviroment Reactions in the 80F to 105F Zone. *ASHRAE Trans. V. 65,* 115–136.

*Kajtár, L.* and *Hrustinszky, T.*, 2001: Measurements of Indoor Air Quality and Emission of Indoor Materials. International Conference on Health, Comfort and Productivity vs. Cost Effective Operation of HVACR proceedings, Sttrbské Pleso, Slovakia.

*Kajtár, L.* and *Hrustinszky, T.*, 2002: Measurements of Indoor Air Quality and Emission of Indoor Materials. Proceedings of the third conference on mechanical engineering1. Budapest, Hungary, 362–366.

*Kajtár, L.* and *Hrustinszky, T.* 2003: Investigation of indoor air quality and emission of indoor used materials in Hungary. 7th International Conference Healthy Buildings, 2003. Singapore, Proceedings 3. 752–757.

*Kalmár, F.* and *Kalmár, T.*, 2013*:* Alternative personalized ventilation. *Energ. Bulidings 65*, 37–44.

*Kérdő I., Hay Gy.*, and *Sváb F.*, 1972: Problems of Ion Climatisation. Budapest.

*Yaglou, C.P., Benjamin, L.C.* and *Brandt. A.D.*, 1933: Physiologic Changes During Exposure to Ionized Air. *ASHRAE Transactions*. 357–372.

*Yaglou, C.P.*, 1935: Observations of Phyisical Efficiency in Ionized Air. *J. Ind. Hygiene 17*,280–282.

# IDŐJÁRÁS

*Quarterly Journal of the Hungarian Meteorological Service*
*Vol. 119, No. 3, July – September, 2015, pp. 409–423*


# A multivariate linear regression model of mean maximum urban heat island: a case study of Beregszász (Berehove), Ukraine


**Elemér László** and **Sándor Szegedi**

*Department of Meteorology, University of Debrecen*
*Egyetem tér 1, H-4043 Debrecen, Hungary*

*Corresponding author E-mail:* laszlo.elemer@science.unideb.hu



*(Manuscript received in final form December 12, 2014)*



**Abstract**—The aim of the research presented in this study is to elaborate a multivariate linear regression model that describes the spatial structure of the mean maximal development urban heat island (UHI) formed under favorable synoptic conditions on the basis of surface parameters. Temperature data were gathered in a small town, Beregszász, Zakarpattia, Ukraine. As a first step, a one-year-long UHI measurement campaign has been carried out using mobile techniques in order to obtain data for the description of the UHI in the study area. Two surface parameters (ratio of non-evaporating surfaces in the environment of the measurement sites and distance of measurement sites from the center of the settlement) have been selected first. The two surface parameters had to be quantified next. On this basis, relationships between surface parameters as independent variables and UHI intensities as dependent variables could be traced by performing a multivariate linear regression. Results have showed that the two chosen parameters have strong impact on UHI development in our study area. Spatial structure and intensity of UHI can be estimated with an accuracy of 0.4 °C within the built-up area of the town using our MLR model. The high resolution surface parameter database and the UHI estimating model enable the prediction of heat load of smaller spaces and town parts. This procedure helps the reduction of heat load and the determination of the location of green areas important for urban planning as well.



*Key-words:* multivariate linear regression model, non-evaporating surfaces, urban heat island

## *1. Introduction*

Settlements differ from natural environment significantly, due to altered surface geometry, different composition, and structure of urban atmosphere. Anthropogenic heat emissions should be taken into consideration as well (*Oke,* 1997). As a result, a local or meso gamma scale phenomenon, the urban climate develops (*Arnfiled,* 2003; *Oke,* 1973; *Orlanski,* 1975). Built-up areas are characterized by higher air and surface temperatures than close-to-natural areas in their neighborhood what is called urban heat island (UHI). The thermal difference between the town center and its rural environment determines the intensity of the urban heat island. UHI intensities have a special diurnal and annual course with maxima 3–5 hours after sunset and in late summer – early autumn (*Landsberg,* 1981). Additionally, UHI intensities change according to synoptic conditions as well: clear skies with calm weather are advantageous for the development of a strong UHI. This way, synoptic conditions determine the UHI intensities at a given point of time, while maximal (or potential) intensities can develop under favorable synoptic conditions. These factors are dynamic conditions of UHI development. Spatial pattern of the absolute or the mean maximal UHI is determined by static factors, the characteristics of the urban surface (*Bottyán* and *Unger*, 2003; *Bottyán et al.,* 2005*; Chen et al.,* 2011; *Ginnaros et al.,* 2013). Therefore, for studying the effects of static conditions on the spatial structure of UHI, favorable synoptic conditions are suitable. Investigations on heat islands give important information for town-planning (*Kuttler,* 1998), because the phenomenon influences the comfort sense of town dwellers (negatively in summer, positively in winter) essentially, alters the composition of urban vegetation, and can cause phenologic phase shifting (*Oke,* 1975).

Beyond determination of the characteristics of urban heat islands, recent studies focus on examination of their evolving factors in big cities. Our study area, Beregszász (Berehove) with its population of 26,000 belongs to the group of settlements which gain much less attention from this aspect. However, a high ratio of the population of Central and Eastern Europe live in small settlements, where heat islands can develop (*Fig. 1*), but there are much less studies in that field. Additionally, many rapidly growing independent suburbs of cities fall into that size category as well.

The main aim of the study presented here is to analyze the relationships between spatial structure of UHI and its formative surface parameters. There are many surface parameters that have an effect on UHI development. The hypothesis was that the most important parameters are the distance of a given site in the settlement from the geometrical center and the ratio of non-evaporating surfaces in that site.

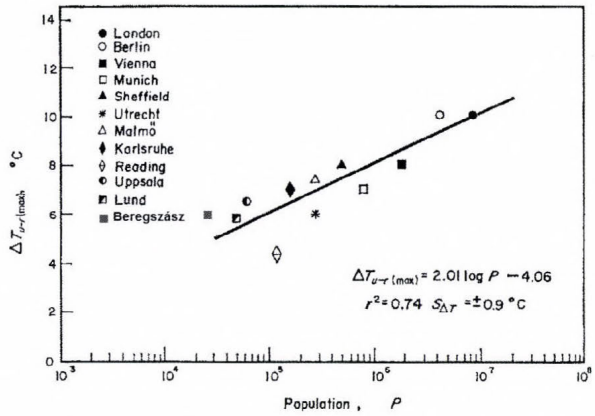


*Fig. 1.* Relationship between maximum observed heat island intensity ($T_{u\text{-}r(max)}$) and population *(P)* for European settlements indicating the position of Beregszász from this aspect (modified after *Oke,* 1973).

Other aim of our studies is to build an empirical estimating model for the spatial pattern of the mean maximal development UHI using the before mentioned surface parameters. The model could make possible the description of the spatial structure of the mean maximal development UHI for settlements of that size and structure category. Results can provide basic information on spatial pattern of the thermal excess in a given small settlement for spatial planning, forming urban spaces and green areas to utilize the advantages and prevent the drawbacks of the heat island phenomenon.

The examination of effects of surface parameters on UHI development requires high resolution spatial temperature data gathered under synoptic conditions what makes possible the strong development of UHI. For this reason, measurements were carried out under anticyclone synoptic conditions with clear skies and calm weather.

While examination of satellite images (*Bartholy et al.,* 2009) are more capable for heat islands of big cities (*Oke,* 1975; *Park,* 1986; *Kislov* and *Konstantinov,* 2011; *Lee* and *Baik,* 2010) (e.g., New York, Montréal, Moscow, Soul, Budapest), in the case of Beregszász, due to its size, the adaptation of a mobile measurement method (*Elansky et al.,* 2012) used by researchers of the University of Szeged (*Unger et al.,* 2000) and Debrecen (*Szegedi,* 2000) seemed to be adequate. The difference between the two methods is that satellite images make possible the determination of heat surplus in surface temperatures, while the latter one allows the measurement of heat excess in air temperatures.

Our mobile temperature measurements have provided abundant data for the characterization of UHI in Beregszász (Berehove). On this base, a multivariate linear regression model can be applied to analyze the role of some surface parameters in development of UHI in our study area.

## 2. Study area and methods

### 2.1. Location and climate of Beregszász (Berehove)

Beregszász (Berehove) (48.1°N, 22.3°E) lies 117 m above sea level. The southwestern part of the town can be found on a flat, alluvial plain, only occasionally interrupted by small hills. The town is situated on an almost flat terrain without great water bodies, what is advantageous from the aspect of the examination of the spatial development of urban heat island. It is located in the Zakarpattia Oblast (province) in Western Ukraine, near to the Hungarian border. It is the administrative center of the Berehivskyi Raion (district) with a population of 26,000.

The climate normal was calculated based on the Climate of the Carpathian Region Project dataset *(Lakatos et al., 2013)*. The town and its environment belong to Köppen's climate region Cfb on the basis of the climate parameters (*Table 1.*). The annual course of precipitation reaches its maximum in June and July. Prevailing wind direction is north-easterly.

*Table 1.* Annual and monthly means and sums of meteorological parameters at the weather station of Beregszász (Berehove), 1961–2010 (*Anon,* 1992; *Lakatos et al.,* 2013).

| **Beregszász (Berehove)** | |
|---|---|
| Annual mean temperature (˚C) | 9.8 |
| Temperature range (˚C) | 21.8 |
| Mean temperature in January (°C) | –2.7 |
| Mean temperature in July (˚C) | 20.2 |
| Annual mean precipitation (mm) | 682 |
| Annual mean wind speed (m $s^{-1}$) | 2.1 |
| Sunshine duration per year (h) | 1998 |

### 2.2. UHI measurements

Since the spatial pattern of the heat island is influenced by different urban morphological types significantly (*Szegedi,* 2006; *Unger et al.*, 2004; *Molnár et al., 2006*), we had to integrate the highly complex urban morphology into our model. Along a measurement route 42 measurement sites were selected, which are representative on one hand and quite smoothly cover the settlement on the other hand (*Fig. 2*). Temperature data was gathered 36 times along the route using mobile measurement techniques from January to December in 2005 by

Marguca V. and Kakas M. A measurement session was carried out using mobile measurement techniques in 2010 as well (n=10), under meteorological conditions advantageous for UHI development. This dataset was used as independent data in validating the established empirical model.

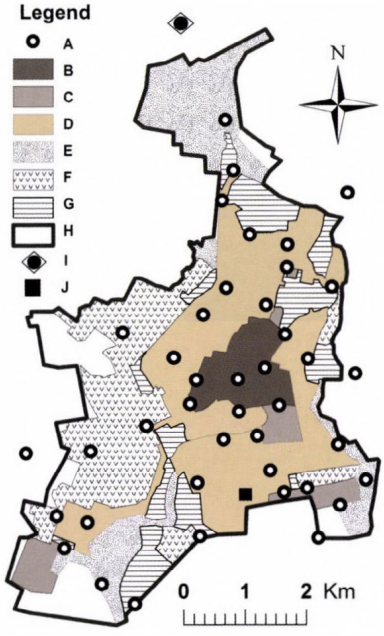


*Fig. 2.* UHI measurement sites (**A**) and urban morphological types in Beregszász (Berehove):**B**–historical town center with 3–5 storied buildings, **C**– 5–8 storied apartment houses, **D**—1-2 storied detached houses, **E**—open low-rise built-up area, **F**—industrial area, **G**—green areas inside the town, **H**—border of the study area, **I**—rural measurement site (reference point), **J**—weather station.

Measurement days were chosen according to the weather conditions within the decades: nights with rain and/or strong winds were excluded, since these conditions prevent the development of UHI. Measurements started approximately 3 hours after sunset, when heat island development is the most dynamic. Temperatures were recorded manually at each measurement site (*Table 2*).

*Table 2.* Observed meteorological parameters during the UHI measurements at the weather station of Beregszász (WMO station code is 33634; 48.19°N, 22.64°E, 122 m above sea level)

| Measurement date | Air temperature (°C) | | Cloudiness (octas) | Wind speed ($m\ s^{-1}$) | | UHI max | UHI mean |
|---|---|---|---|---|---|---|---|
| 2005 | 19 : 00 | 01 : 00 | 19 : 00 | 19 : 00 | 01 : 00 | | |
| January 5 | 2.8 | 3.5 | 7 | 0 | 0 | 0.9 | 0.5 |
| January 17 | –2.1 | –3.1 | 0 | 0 | 1 | 5.0 | 1.6 |
| January 25 | –1.3 | –1.4 | 4 | 1 | 2 | 2.2 | 1.2 |
| February 4 | –5.1 | –5.4 | 2 | 2 | 3 | 4.1 | 3.0 |
| February 16 | 0.3 | 0.8 | 0 | 0 | 1 | 1.8 | 1.1 |
| February 21 | 2.6 | 1.1 | 1 | 1 | 0 | 4.0 | 1.7 |
| March 3 | –1.4 | –0.8 | 2 | 2 | 1 | 0.9 | 0.4 |
| March 15 | 3.5 | 1.6 | 6 | 1 | 0 | 2.2 | 1.0 |
| March 22 | 0.1 | 1.4 | 0 | 2 | 1 | 2.6 | 1.5 |
| April 5 | 9.3 | 8.1 | 0 | 0 | 1 | 4.9 | 2.7 |
| April 18 | 11.3 | 10.4 | 8 | 3 | 4 | 0.5 | 0.3 |
| April 27 | 10.4 | 12.6 | 0 | 0 | 1 | 2.8 | 1.6 |
| May 5 | 13.7 | 12.8 | 4 | 1 | 2 | 0.9 | 0.7 |
| May 12 | 8.0 | 5.3 | 0 | 0 | 1 | 1.7 | 0.9 |
| May 23 | 19.4 | 17.8 | 0 | 0 | 0 | 3.9 | 2.1 |
| June 07 | 12.8 | 12.2 | 0 | 1 | 0 | 1.9 | 1.3 |
| June 14 | 17.1 | 15.5 | 0 | 0 | 0 | 4.6 | 1.4 |
| June 22 | 20.1 | 19.0 | 7 | 2 | 3 | 2.0 | 1.1 |
| July 8 | 18.2 | 16.9 | 0 | 1 | 0 | 4.9 | 2.4 |
| July 18 | 23.4 | 22.3 | 0 | 1 | 0 | 2.1 | 1.6 |
| July 21 | 15.5 | 14.1 | 0 | 1 | 1 | 4.9 | 1.4 |
| August 2 | 23.2 | 22.7 | 0 | 0 | 1 | 3.3 | 1.9 |
| August 12 | 18.1 | 17.7 | 0 | 0 | 0 | 2.3 | 1.4 |
| August 22 | 20.2 | 19.6 | 6 | 2 | 3 | 0.8 | 0.4 |
| September 6 | 12.7 | 12.0 | 0 | 0 | 1 | 4.5 | 2.6 |
| September 13 | 18.5 | 16.6 | 0 | 1 | 0 | 1.7 | 0.9 |
| September 22 | 14.2 | 15.9 | 0 | 0 | 2 | 6.6 | 4.1 |
| October 04 | 14.9 | 16.7 | 1 | 0 | 1 | 3.6 | 1.6 |
| October 11 | 9.0 | 8.1 | 0 | 0 | 0 | 3.9 | 1.7 |
| October 25 | 14.4 | 13.9 | 7 | 2 | 3 | 1.7 | 0.3 |
| November 03 | 3.3 | 1.5 | 0 | 1 | 0 | 4.2 | 2.5 |
| November 15 | 7.7 | 7.4 | 8 | 3 | 4 | 1.4 | 0.6 |
| November 22 | –2.2 | –3.0 | 0 | 0 | 1 | 2.7 | 1.8 |
| December 07 | 5.1 | 4.3 | 5 | 1 | 3 | 0.7 | 0.4 |
| December 13 | 0.6 | 0.5 | 6 | 0 | 1 | 1.0 | 0.6 |
| December 21 | –5.0 | –5.9 | 1 | 2 | 1 | 3.2 | 2.5 |

From the numerous methods developed for urban climate examinations, mobile techniques were used in order to get abundant comparable data for Debrecen and settlements involved in the research. Sensors of a digital thermometer were mounted on a car (with a resolution of 0.1 °C) at a height of 1.5 m, which is a common practice in UHI measurements. An important problem is that measurements should be carried out at exactly the same time in each grid. This is impossible using mobile techniques. The difference between the first and the last grid is 90 minutes, which is a considerable time span from the aspect of the change of temperatures in the different parts of the city. In order to get comparable temperature data during the measurements, we visited each grid two times: first on the way to the end of the route (the reference site, measurement site 42) and the second time on the way back. In this way we gained two temperature values for each grid. Since on the way back we visited the grids in reversed order, calculating the averages for the grids we gained values for the same time (the reference time). The reference time was four hours after sunset, since according to the literature, heat island intensity reaches its maximum 3–5 hours after sunset. Since the aim of the research was to trace the spatial pattern of urban heat island, only favorable conditions for heat island development were taken into consideration during the first campaign: measurements were carried out in anticyclone conditions. *Fig. 2* shows locations of measurement sites. UHI intensities ($\Delta t$ values) were calculated using the following formula:

$$\Delta t = t_{urban} - t_{rural} \,, \tag{1}$$

where $t_{urban}$ means temperature values measured at urban sites and $t_{rural}$ means temperatures measured at the reference site outside the town.

### *2.3. Determination of surface parameters*

The role of two surface parameters (presumably the most important ones) influencing the heat island development have been examined in the present study.

These are:

— Ratio of non-evaporating surfaces *(NES)* in the environment of measurement sites;

— Distance between measurement sites and the geometrical center (48.20°N, 22.64°E) of the town. Distances between measurement sites and the geometrical center of the town (km) were calculated, and distances were determined for the grid points of the network of the town as well.

Since non-evaporating surfaces store more heat during daytime than the close-to-natural evaporating surfaces, the air above built-up areas is warmer than over their surroundings. For this reason, quantification of the ratio of non-evaporating surfaces is necessary.

Close-to-natural evaporating areas are surfaces covered by vegetation (wood, shrub, lawn etc.) or bare soil. Non-evaporating surfaces are mainly artificial objects (buildings, pavements, other constructions). We have found that satellite images are the most suitable for parameter estimation. Thus, the ratio of non-evaporating surfaces was assessed visually using high-resolution, true color images of Google Earth. A grid network of 15.4×15.4 m was set on the images with the measurement points at the centers of the grids, and characteristic surface types for each grid were determined. The land cover was determined at 109,500 points with a spatial resolution of 15.4×15.4 m, which gives more detailed data than a grid network with 500×500 m resolution used by other researchers *(Kislov et al.,* 2011; *Unger et al.*, 2000).

It was an important question to decide what size of environment of measurement points influences the heat island intensity most strongly. We have tested four variations by statistical analysis:

—$NES_1$ – 9 grid points represent an area of 2134 $m^2$ around the measurement point;

—$NES_2$ – 25 grid points cover an area of 5930 $m^2$;

—$NES_3$ – 49 grid points represent an area of 11,621 $m^2$ around the measurement point;

—$NES_4$ –81 grid points cover an area of 19,210 $m^2$.

As a first step, the size of the environment, which influences the heat island intensity most strongly around the measurement sites was determined statistically. For this reason, *NES* values of the 4 chosen areas were correlated with the mean maximal heat island intensities of measurement sites, and significant correlation was found in every case (*Table 3*).

*Table 3.* Connection between the ratio of non-evaporating surfaces (*NES*) and UHI intensities, *r*– correlation coefficient

| Period | $NES_1$ *r* | $NES_2$ *r* | $NES_3$ *r* | $NES_4$ *r* | Sign. level |
|---|---|---|---|---|---|
| $\Delta t$-annual | 0.57 | 0.64 | **0.70** | 0.67 | 1% |
| $\Delta t$/heating | 0.56 | 0.64 | **0.69** | 0.67 | 1% |
| $\Delta t$/non-heating | 0.54 | 0.59 | **0.68** | 0.61 | 1% |

The strongest relationship was found between $NES_3$ and the UHI, so the 11,621 $m^2$ area influences heat island intensities of Beregszász most remarkably. Maps were completed on the basis of the ratio of non-evaporating surfaces in Surfer 8.0 (*Fig. 3*). This statistical software offers several types of interpolation methods, from which we have chosen the widely used Kriging-procedure. Ratio of non-evaporating surfaces reaches its maximum in the center of the town, however, there are some patches with high ratio of artificial (non-evaporating) surface cover around the center near the edges of the settlement. They are industrial areas and housing estates. The distance of the measurement points from the town center was determined by using the differences of coordinates of the previously mentioned grids.

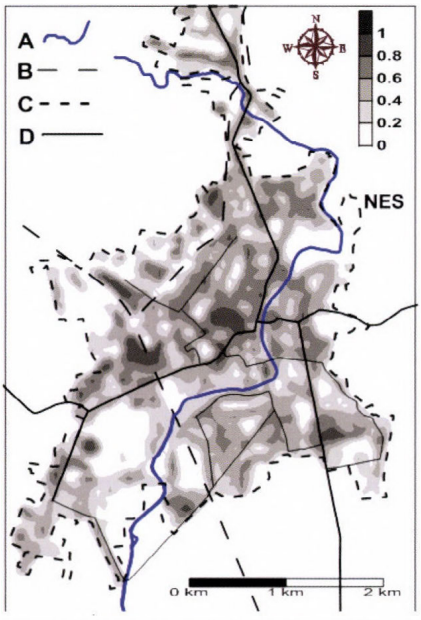


*Fig. 3.* Spatial pattern of the of non-evaporating surfaces in Beregszász: A– Vérke canal, B–railroad line, C– border of built-up area, D– main road line.

Correlations between variations of *NES* ($NES_1$-$NES_4$) and distances from the geometrical center of the town were determined. In this way, possible linear dependence between explanatory variables was traced. In the case of dependence between explanatory variables, one of them was ignored in order to create an independent system of explanatory variables. This method

minimized the possible multicollinearity ($M$) of explanatory variables incorporated into the model. Value of $M$ shows the magnitude of the non-separable effect of factor variables. In this way, the coefficient of multiple determination can be divided into the partial effect of each factor variable and the joint effect of the factor variables. In our case, the value of $M$ was 0.37 which cannot be regarded as significant. This value was tested using the variance inflation factor (VIF):

$$VIF_i = \frac{1}{1 - R_i^2} \,. \tag{2}$$

This factor shows how many times greater the actual variance of the estimated coefficient of variable $i$ is than it would be with the complete exclusion of multicollinearity. Value of $VIF$ in our case is 1.58 suggesting slight multicollinearity that determines the estimation strength of the model not significantly.

### *2.4. The statistical model applied*

Beside basic statistical analysis (average, correlation), we have attempted to build an empirical model to investigate relationships between heat island intensities and surface parameters. We have applied the multivariate linear regression (MLR) method in the model, which is deemed to be advisable for solving similar kind of problems by other researcher's (*Bottyán et al.*, 2005; *Hjort et al.*,2011; *Szymanowski* and *Kryza,* 2012).The MLR equation is

$$Y = a + b_1 X_1 + b_2 X_2 + ... + b_i X_i \,, \; i=1,2,\ldots,n \tag{3}$$

where $Y$ is the dependent variable, $a$ is a constant, $X_i$ is independent variable, $b_i$ is the partial regression coefficient of independent variable number, and $n$ is the number of independent variables taken into consideration (*Ezekiel* and *Fox,* 1959).

Fitting of the multiple regression equation was performed using the method of least squares. Calculations were carried out using SPSS software pack. Establishment of the linear model was made suing the software SPSS applying the Enter method. Kolmogorov–Smirnov tests proved that distribution of dependent and independent variables involved in the model is not different significantly from normal distribution what is a condition of correlation and regression calculations.

## *3. Results and discussion*

### *3.1. Characteristics of the mean maximal UHI*

Mean maximal diurnal UHI intensities culminated in the center of the settlement of Beregszász with 2.3 °C during the studied period, while maximal observed UHI intensity reached 6.1°C, in accordance with the results of *Oke* (1973). Development of the UHI is supported by high ratio of non-evaporating surfaces, compact built-up structure with two storied buildings, and high traffic density beside the central part of studied area.

A map of mean maximal UHI intensities have been prepared by calculating the average maximal UHI intensities for each measurement sites (*Fig. 2*). The following main characteristics of the UHI can be determined (*Molnár et al.*, 2006; *Molnár, 2007*):

- Highest mean maximal UHI intensities over 2.3 °C form the "peak" in the center of the town.
- Thermal excess decreases gradually from the center towards the outskirts of the town. The phenomenon "plateau" cannot be identified due to the small size of the settlement, presumably.
- Thermal excess over 1 °C on the slopes of the low mountain ridge bordering the town from the East is linked to the UHI.
- Low intensity fringes (around 1 °C) of the UHI of Beregszász reach the small, previously independent villages around the town (Beregardó on the north and Búcsú on the southwest) and a housing estate on the southeastern border of the town.
- Mean maximal UHI intensities around the weather station of Beregszász reach 1.2 °C what should be taken into consideration in the processing of datasets measured there.
- Low intensity borders of the mean maximal UHI reaches far over the borders of the built-up area of the town due to the impacts of airflows.

### *3.2. Structure of the multivariate model*

Our main aim was to elaborate a universal model for estimation of spatial pattern of mean maximal heat islands on the base of meteorological and morphological data of Beregszász.

The input parameters of the multivariable model are

- heat island intensity as a dependent variable (°C),
- ratio of non-evaporating surfaces as an independent variable (*NES* – given in %), and
- distance of measurement sites from the geometrical center of the town as an independent variable (D – given in meters).

The following model equation has been created for the spatial structure of annual mean maximal heat island intensity using multivariate regression process of SPSS software:

$$\Delta t_{annual} = 1.642 - 0.00026 \times D + 0.54 \times NES \,. \tag{4}$$

It has been proved that the two parameters play an important role in development of the temperature excess ($r^2$=0,766). The value of $D$ partial correlation coefficient is prominent in the model ($r^2$=0,766), since it is much higher than the other parameter ($NES$ – $r$=0.477), which means that it may play much more important role in the formation of UHI. Spatial structure of UHI in Beregszász has been described on the base of UHI intensities calculated by the model. It can clearly be seen in the map that ratio of non-evaporating surfaces determines the alteration of air temperature much obviously in the built-up area than on the outskirts (*Fig. 4*). Where *NES* values are above 40%, isotherm lines run parallel with them, otherwise isotherm lines diverge. The reason for this is the irregular shape of the borderline between the built-up and close-to-natural areas in the town, probably.

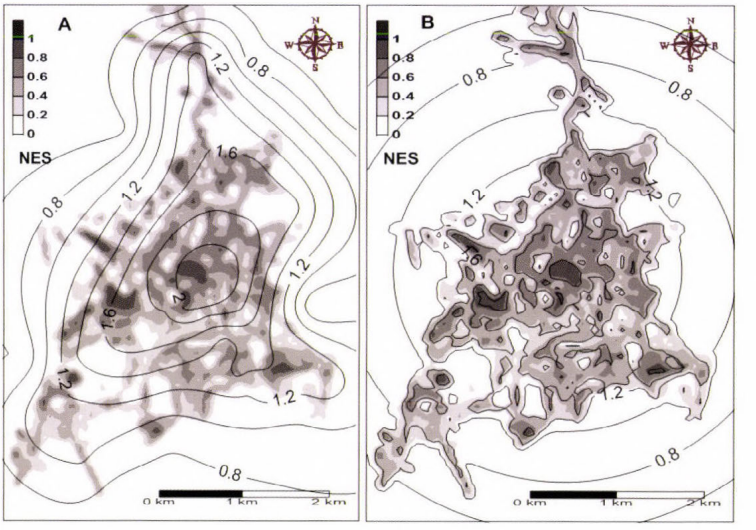


*Fig. 4.* Spatial structure of non-evaporating surfaces, measured (A) and estimated (B) mean maximal UHI intensities (difference between isotherms is 0.2 °C) for the studied period.

Empirical estimation model equations were created for the summer period (April 16 – October 15), winter period (October 16 – April 15), and sunny (under 4 octas) and cloudy days (over 4 octas).

Differences can be found in the empirical model of heat island intensities in the heating and non-heating periods. Values of $r^2$ indicate that the two built-up factors determinate the „strength" of heat excess developed in the town relatively weakly in the winter period. *Table 4.* presents the multivariate linear regression equations created for heating and non-heating periods. The disparity of partial correlation coefficients emphasizes the higher importance of distance from the center probably in the cold season, since decreasing evaporation rates weaken the impact of evaporating surfaces on the energy balance in the heating season.

*Table 4.* The multivariate regression equations of heat island intensities at measurement sites, the surface parameters influencing them, and the partial correlation coefficients built in the equations for Beregszász. $r^2$ is the coefficient of multiple determination, the other applied notations are the same as in *Table 3.*

| | **Equation of multivariate linear regression** | *r2* | **Partial correlation coefficients** | |
|---|---|---|---|---|
| | | | ***D*** | ***NES*** |
| $\Delta t$/heating | $=1.652-0.000274\times D+0.709\times NES$ | 0.650 | –0.665 | 0.513 |
| $\Delta t$/non-heating | $=1.679-0.000273\times D+0.319\times NES$ | 0.732 | –0.737 | 0.309 |

Correlation analysis was carried out to verify our model. Mean maximal UHI intensity values estimated by the model were correlated to mean maximal UHI intensities calculated on the base of results of a campaign of ten measurements carried out in 2010. There is a significant connection between the two datasets ($r=0.86$, $n=41$) at a level of significance of 0.1. Maximal error of the model was 0.4 °C, standard deviation of error was under 0.2 °C.

## *4. Conclusions*

Our attempt to elaborate a model describing the spatial pattern of UHI in a small town has proved to be successful from methodological aspects. The multivariate linear regression model created by the integration of two surface factors as ratio of non-evaporating surfaces and distance of measurement points from the

settlement center describes the structure of UHI in our study area well. A part of spatial pattern of thermal excess developed in the built-up area could not be interpreted by the regression model, what can be a result of measurement bias on one hand and factors not taken into consideration in the model on the other hand. A continuation of this research for this reason could be to integrate new surface parameters into the model like sky view factor (SVF) and aspect ratio (H/W), which can have a significant impact on UHI formation as well.

According to literature and our previous examinations, the limit of the development of urban heat island is under 1,000 inhabitants. Our results provide better knowledge on spatial structure of UHI in small settlements. It is important, since small settlements have different structures from cities making it impossible to study the spatial and temporal characteristics of those heat islands on the basis of simple extrapolation of results for big cities.

Most advantageous location of new buildings and green areas can be found using UHI maps. Human comfort conditions of public spaces could be improved by the establishment of smaller parks in central areas of the town, while heating energy demand could be decreased by more compact built-up in residential areas. This way our results could be applied in spatial planning.

***Acknowledgements***:The authors are grateful to anonymous reviewer for providing valuable comments this study. The authors wish to special thanks to Molnár József, Kakas Mónika, and Marguca Viola. The publication is supported by the Arany János Közalapítvány a Tudományért.

## *References*

*Arnfield J.A.*, 2003: Two decades of urban climate research: A review of turbulence, exchanges of energy and water, and the urban heat island. *Int. J. Climatol, 23,* 1–26.

*Atkinson B.W.*, 2003: Numerical modelling of urban heat-island intensity. *Bound.-Lay. Meteorol. 109,* 285–310.

*Anon,* 1992: Climatological normals (CLINO) for the period 1961–1990. *WMO/OMM-No. 847.*

*Chen F., Kusaka H., Bornstein R., Ching J., Grimmond S., Grossman-Clarke S., Loridan T, Manning K., Martilli A., Miao S., Sailor D., Salamanca FP., Taha H., Tewari M., Wang X., Wyszogrodzki A., Zhang C.*, 2011: The integrated WRF/urban modelling system: development, evaluation, and applications to urban environmental problems. *Int. J. Climatol., 31*, 273–288.

*Bartholy J., Pongrácz R., Lelovics E.*, and *Dezső Zs.*, 2009: Comparison of urban heat island effect using ground-based and satellite measurements. *Acta Climatologica et Chronologica Universitatis Szegediensis. 42-43*, 7–15.

*Bottyán Z.* and *Unger J.*, 2003: A multiple linear statistical model for estimating mean maximum urban heat island. *Theor. Appl.Climatol. 75,* 233–243.

*Bottyán Z., Kircsi A., Szegedi S.*, and *Unger J.*, 2005: The relationship between built-up areas and the spatial development of the mean maximum urban heat island in Debrecen, Hungary, *Int. J. Climatol.25*, 405–418.

*Elansky, N.F., Lavrova, O.V., Moklov, I.I.*, and *Rakin A.A.*, 2012: Heat island structure over Russian towns based on mobile laboratory observation. *Doklady Earth Siciences 443*, Part 1, 420–425.

*Ezekiel, M.* and *Fox, K.A.*, 1959: Methods of correlation and regression analysis: Linear and curvilinear. John Wiley, Oxford, England.

*Giannaros, T.M., Melas, D., Daglis, I.A., Keramitsoglou, I.,* and *Kourtidis, K.,* 2013: Numerical study of the urban heat island over Athens (Greece) with the WRF model. *Atmos. Environ. 73*, 103–111.

*Hjort, J., Suomi, J.,* and *Käyhkö, J.,* 2011: Spatial prediction of urban-rural temperatures using statistical methods", *Theor. Appl. Climatol. 106*, 139–152.

*Kislov, A.V.* and *Konstantinov, P.I.,* 2011: Detailed spatial modeling of temperature in Moscow. *Meteorol. Gidrol., 5*. 300–306.

*Kuttler, W.,* 1998: Stadtklima. In Stadtökologie (eds: Sukopp, H. und Wittig, R.) Gustav Fischer, Stuttgart-Jena-Lübeck-Ulm,. 125–167.

*Molnár J., Kakas M.,* and *Marguca V.*, 2006: A beregszászi hősziget intenzitásának és térbeli szerkezetének vizsgálata (Examination of intensity and the spatial structure of maximum heat island in Beregszász (Berehove), Ukraine). In Kiss A, Mezősi G, Sümeghy Z (szerk): Táj, környezet és társadalom. Ünnepi tanulmányok Keveiné Bárány Ilona professzor asszony tiszteletére. SZTE Éghajlattani és Tájföldrajzi Tanszék, Természeti Földrajzi és Geoinformatikai Tanszék, Szeged, 509-518. (*in Hungarian*)

*Molnár J.,* 2007: A városi hősziget és annak kapcsolata a főbb felszínparaméterekkel Beregszász példáján. In Tóth Tamás, Bíróné Kircsi Andrea (szerk.) Kedvező széllel Kunhegyestől Debrecenig: Tiszteletkötet Dr. Tar Károly 60. születésnapjára. Debrecen: Magyar Szélenergia Társaság, 2007. pp. 225-233. (*in Hungarian*)

*Lakatos M., Szentimrey T., Bihari Z.,* and *Szalai S.,* 2013: Creation of a homogenized climate database for the Carpathian region by applying the MASH procedure and the preliminary analysis of the data. *Időjárás 117*, 143–158.

*Landsberg, H.E.,* 1981: The Urban Climate. Academic Press: New York.

*Lee, S.H., Baik, J.J.,* 2010: Statistical and dynamical characteristics of the urban heat island intensity in Seoul. *Theor. Appl. Climatol. 100*, 227–237

*Oke, T.R.,* 1973: City size and the urban heat island. *Atmos. Environ. 7*, 769–779

*Oke, T.R.,* and *Maxwell, G.B.,* 1975: Urban heat island dynamics in Montreal and Vancouver. *Atmos. Environ. 9*, 191–200.

*Oke, T.R.,* 1997: Urban climates and global environmental change. In (eds.: R.D Thompson. and Perry) Applied Climatology. Routledge, London and New York, 273–287.

*Orlanski, I.* 1975: A rational subdivision of scales for atmospheric processes"*Bull. Amer. Meteor. Soc., 56,* 527–530.

*Park, H.S.,* 1986: Features of the heat island in Seoul and its surrounding cities. *Atmos. Environ. 20,* 1859–1866.

*Szymanowski, M.* and *Kryza, M.,* 2012: Local regression models for spatial interpolation of urban heat island– an example from Wroclaw, SW Poland. *Theor. Appl. Climatol. 108,* 53-71.

*Szegedi S.,* 2000: Spatial structure of urban heat island in Debrecen. *In 3rd European Conference on Applied Climatology,* Pisa, Italy, 16–20 October; CD-ROM

*Szegedi S.,* 2006: Heat islands in small and medium sized towns in Hungary. *Proceedings of Sixth International Conference on Urban Climate,* Gothenburg, Sweden, 439–442.

*Unger J., Sümeghy Z., Gulyás, Á., Bottyán Z.,* and *Mucsi L.,* 2000: Land-use and meteorological aspects of the urban heat island. *Meteorol. Appl. 8,* 189–194.

*Unger J., Bottyán Z., Sümeghy, Z.,* and *Gulyás A.,* 2004: Connection between urban heat island and surface parameters: measurements and modeling. *Időjárás 108*, 173–194.

# INSTRUCTIONS TO AUTHORS OF *IDŐJÁRÁS*

The purpose of the journal is to publish papers in any field of meteorology and atmosphere related scientific areas. These may be

- research papers on new results of scientific investigations,
- critical review articles summarizing the current state of art of a certain topic,
- short contributions dealing with a particular question.

Some issues contain "News" and "Book review", therefore, such contributions are also welcome. The papers must be in American English and should be checked by a native speaker if necessary.

Authors are requested to send their manuscripts to

*Editor-in Chief of IDŐJÁRÁS*
*P.O. Box 38, H-1525 Budapest, Hungary*
*E-mail: journal.idojaras@met.hu*

including all illustrations. MS Word format is preferred in electronic submission. Papers will then be reviewed normally by two independent referees, who remain unidentified for the author(s). The Editor-in-Chief will inform the author(s) whether or not the paper is acceptable for publication, and what modifications, if any, are necessary.

Please, follow the order given below when typing manuscripts.

*Title page:* should consist of the title, the name(s) of the author(s), their affiliation(s) including full postal and e-mail address(es). In case of more than one author, the corresponding author must be identified.

*Abstract:* should contain the purpose, the applied data and methods as well as the basic conclusion(s) of the paper.

*Key-words:* must be included (from 5 to 10) to help to classify the topic.

*Text:* has to be typed in single spacing on an A4 size paper using 14 pt Times New Roman font if possible. Use of S.I. units are expected, and the use of negative exponent is preferred to fractional sign. Mathematical formulae are expected to be as simple as possible and numbered in parentheses at the right margin.

All publications cited in the text should be presented in the *list of references*, arranged in alphabetical order. For an article: name(s) of author(s) in Italics, year, title of article, name of journal, volume, number (the latter two in Italics) and pages. E.g., *Nathan, K.K.,* 1986: A note on the relationship between photosynthetically active radiation and cloud amount. *Időjárás 90,* 10-13. For a book: name(s) of author(s), year, title of the book (all in Italics except the year), publisher and place of publication. E.g., *Junge, C.E.,* 1963: *Air Chemistry and Radioactivity.* Academic Press, New York and London. Reference in the text should contain the name(s) of the author(s) in Italics and year of publication. E.g., in the case of one author: *Miller* (1989); in the case of two authors: *Gamov* and *Cleveland* (1973); and if there are more than two authors: *Smith et al.* (1990). If the name of the author cannot be fitted into the text: *(Miller,* 1989); etc. When referring papers published in the same year by the same author, letters a, b, c, etc. should follow the year of publication.

*Tables* should be marked by Arabic numbers and printed in separate sheets with their numbers and legends given below them. Avoid too lengthy or complicated tables, or tables duplicating results given in other form in the manuscript (e.g., graphs).

*Figures* should also be marked with Arabic numbers and printed in black and white or color (under special arrangement) in separate sheets with their numbers and captions given below them. JPG, TIF, GIF, BMP or PNG formats should be used for electronic artwork submission.

*More information* for authors is available: journal.idojaras@met.hu

Published by the Hungarian Meteorological Service

Budapest, Hungary

**INDEX 26 361**

**HU ISSN 0324-6329**